Document Number**:** H2020-ICT-52/RISE-6G/3.4

Project Name:
Reconfigurable **I**ntelligent **S**ustainable **E**nvironments for **6G** Wireless Networks
(RISE-6G)

Deliverable 3.4

Optimised RIS prototypes for PoCs and model assessment test

Date of delivery:	30/06/2023	Version:	1.0
Start date of Project:	01/01/2021	Duration:	36 months

Deliverable D3.4
Optimised RIS prototypes for PoCs and model assessment

Project Number:	H2020-ICT-52 / 101017011
Project Name:	**R**econfigurable **I**ntelligent **S**ustainable **E**nvironments for **6G** Wireless Networks

Document Number:	H2020-ICT-52/RISE-6G/D3.4
Document Title:	Optimised RIS prototypes for PoCs and model assessment test
Editor(s):	R. D'Errico (CEA)
Authors:	UNOT: G. Gradoni, S. Terranova, H. Taghvaee, M. Richter, G. Tanner CEA: T. Mazloum, M. Bouslama, F. Munoz, S. Garbieh, G. Makhoul, A. Mudonhi, A. Clemente, R. D'Eerrico GNW: A. Toubal, L. Santamaria, G. Lerosey and V. Killamsetty. CNRS: M. Di Renzo, H. El Hassani, S. Jeong CNIT : L. Bastianelli, F. Moglie, V. Mariani Primiani, E. Colella TIM: D. Micheli AAU : O. Franek NKUA : G. Alexandropoulos, I. Vinieratou, A. Papadopoulos ORA : P. Ratajczak, D.-T. Phan-Huy, Yohann Benedic NEC: P. Mursia, V. Sciancalepore, X. Costa-Pérez
Dissemination Level:	PU
Contractual Date of Delivery:	30/06/2023
Security:	Public
Status:	Final
Version:	1.0
File Name:	RISE-6G_WP3_D3.4_Final.docx

Abstract

This document reports the final results of RISE-6G WP3 activities on RIS design, prototyping and modelling . The prototypes here presented have been characterized in laboratory environments and employed in channel measurement campaigns. The final assessment of their performance in an overall Proof of Concept is left for the final WP7 deliverable

Keywords

RIS, Reconfiigurable Intelligent Surface, Model, Channel

Contents

List of Figures

List of Tables

1 Introduction

This documents illustrate the final results of WP3 on RIS prototyping and modelling. The main achievement are here reported as extension of previous deliverables (D3.1-D3.3). The results here presented are non-comprehensive of the whole WP activity. Different prototypes and early channel measurements, as well preliminary models have been presented in the above mentioned reports.

The report is organized as follows:

- Section 2 illustrates the different prototypes which include Riflective (R) and Transmitting (T) RIS. Different technologies are presented together with their characterization
- Section 3 shows the final models assessment based on the real RIS design developed in the project
- Section 4 presents different channel measurement campaign in including RIS. The objective here is to characterize and model the RIS effect in a multipath context.

Additionally some example of model exploitation for communications purposes and a discussion on model harmonization are also included.

2 RIS Hardware Prototyping and Characterization

In this section, the deliverable reports on the different prototypes designed and manufactured by the different partners of the project. It concerns mainly RIS operating in the sub-6GHz band, in the mmwave 5G FR2 band and in the V and D bands.

2.1 **RF switch-based sub-6GHz RIS**

In this section we overview the main hardware characteristics of the NEC RIS, which is designed to operate at 5.3 GHz, and its empirical characterization [RMG22].

We have designed a 10x10 array of patch antennas on PCB, which are designed to operate at 5.3 GHz, as shown in Figure 2-1(left-hand side). The overall structure of the board is depicted on the right-hand side of the same figure. The array is divided into 10x10 unit cells, which are connected to the MCU via a pair of buses, namely the *row* and *column* bus. Each unit cell i, j is selected when both corresponding buses are activated. With this design, we limit the number of MCU connections to the number of rows plus columns, as opposed to one connection per unit cell. A second set of bus is used to forward the chosen configuration of each unit cell, which is encoded with 3 bits and stored in as many Flip-flops per unit cell.

More specifically, each unit cell is comprised of a reflective patch antenna connected to an 8-port RF switch. Seven of these ports are connected to open-ended delay lines of different lengths, which are designed to induce 7 equally spaced phase shifts to the incoming signal. One of the RF switch ports is connected to a $50\ \Omega$ matched resistor, which is used to absorb the incoming signal and effectively *turn off* the associated unit cell. Accordingly, we label the RIS configuration in which each unit cell is connected to the absorber as *absorption mode.*

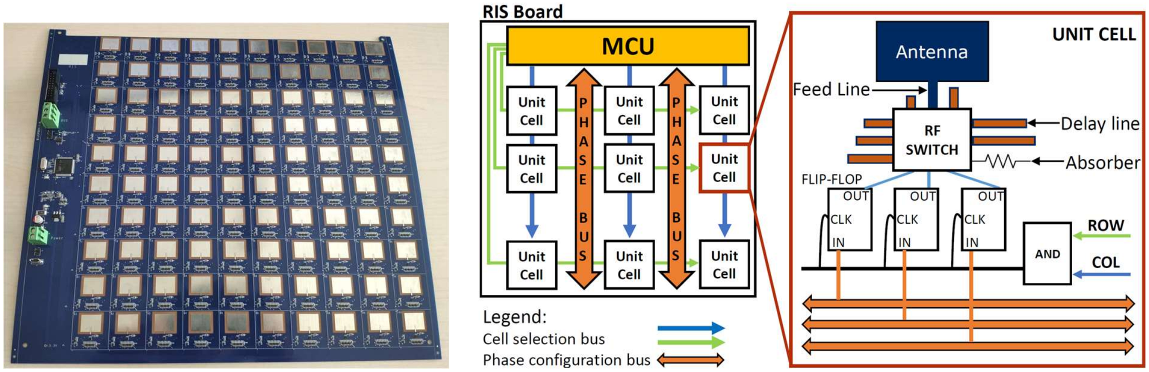

Figure 2-1: NEC 10x10 sub-6 GHz RIS final printout.

The overall structure has a relatively low power consumption, which has been measured to be 62 mW and is mainly due to the power required by the MCU and the Flip-Flops. Moreover, each unit cell is configured sequentially by the MCU, requiring a total of 0.35 ms.

The unit cell has a total dimension of 27.25×27.25 mm, whereas the patch antennas are 15.5×12.8 mm with an isotropic array response, as shown in Figure 2-2. Moreover, each unit cell is spaced by $\lambda/2$ with the neighboring cells. Moreover, this RIS board is designed in a modular way, meaning that multiple RIS boards can be connected, while preserving the same unit cell spacing across consecutive boards.

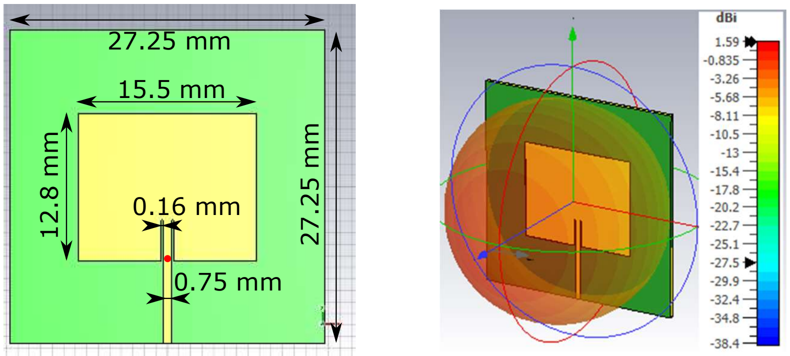

Figure 2-2: NEC sub-6GHz RIS unit cell.

This RIS prototype has been characterized in an anechoic chamber. Specifically, we have placed a TX, composed by a USRP connected to a master PC, and the RIS board together on a remotely controlled turntable with a distance of 1 m between each other. Whereas we have place d RX, consisting again of a USRP connected to a master PC, at 6 m, on the opposite side of the chamber, as depicted in Figure 2-3. Hence, when we rotate the table, the angle between the RIS and RX, denoted as θ_r is varied, while the angle between TX and RIS, i.e., θ_t, is kept fixed.

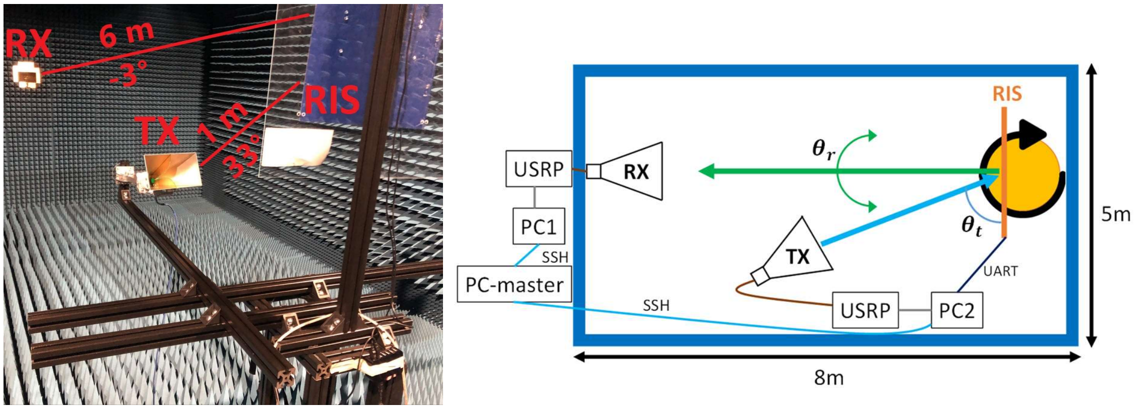

Figure 2-3: Anechoic chamber measurement setup.

The characterization consists in sweeping across a predefined codebook of RIS configurations while rotating the turntable. Hence, for every position of the TX-RIS block, we sweep across all available RIS configurations and collect relevant measurements at the RX-side. In particular, the TX is configured to stream a continuous reference OFDM QPSK signal with 5 MHz bandwidth and -30 dBm of transmit power per subcarrier. The RX then demodulates the signal and measures the RSRP. Both the TX and RX are equipped with horn antennas providing a gain of 13.5 dBi. The value of θ_t is set to 90° and 20° in two different sets of measurements.

The RIS codebook consists in a total of 1891 distinct configurations, where each configuration is calculated by aligning the main beam in a specific direction (θ_n, ϕ_n) in space, where θ_n and ϕ_n represent the azimuth and elevation directions. We vary both angles as $\theta_n \in [-\pi/2,\ \pi/2]$ and $\phi_n \in [-\pi/4,\ \pi/4]$ with a spacing of 3° in both cases.

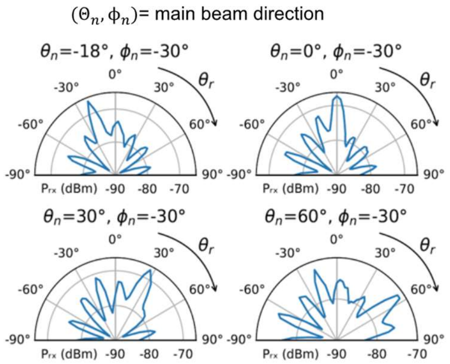

Figure 2-4: NEC sub-6GHz RIS measured beampattern.

The measured beampattern for the case of $\theta_t = 90^\circ$ is shown in Figure 2-4/ We measured a HPBW of 10°, RCS of 11.2 dBm^2 and a gain of 27 dB in the best-case scenario. Further experimental data can be found in [RMG22] and references therein (e.g., GitHub repository).

2.2 R-RIS Design using PIN Diodes via Rotation Technique

Several techniques are used to design R-RIS unit cells, for example, varying size patches, varying delay line lengths, and varying rotation angles. To the best of our knowledge, the technique based on varying rotation angles was previously used in the literature only in the case of designing passive circularly polarized RA. In our work, we use the aforementioned rotation strategy, to design a 1-bit reconfigurable RA unit cell linearly polarized, where the states of two p-i-n diodes will control the current distribution on top of the patch, and create a 180° phase difference. The proposed unit cell is used to synthesize a RA composed of 8×8 unit cells. The full antenna is optimized using an in-house developed MATLAB tool. Furthermore, Full-wave simulations are performed to validate the design and the optimization tool.

2.2.1 Geometry of the unit cell and operating principle

The schematic of the proposed linearly-polarized unit-cell is shown in Figure 2-5. It is composed of four metal layers printed on two Isola Astra MT77 substrates and bonded with Astra MT77 pre-preg bonding film (ϵ_r= 2.95, $tan\delta$ = 0.0019). The top layer (Figure 2-5 (b)) is the radiating element. It consists of center-fed O-slot rectangular patch antenna working in reflecting mode. The patch antenna is connected by a metalized via hole located at its center to the ground plane (Figure 2-5(e)). Two p-i-n diodes MA4AGP907 are flip-chipped on the patch antenna to tune the reflection phase, and these diodes are controlled by a bias line (Figure 2-5 (c)) printed on the opposite side of the substrate. The bias network includes microstrip radial stubs to isolate the RF signals. The patch is also connected to a delay line (Figure 2-5 (c)), printed as well on the opposite side of the substrate. The DC connection to ground is realized with a short circuit stub.

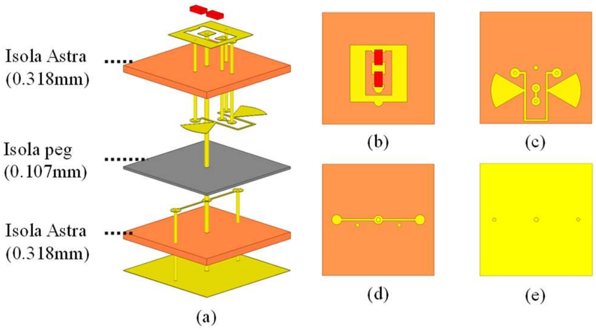

Figure 2-5 The proposed 1-bit linearly-polarized unit-cell: (a) Schematic view, (b) radiating element, (c) biasing layer, (d) DC connection to the ground layer, and (e) ground plane.

The two PIN diodes are biased in opposite states (one p-i-n diode is switched ON while the other one is in OFF state). Due to the presence of the delay line a 90° rotation of the current distributions is expected to occur. In the passive case, the rotation of the printed elements in the reflectarray cell by an angle α_{rot} results in a phase shift of $\Delta\phi = 2 \times \alpha_{rot}$ Therefore, if the alternation states of the diodes will incur a rotation of angle α_{rot} = 90°, then a $\Delta\phi$ = 180° phase shift is obtained, i.e., a 1-bit phase quantization.

2.2.2 Simulation of the unit cell

The two generated states of the unit cells will be denoted by State000 and State180. As explained in the previous section and depicted in Figure 2-6, the alternation of the diodes states will induce a variation in the current distribution and thus a phase shift of 180°. The OFF state of the diode (red diode) is equivalent to a capacitor C_{off} = 0.042 pF in parallel with a resistor R_{OFF} = 300 kΩ. Whereas the ON state of the diode (green diode), is equivalent to an inductor L_{ON} = 0.05 nH in series with a resistor R_{ON} = 4.2 Ω. This 1-bit unit cell has been simulated for its two-phase states using the commercial software Ansys HFSS with periodic boundary conditions on the unit-cell lateral faces and a Floquet port excitation in normal incidence (Figure 2-7). The unit cell presents a phase difference of almost 180°± 20° and a reflection coefficient magnitude higher than -1.5 dB over the frequency band for both unit cell states.

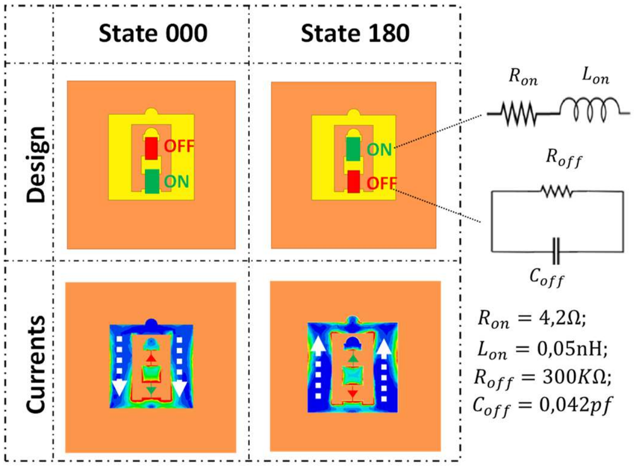

Figure 2-6 The two states of the unit cell with the corresponding diode states and current distributions.

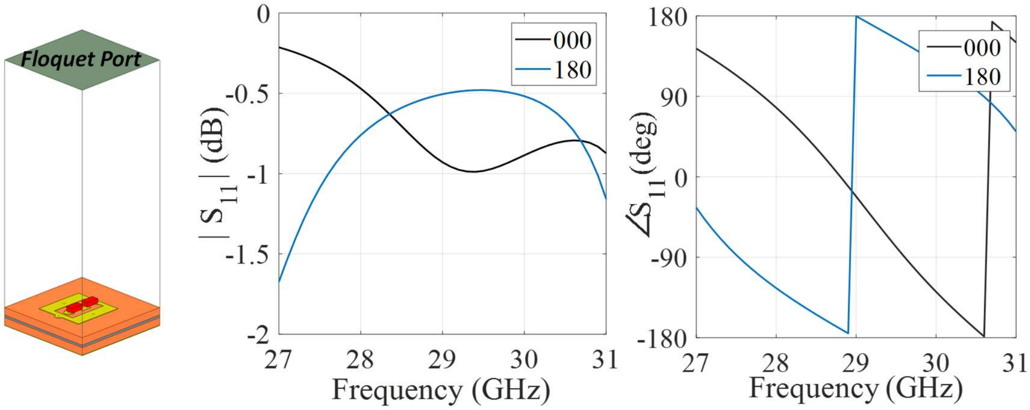

Figure 2-7 The unit cell simulation setup , the magnitude and the phase of the reflection coefficients of the two states (State000 and State180).

2.2.3 Prototype

The optimized protoype has been realized for a 20x20 UCs configuration, by including in the layout the biasing network of PiN diodes

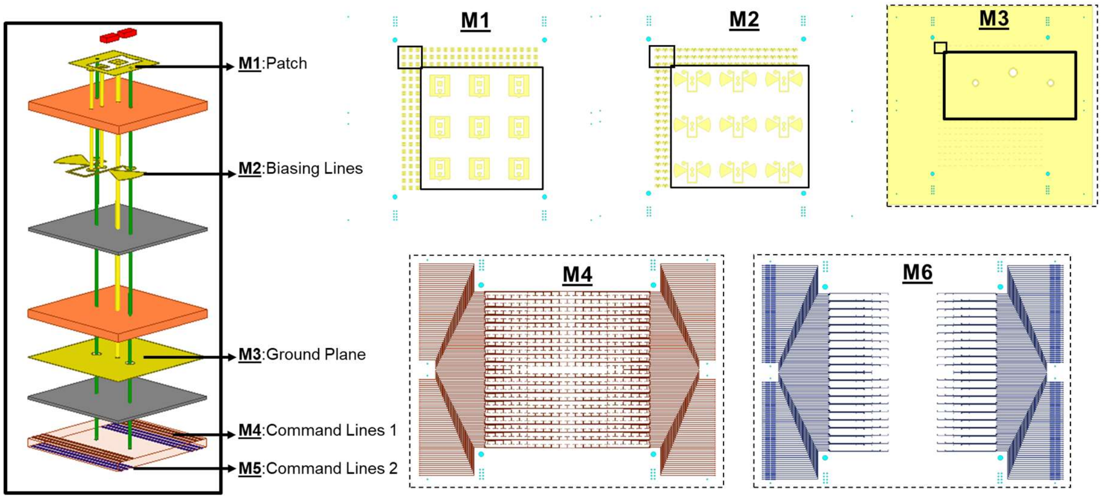

Figure 2-8 R-RIS UCs optimization with biasing network

The final prototype is shown in Figure 2-9 and the performance will be assesd in WP7.

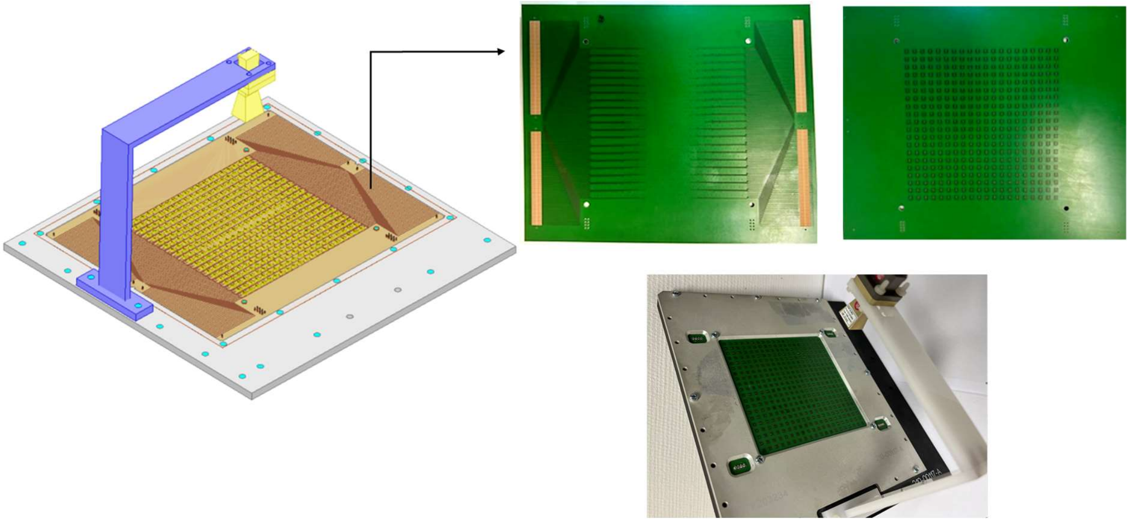

Figure 2-9 R-RIS prototype

2.3 Transmitive-Reflective RIS in the Ka band based on PIN diode

In D3.2 a Transimittive-Reflective RIS was implemented. The UC realizes a 1-bit phase quantization in Reflecting mode and 2-bits in transmitting mode. The prototype was measured in transmitting mode in anechoic chamber (Figure 2-10). Figure 2-11 show the measured gain pattern for different phase distributions, corresponding to different steering angle. Also the frequency dependence of the pattern is shown for an extreme steering, hilighting the beam squint effect.

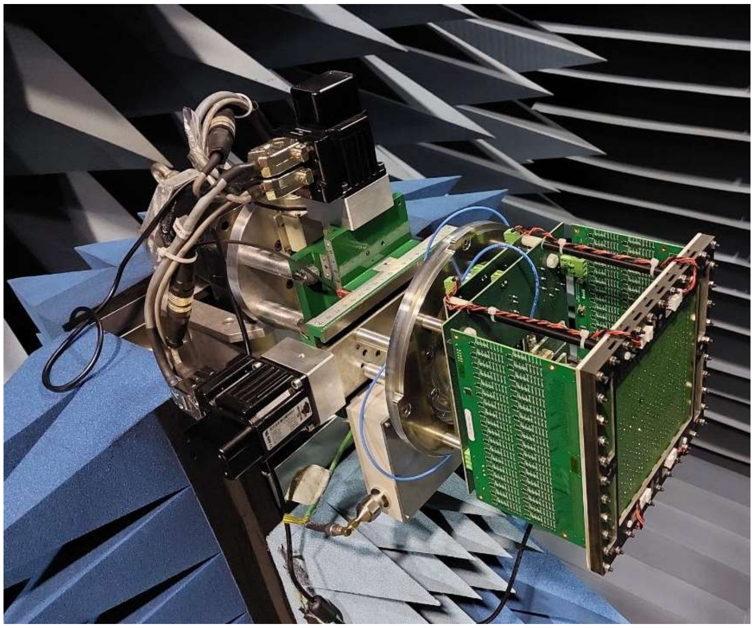

Figure 2-10 Transmitting-Reflecting RIS protoype characterization

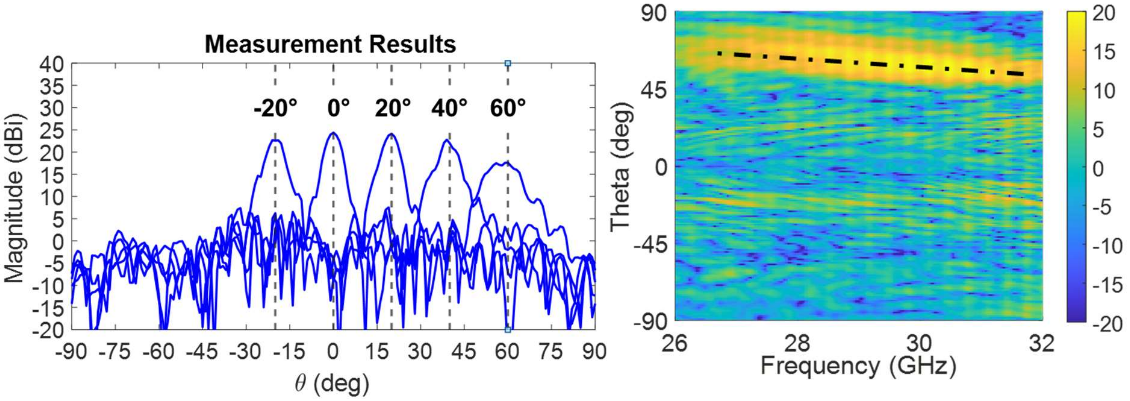

Figure 2-11 2-Bit Transmitting mode pattern for different steering angle (left) and freuqnecy dependeny pattern (right)

2.4 PIN Diode R-RIS prototype in 3.6-GHz-band

The proposed RIS is composed of a set of periodically arranged pixels with a λ/2 spacing. The single unit cell, shown in Figure 2-12(a), consists of a square copper patch printed on a Meteorwave 8300 substrate of thickness Ts = 0.51 mm, with relative permittivity $\varepsilon_R = 3$, and a dielectric loss tangent of tan(δ) = 0.0027. The patch is initially designed to provide resonance at f_0 = 3.6 GHz. As can be noticed from Figure 2-12(b), a spacer is placed between the patch layer and a bottom copper floor which acts as a ground plane (see Figure 2-12(c)). The 3 mm thick spacer has an extremely low relative permittivity ($\varepsilon_R = 1.04$), making it electromagnetically transparent and reducing the power dissipation. To provide a π-phase shift, a parasitic resonator P_V is placed very near to the main radiator in the Y direction. The mutual coupling between the patch and P_V is used to change the main radiator's resonance frequency and the reflected wave's phase in the desired 5G frequency band.

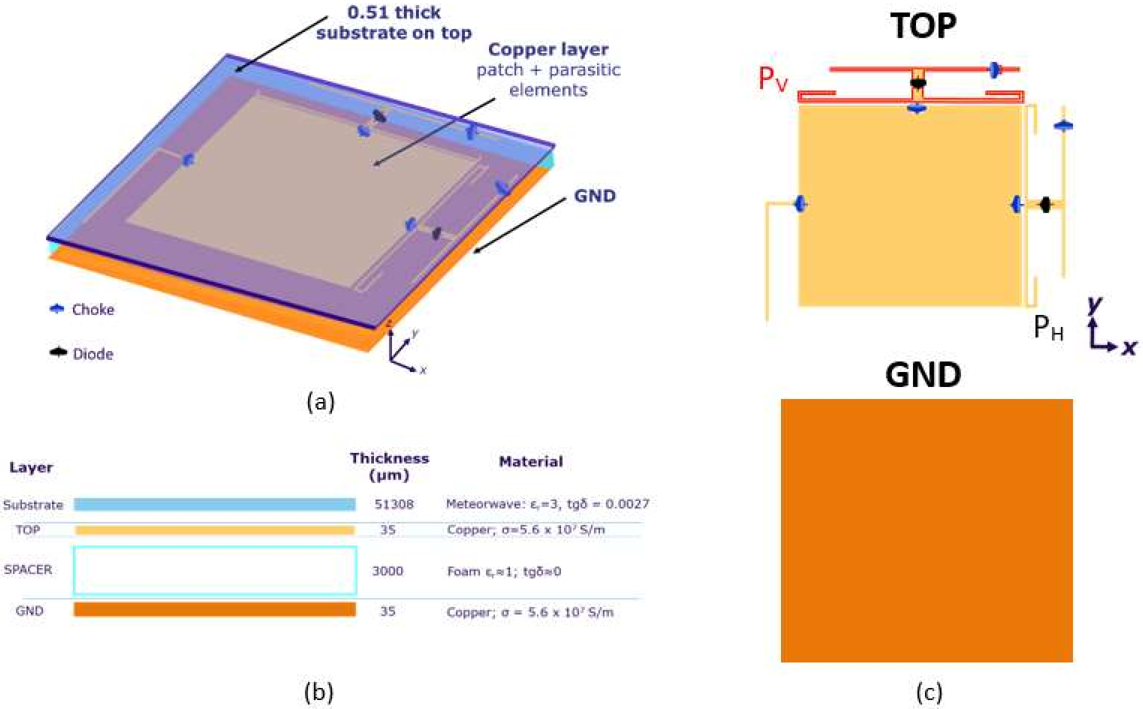

Figure 2-12. Proposed RIS unit cell: (a) 3D isometric view, (b) PCB stackup, and (c) copper layers

The switching between resonance states is performed by controlling the ON/OFF states of the PIN diodes (model: SMP1345 from Skyworks) integrated into the middle of the parasitic element. RF chokes are used to prevent the RF current from flowing to the ground. The PIN diodes and RF chokes are highlighted with black and blue arrows in Figure 2-12 (c), respectively. The electronic control of the PIN diodes is placed on the same side of the top layer. An additional parasitic element P_H has been added in the X direction to provide the horizontal polarization of the E-vector.

The proposed RIS geometry is shown in Figure 2-13(a). The reflection coefficient in the two different states is shown in Figure 2-13(b). As it can be seen, the reflector maintains a low dissipation (|S11| > - 2.4 dB) all over the 3.6 GHz band (3.4 - 3.8 GHz). In the desired 3.6 GHz frequency range the phase difference between ON and OFF states is between 163° and 206°. Figure 2-14 shows a snapshot of the unit-cell design. The full prototype is under fabrication.

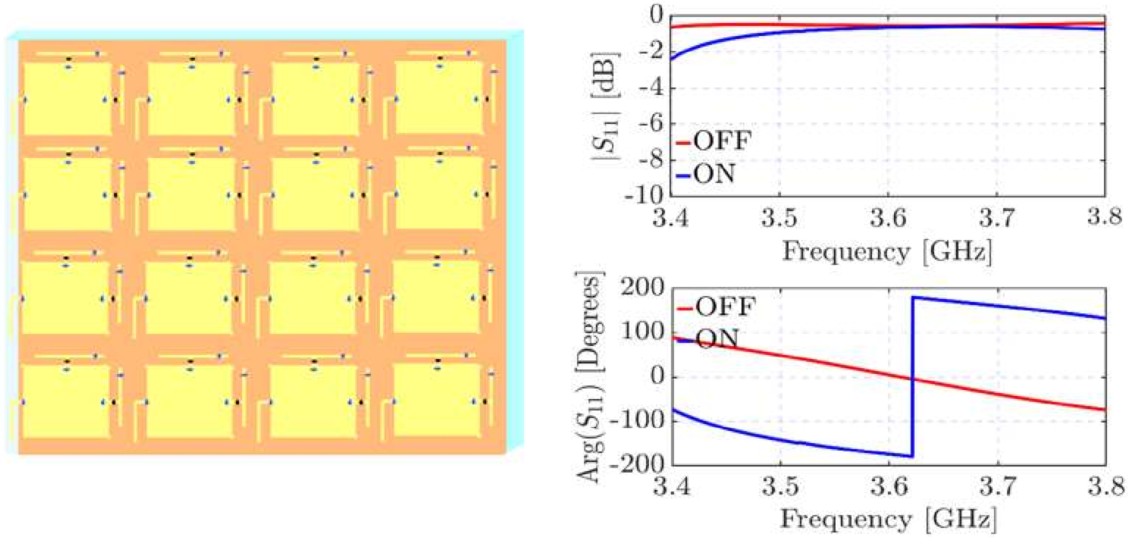

(a) (b)

Figure 2-13. (a) Proposed metasurface geometry. (b) Simulated amplitude and phase of the reflection coefficient of the RIS pixel in the operating range of frequency. Blue line represents OFF-state and red line represents ON-state of the pixel.

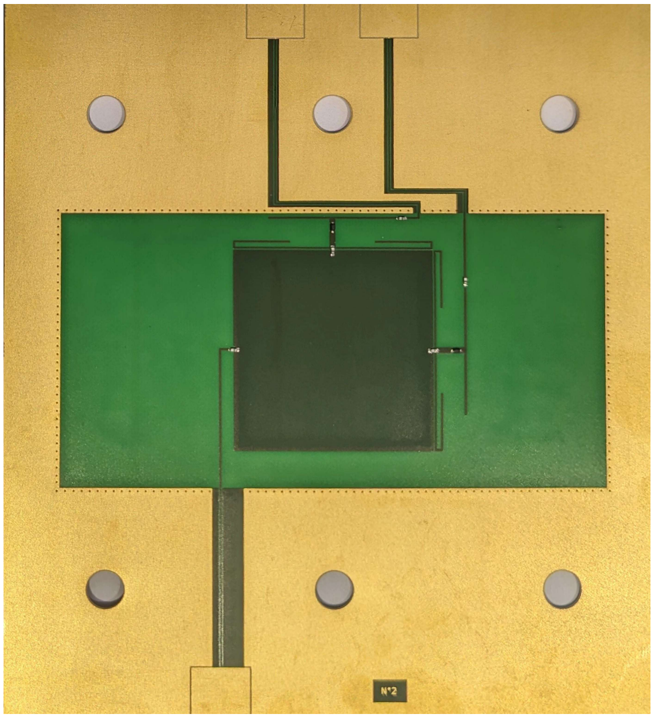

Figure 2-14. Picture of the Unit-cell design by Greenerwave

2.5 Varactor Based R-RIS design update in the Ka band

Considering the PCB manufacturer’s constraints, an updated design has been done. The main modification concerns the RF block (spirals) location: instead to be placed at the end of each arm of the cross, the spirals are shifted on the side of the arms just after the slot (Figure 2-15).

The connection between neighboring crosses is realized in the DC level behind the ground plane. The RF short circuit at the center of the cross and for each spiral is achieved by a shielded metallic via.

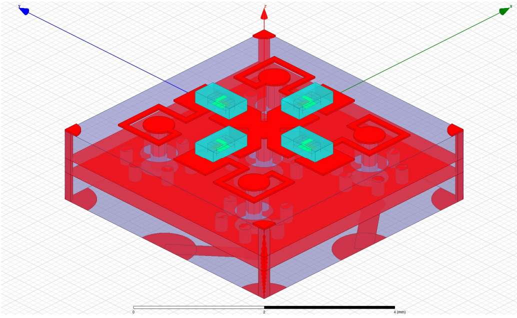

Figure 2-15 – UC updated design

The independent phase controls for two orthogonal polarizations are presented in Figure 2-16 where the required 300° of control are reached for a normal incidence. The amplitudes of the reflection coefficient are presented Figure 2-17where the typical behavior of this kind of unit cell is observed: a lower amplitude level at the resonance frequency (~ 0°). The coupling between the 2 orthogonal polarizations at normal incidence stays below -20 dB as required.

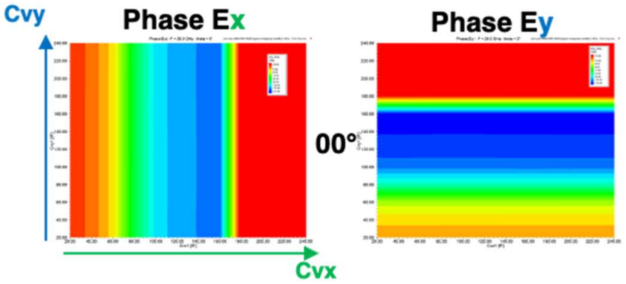

Figure 2-16 – Phase controls at 26 GHz and 0° of incidence

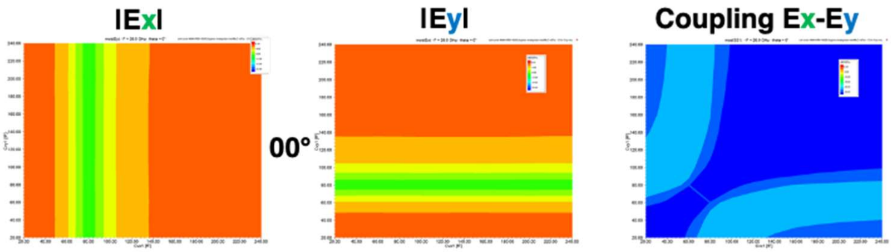

Figure 2-17 – Amplitude of reflection coefficient and polarization coupling at 0° of incidence

At lower incident angle (45°), the reflection phase coefficient control is maintained with 300° with some changes for one of the two polarizations (Figure 2-18) where the control is done in a reduced zone of capacitance. This modification is also observed on the coupling between the two polarizations where the map is not symmetric anymore, and the level is increased to -18 dB.

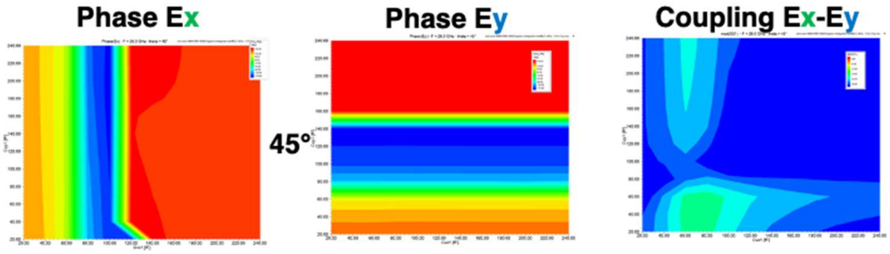

Figure 2-18 – Phase controls and polarization coupling at 45° of incidence

To keep the isolation above 20 dB after manufacturing, a composite cell, composed by 2x2 symmetric unit cells, will be used that allows an increase above 40 dB of the simulated isolation.

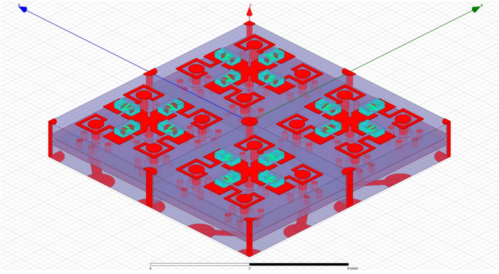

Figure 2-19 – composite unit cell: 2x2 symmetric unit cells.

A last checking is done by the PCB manufacturer before launching the manufacturing process of a 16x16 cells coupon. This coupon will be used to validate by experiments all the required RF performance of the controllable surface.

2.6 MEMS based R-RIS prototype for the 3.7 GHz band

This reflective RIS design is intended to operate in the 3.7 GHz band, with 200 MHz bandwidth. The unit cell consists of a dual-polarized patch antenna as a scattering element, backed by two phase shifters, one for each polarization.

The scattering element is built on two substrates, lower and upper. The lower substrate has a ground plane on its top side and the phase shifters and control circuitry on the bottom side. The upper substrate (not displayed in Figure 2-20) carries the patch element with dimensions 31.8 x 31.8 mm on its bottom side facing the ground plane and is suspended over the lower substrate with the help of spacers. This solution has been chosen to obtain as low losses as possible, since the resonator volume between the patch and the ground plane is formed entirely by air (see Figure 2-20).

Since the upper substrate covers the entire aperture of the scattering element, a low-loss Rogers RO4003C substrate is used to avoid additional losses. In contrast, a traditional FR4 is used for the lower substrate, because this part holds the entire structure and needs to be robust and reliable.

Two feeding pins for each polarization are attached to the patch and leading through the ground plane to the phase shifters. In addition, a third pin at the center of the patch provides DC connection to the ground layer.

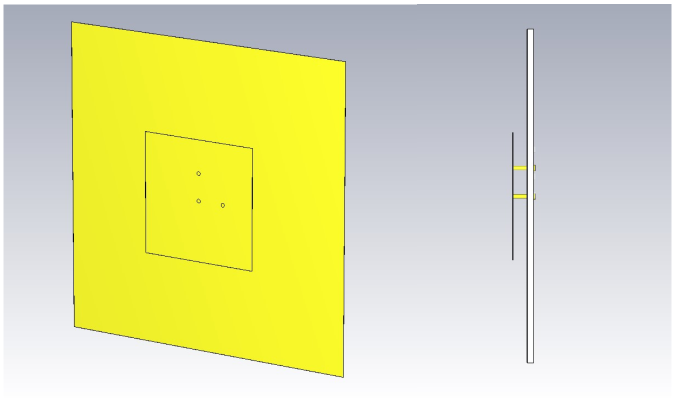

Figure 2-20 – Detail of the array element unit cell; circles show the feeding points of the patch.

The phase shifters are a novel design consisting of a low-impedance coaxial feed from the antenna side, a short coplanar waveguide with high-impedance, and two MEMS tunable capacitors with 5-bit control range (See Figure 2-21). The design balances maximum phase resolution with minimum loss.

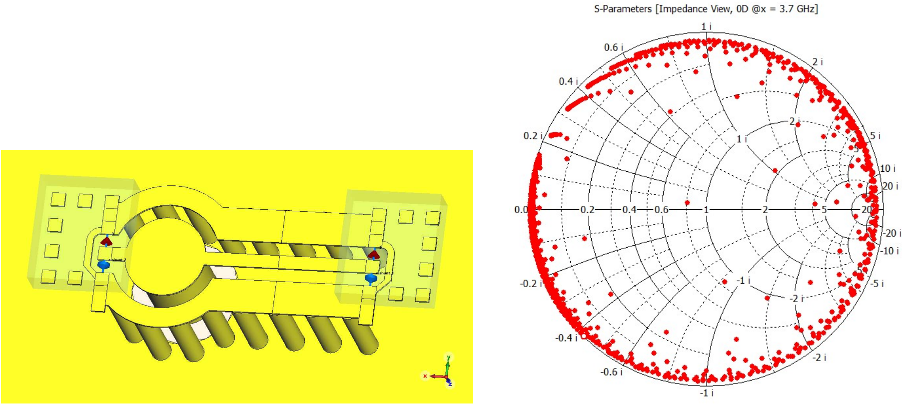

Figure 2-21 – Novel design of a phase shifter with two MEMS variable capacitors: 3D layout with substrate invisible (left) and simulated reflection coefficient in Smith diagram (right)

The unit cell has been simulated in CST Microwave Studio with incident wave incoming from boresight. Figure 2-22 shows the simulation results for various phase shifter settings. The designed loss of the scattering element is below 2 dB in the 3.6—3.8 GHz band and the phase covers the entire 360-degree range with good phase homogeneity across the frequency range.

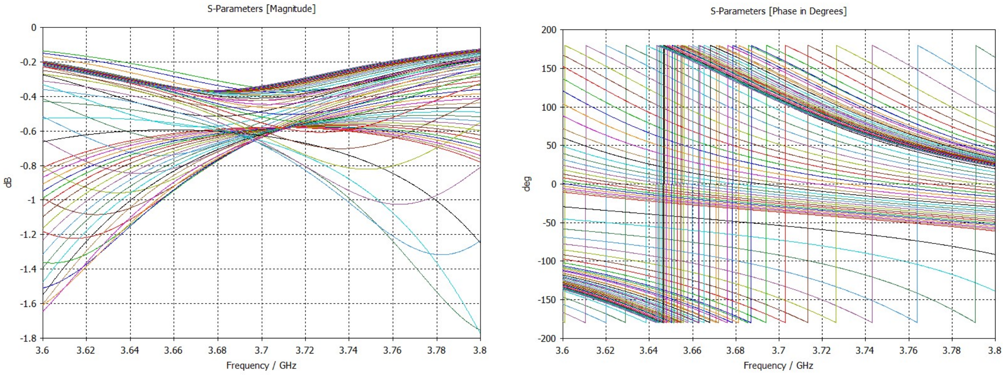

Figure 2-22 – Simulated reflection coefficient magnitude (left) and phase (right) of the boresight incident wave for various phase shifter settings.

A subarray with 4x4 pattern of the above-described unit cells forms the smallest building block of the entire RIS array (Figure 2-23). This choice was motivated by practicality and higher flexibility. It is much easier to design a control board for 4x4 subarray than it would be for larger patterns, while it is also possible to experiment with different sizes and shapes of the final RIS array. The aim is to produce 16 such subarrays and thus be able to form both 8x8, 12x12, and 16x16 RIS arrays.

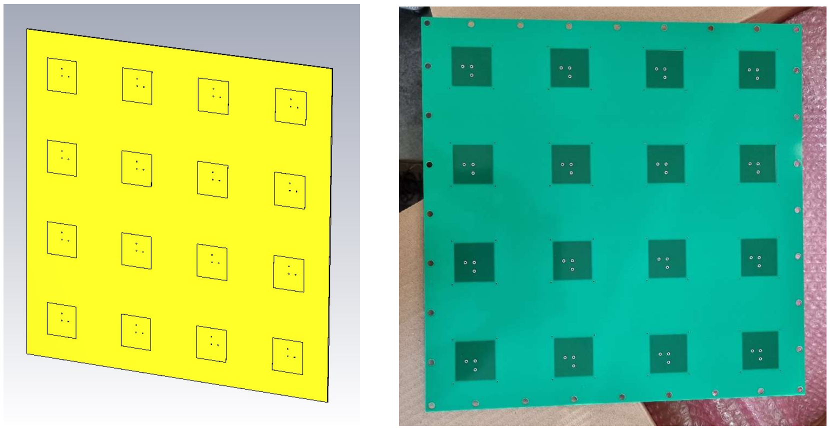

Figure 2-23 – 4x4 subarray of the reflective RIS array at 3.7 GHz.

The periodicity (pitch) of the subarray is 1 wavelength (81 mm). Despite the existence of grating lobes in this design, we intentionally chose higher than half-wavelength periodicity to have 4x larger area of the resulting RIS with the possibility of eliminating grating lobes via optimized coding of the loading phase shifts.

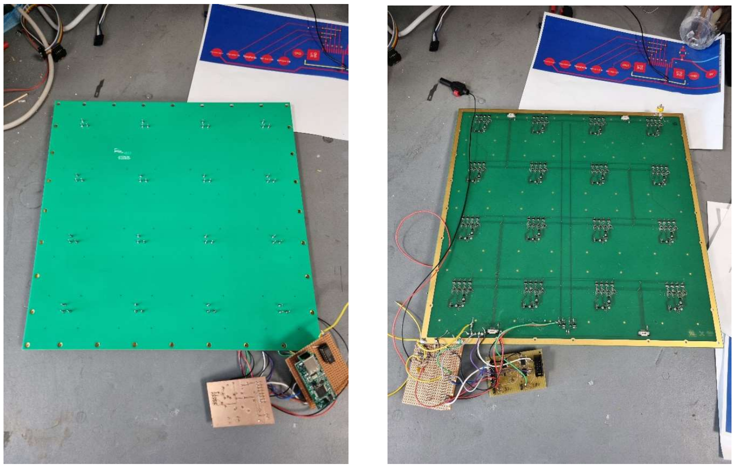

Figure 2-24 – 4x4 subarray prototype of the reflective RIS array at 3.7 GHz: top side with the feeding and grounding pins (left) and bottom side with the phase shifters and the control bus visible (bottom)

Figure 2-24 shows the produced 4x4 subarray from both sides. The control board was found faulty when first put into operation, but the error was identified. Currently we are testing the prototype, and planning to produce one more prototype of the 4x4 subarray for further tests, before finally placing the order on the remaining 15 subarrays.

2.7 mmWave RIS prototypes

2.7.1 V-band COTS based RIS

Chalmers made V-band RIS by modifying commercial V-band transceiver. The RIS has 16x4 beamforming antenna at both transmitter and receiver side respectively. The RIS can be configured for down-conversion V-band signal and then re-transmitted back at a same frequency, thanks to the common local oscillator design share between transmitter and receiver chain. Both transmitter and receiver have 1GHz baseband bandwidth and RF bandwidth from 58-71 GHz. Adding additional delay network and filter between received IQ ports and retransmission IQ input, additional phase compensation can be made for additional beamforming.

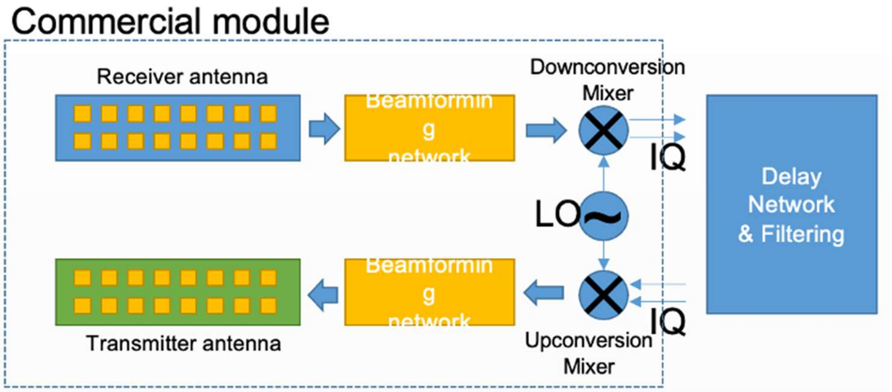

Figure 2-25. Block diagram of proposed V-band RIS prototype

The detail of the antenna array is shown in the Figure 2-26. The V-band RIS can be operated at 58-71GHz and receiver and transmitter beamforming of +/-20 degree with 1 degree resolution. And expected beamforming radiation patterns are plotted as well.

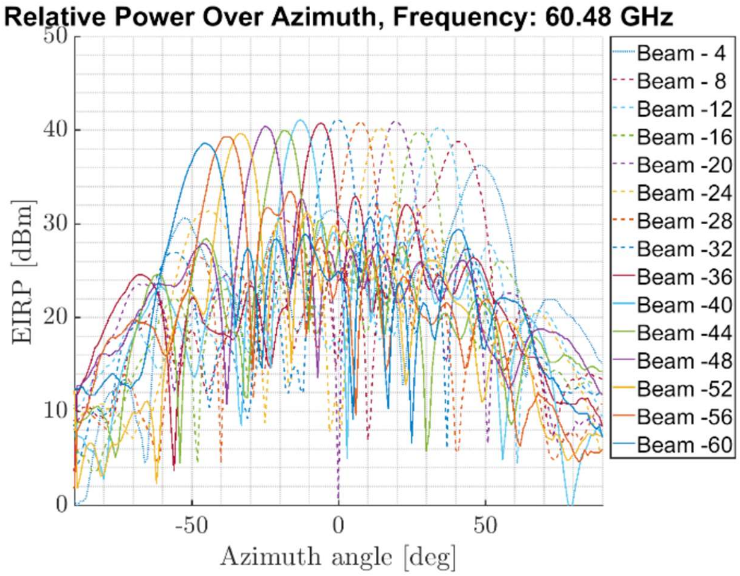

Figure 2-26. Antenna beamforming state adjustment and radiation pattern

2.7.2 D-Band prototype in 130nm SiGe BiCMOS technology

A D-band RIS unit cell is designed and fabricated in a 130nm SiGe BiCMOS process by Infineon. The design uses two bipolar transistors in a pi-network configuration for impedance manipulation (Figure 2-27). The Chip design also contains a D-band on-chip antenna. Using two controlling bias voltage, the reflectivity phase of RIS unit can be adjusted from 0-180 degree at 140 GHz. The size of the unit cell is 0.75mm X 0.93mm.

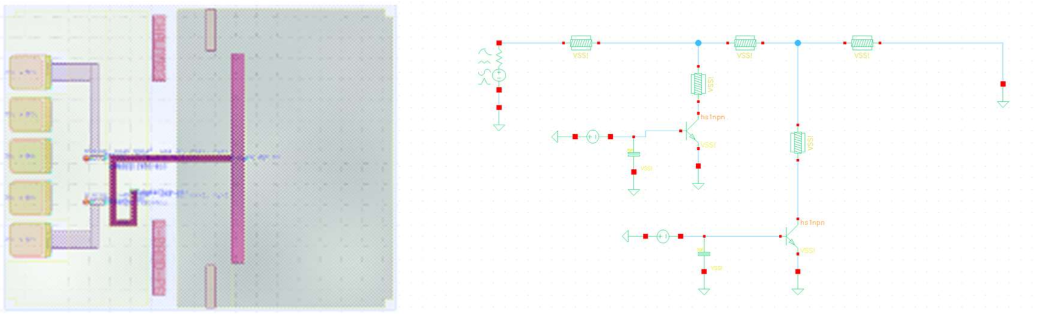

Figure 2-27. D-band RIS Unit Cell MMIC design

The designed RIS phase adjustment performance versus different bias condition is shown in Figure 2-28 with 120-160GHz frequency coverage.

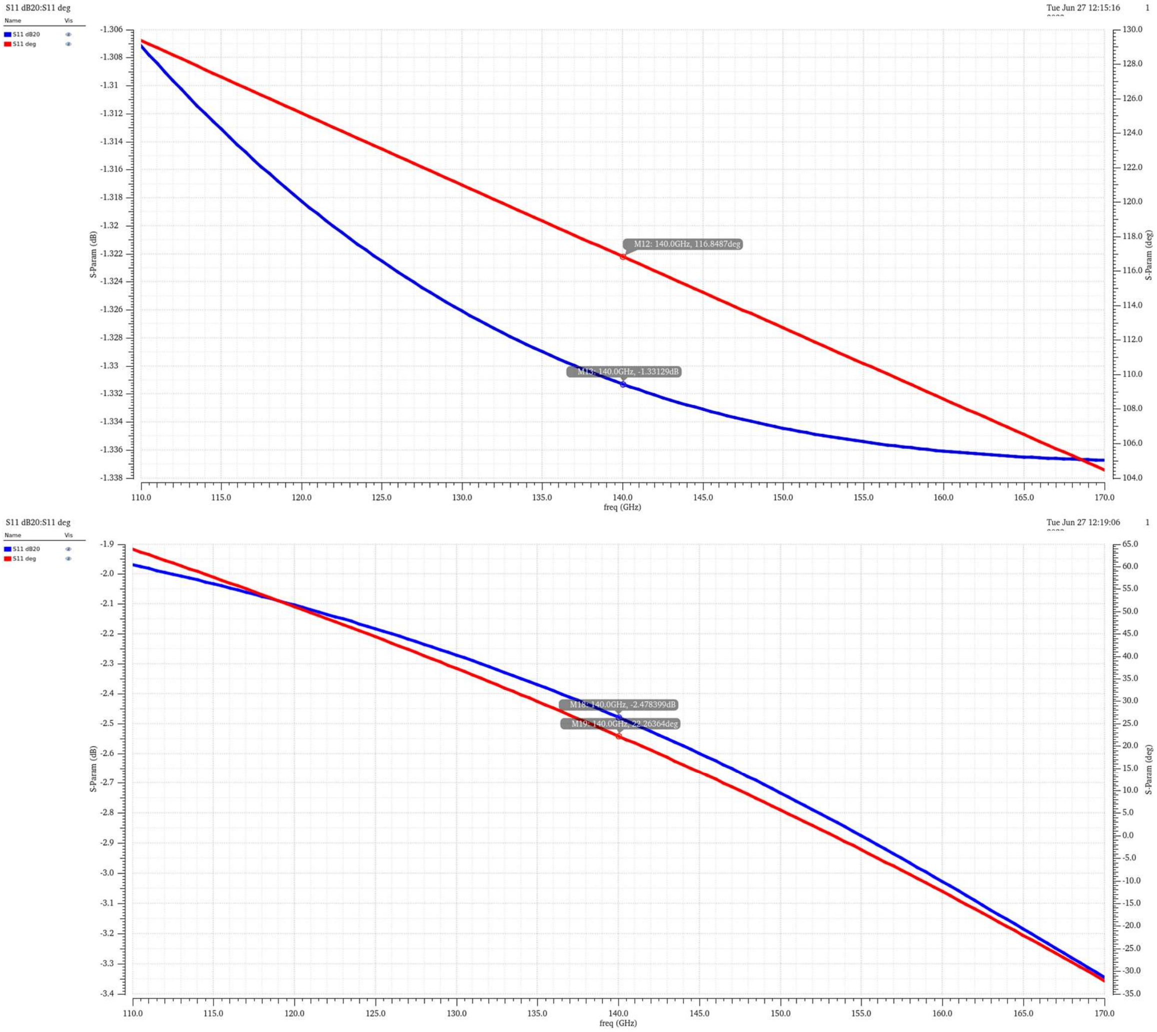

Figure 2-28 D-band RIS unit cell simulation result.

The unit cell with on chip antenna can also partially insert into a waveguide to form MMIC to waveguide port interfacing for connecting with a higher gain antenna. The assembly concept is shown in Figure 2-29:

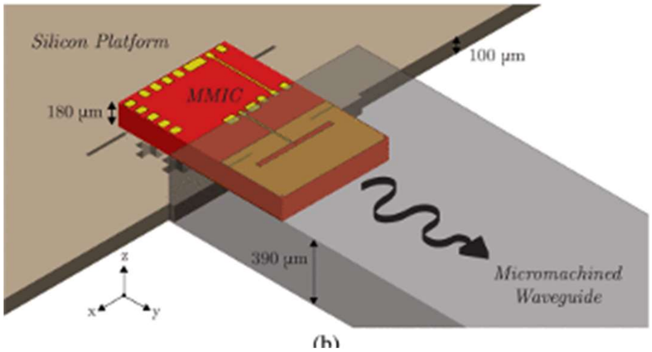

Figure 2-29 D-band RIS unit cell assembly into waveguide concept.

3 Advanced Models on RIS and UCs in free space

3.1 End-to-end impedance model final assessment

In this section we briefly review the model impedance model and discuss their extension based on scattering parameters. This leads to a global model that accounts for the interactions between multiple ports within the same cell, as well as among and with multiple ports within transmit/receive antenna arrays. It is worth remarking that this adds to the current effort of the scientific community to devise a physics-based model, with the impedance model being a first principle electromagnetic model that relates voltages and currents at the RIS/antenna ports. Remarkably, the scattering parameter extension allows for capturing the structural scattering and embed it into the original E2E model, thus overcoming the canonical minimum scattering approximation adopted originally to proof the principle. We will describe in detail the normalization procedure of port quantities that allows for achieving accurate predictions (based on limited, one-off, full-wave simulations) independent on cell geometry and technology. To remark this model advantage, we show a numerical verification for selected sub-6 and mmWave RIS structures. We will perform the validation for an E2E link with horn antennas and finite-size RIS with 2x2 and/or 4x4 unit cells. Comparisons will involve both the amplitude and the phase response of the RIS. A parametric analysis will be further presented with respect to distance and angle of the receiver with respect to the normal to the RIS, to appreciate the ability of the model of capturing the angular dispersion of the re-radiation process. We conclude the section with a simple RIS optimization of the load impedance. The optimization is aware of the mutual coupling that is encoded in the active impedance, although it is shown that the large RIS limit retrieves the predictions form PBC simulations. We show the model validation on configuration involving both sub-6 and mmWave prototypes designed and fabricated within the project.

3.1.1 Impedance model validation on mmWave R-RIS

In this section we analyse the applicability of the impedance model on reflecting RIS based on UC design presented in §2.2. The configuration model prototype operates in Ka-band. The simulation setup for model validation is represented in Figure 3-1. In a first step a full wave simulation is realized in the two states: namely “000” and “180” as depicted in Figure 3-1 (a)-(b). Then the diodes are replaced by lumped port to realize a multi-port simulation in order to retrieve the Z_{SS} active impedance matrix. Additionally, a simulation with PBC is performed Figure 3-1 (d).

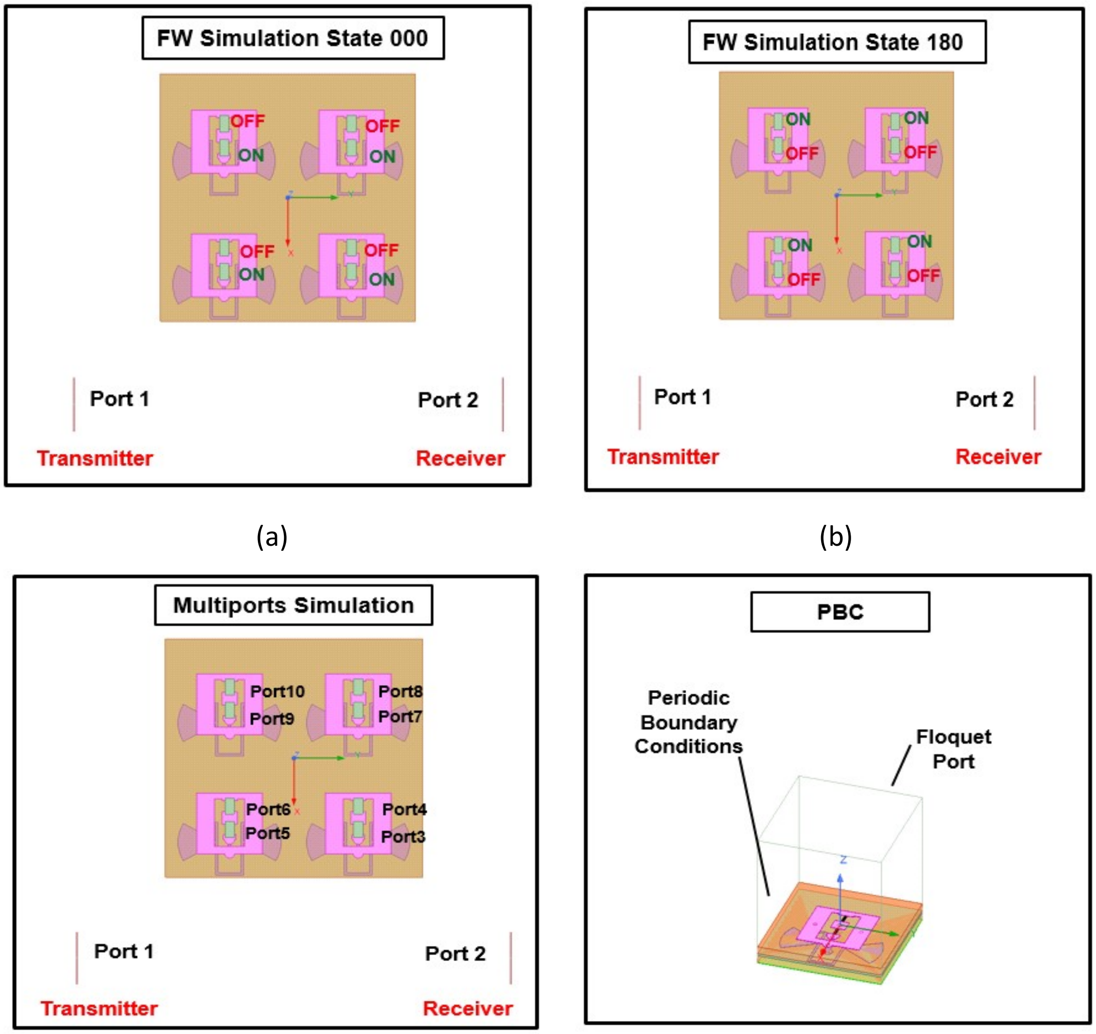

(a) (b)

(c) (d)

Figure 3-1 (a) Reflective RIS Configuration in state 0°, (b) Reflective RIS Configuration in state 180°, (c) Multi-ports Reflective RIS configuration, (d) PBC Reflective RIS UC

An in-depth study impedance model validation is based on the comparison of the two models. In the work [GD21], the impedance-based model proposed is:

$$\boldsymbol{H_{E2E}} = \boldsymbol{y_0}\,(\boldsymbol{Z_{RT}} - \boldsymbol{Z_{RS}}(\boldsymbol{Z_{SS}} + \boldsymbol{Z_{RIS}})^{-1}\boldsymbol{Z_{ST}})$$

3-1

Where $\boldsymbol{y_0}$ is a complex constant that accounts for the internal impedance of the voltage generator at the transmitter, the impedance at the receiver, the self-impedances of the transmit and receive antennas:

$$\boldsymbol{y_0} = \boldsymbol{Z}_L(\boldsymbol{Z}_L + \boldsymbol{Z}_{RR})^{-1}(\boldsymbol{Z}_G + \boldsymbol{Z}_{TT})^{-1}$$

3-2

With $\boldsymbol{Z_{RT}}$ is the mutual impedance between the transmitter Tx and the receiver Rx , $\boldsymbol{Z_{RS}}$ is the one between the receiver Rx and the R-RIS, $\mathbf{Z}_{\mathrm{RIS}}$ is the diagonal matrix including the equivalent impedances of the biasing circuits enabling the reconfigurability of the surface, and $\mathbf{Z}_{\mathrm{SS}}$ is active impedance of the R-RIS surface. This obviously simplifies the analytical calculation of the $\boldsymbol{H_{E2E}}$ channel transfer function matrix in Eq. 3-1 that is related to same assumptions, the $\boldsymbol{H_{E2E}}$ channel model Tx-RIS-Rx can be formulated in terms of the voltage generators at transmitter/Receiver antennas through an inverse matrix that explicitly depends on the active impedance with RIS impedance R-RIS unit cells. The scalar form of $\boldsymbol{H_{E2E}}$ and the corresponding simplification the general channel system will be compared with the general form of the impedance model.
Furthermore, in this work [R18] presents main formulas to convert parameters of multiport circuits. All Formulas are presented in matrix model form, and some assumption systems for global parameters have been discussed. This global matrix impedance model is used in order to analyze and optimize multiport systems.

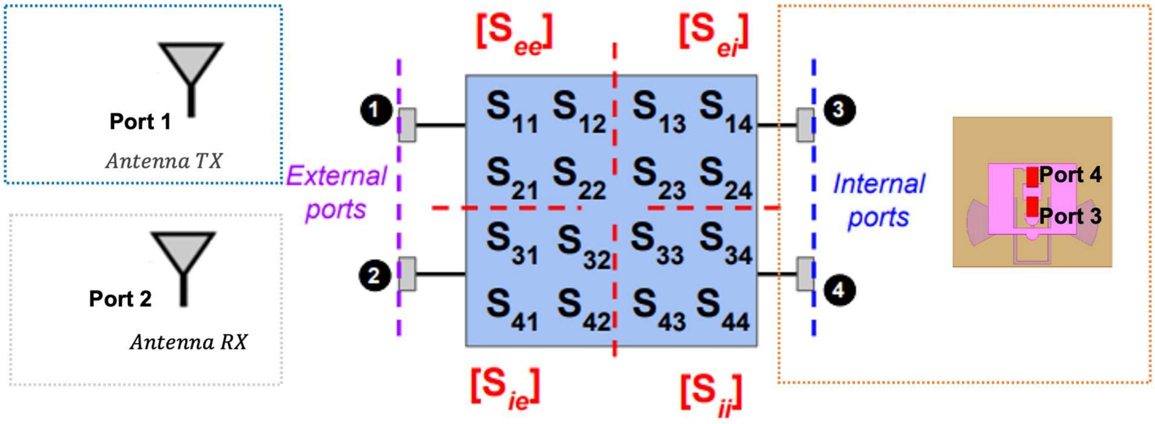

Figure 3-2 Multi-port representation of the end-to end link for a RIS unit cell: The ports are partitioned in external (excitation) and internal (circuital).

Based on the presented model of the partitioning multi-ports to external and internal ones that is illustrated in Figure 3-2, the Z $_{\text{Global}}$ matrix of the obtained channel system was expressed as:

$$[\boldsymbol{Z_{Global}}]=[\boldsymbol{Z_{ee}}]-[\boldsymbol{Z_{ei}}]([\boldsymbol{Z_{ii}}]+[\boldsymbol{Z_{L}}])^{-\mathbf{1}}[\boldsymbol{Z_{ie}}]$$

3-3

Which is valid for more sophisticated designs with multiple circuital ports, and where $\boldsymbol{Z_{ee}}$, $\boldsymbol{Z_{ii}}$, denote the sub-matrix of the external and internal ports respectively. Also $\boldsymbol{Z_{ei}}$, $\boldsymbol{Z_{ie}}$, denote the sub-matrix between the external and internal ports and $\boldsymbol{Z_{L}}$ the diagonal matrix of the multiport impedance terminated with a multiport at its internals ports.
In order to quantify the performance offered by RISs in classic representative communication networks, we need to validate the proposed $\boldsymbol{H_{E2E}}$ model.
On the one hand, we purpose to validate the proposed $\boldsymbol{H_{E2E}}$ model with the full-wave EM simulations. We consider the three scenarios presented in Figure1 and compare the transmission coefficients compared to those obtained by using a full-wave simulator. In the considered illustration, each R-RIS unit cells is assumed to be reconfigurable: each PIN diodes are set to the

000 state, i.e., the state (ON, OFF), and both diodes are set to the 180 state, i.e., the state (OFF, ON). The comparison between the full-wave simulations and the proposed HE2E channel model is reported in Figure 3-3 . The obtained results demonstrate that the proposed model provides a good accuracy for the considered single R-RIS UC case study.

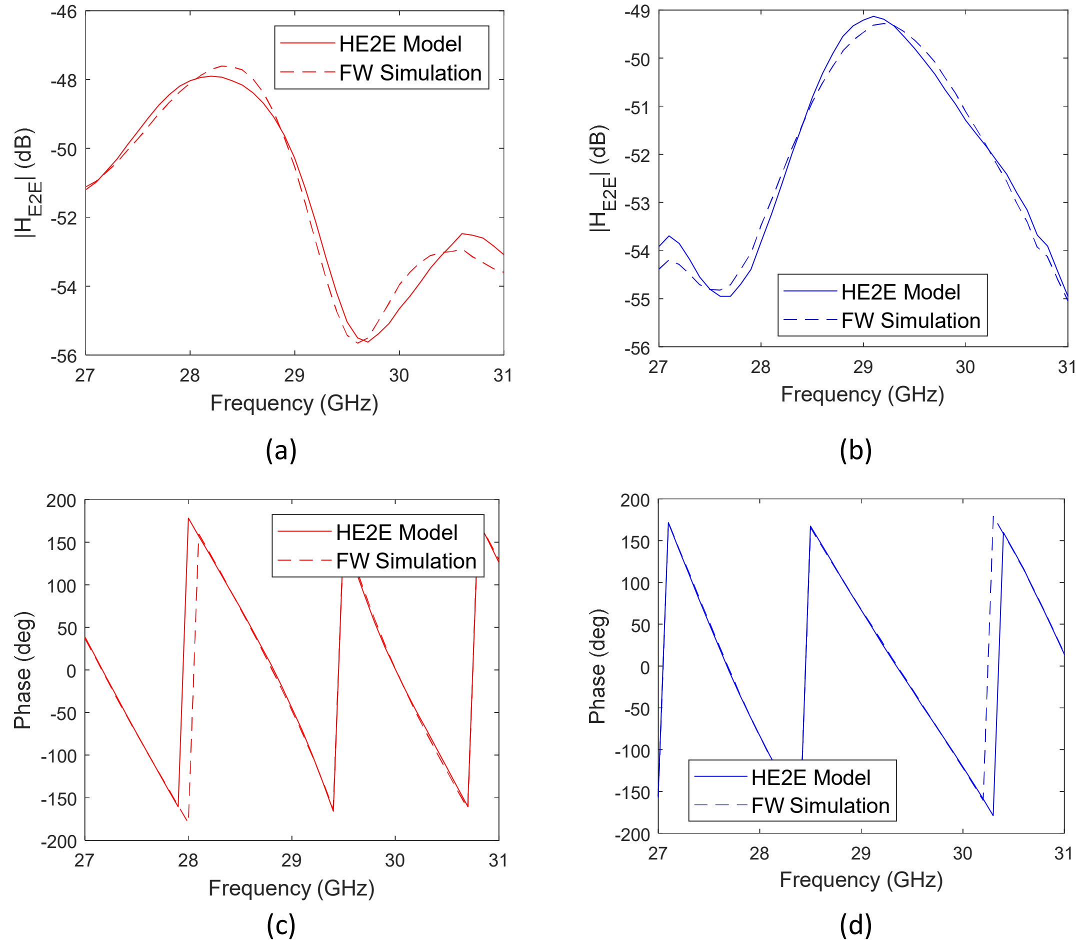

(a) (b)

(c) (d)

Figure 3-3 Comparison between full-wave simulations and the proposed model: Magnitude and phase responses at the operating frequency: (a,c) State 000 (red curves) , (b,d) State 180 (bleu curves).

On the other hand, we verify the global matrix model Z_{Global} obtained from the formulas in Eq. 3-3, as function of the Rx-RIS-Tx impedance properties induced by the RIS channel system. Each impedance matrix of the proposed channel system is modeled with an equivalent matrix impedance that is represented in [GD21]. Then, we could be extracted the required impedance term from commercial full-wave solvers. After that the $Z_{21Global}$ could be convert to $S_{21Global}$ to compare it with simulation one on both states. By assuming Z_0 is the characteristic impedance, the magnitude and phase responses retrieved by this model and a full wave simulation are compared. As expected, the impedance model plots referred to as global matrix model are in good agreement with the S_{21} extracted from the Ansys HFSS simulation with diodes in both state cases (Figure 3-4).

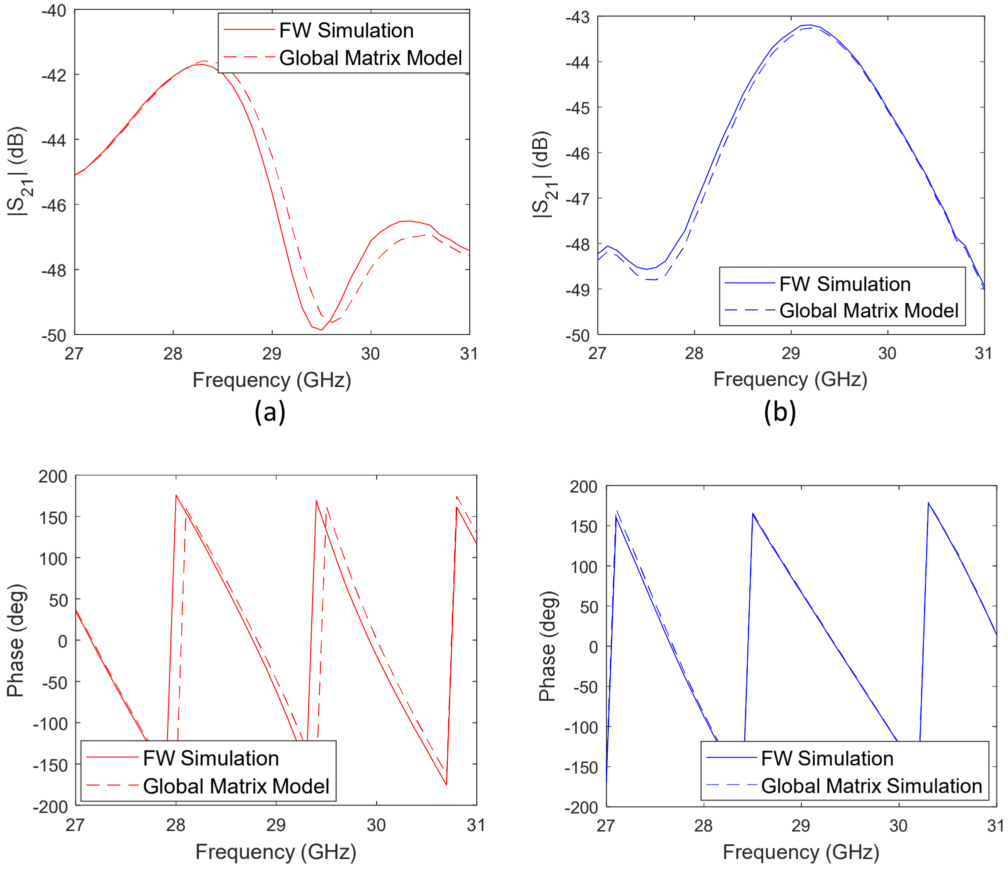

(a) (b)

(c) (d)

Figure 3-4 Comparison between the impedance model (blue solid curve) and the global impedance extracted from HFSS (solid black curve) in case: (a,c) 0° and (b,d) 180°.

At this point, in order to find a voltage expression of the global impedance matrix, we can use the parameters calculated within Eq. 3-4 and Eq. 3-5 by adopting a simple approach related to the RIS configuration. These two voltages terms, $V_2 = -Z_{Lr}\, I_2$, and $V_1 = V_G - Z_G\, I_1$, are considered as correct parameters for the model converting and assumed as known but constant with respect to frequency.

$$V_1 = Z_{11} I_1 + Z_{12} I_2$$

3-4

$$V_2 = Z_{21} I_1 + Z_{22} I_2$$

3-5

$$H_{Global} = \frac{Z_{21} - \frac{(Z_{22}Z_{21})}{(Z_{22}+Z_{Lr})}}{(Z_{11}+Z_G) - \frac{(Z_{12}Z_{12})}{(Z_{22}+Z_{Lr})}} \tag{3-6}$$

We compared H_{Global} to the H_{E2E} model with the tuning parameters appropriately chosen to achieve this End-to-End channel system. The comparison simplest with H_{E2E} model or Global matrix model adopting the same transfer function form is shown in Figure 3-5 . A same accuracy with respect to the magnitude in case 0° is present, and concerning the reflection phase the two curves are almost superposed. We can say that the terms of impedance that are neglected and simplified in the H_{E2E} does not affected the model.Therefore, we observe that the neglected term among the H_{Global} model has imperceptible impact on the final H_{E2E}. The results substantiate the proposed End-to-End model, which compared to global matrix model and the full wave simulation.

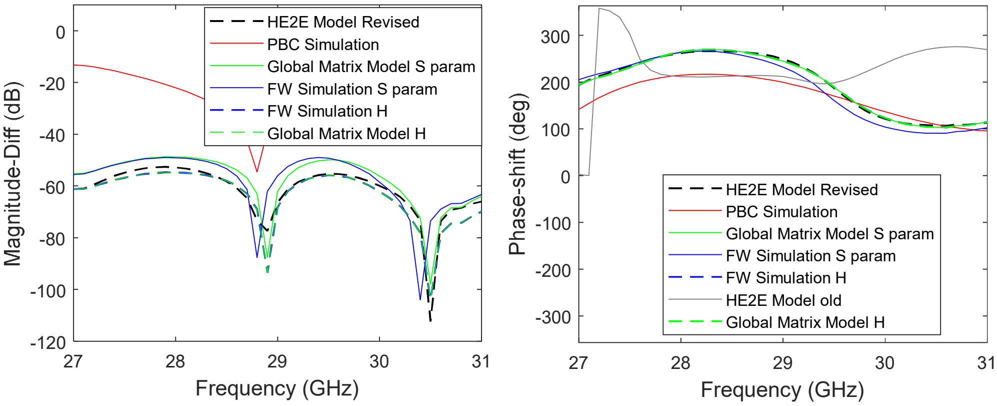

(a) (b)

Figure 3-5 Comparison between the impedance models and FW simulationof RIS UC: Magnitude_difference (a), Phase_shift (b).

A previous validation of the model presented in D3.3 and based on the analysis of this shift when using the model as compared to the full wave simulation. The previous results (i.e H_{E2E} model old) is incompletely in agreement especially at the central frequency. On the extremity of the band, a larger disagreement is found, and the reasons are related to the made assumptions like the mutual impedance effect, the normalization of all terms of impedance and the primer a scalar version of $\boldsymbol{y_0}$ that was supposed equal to 1.

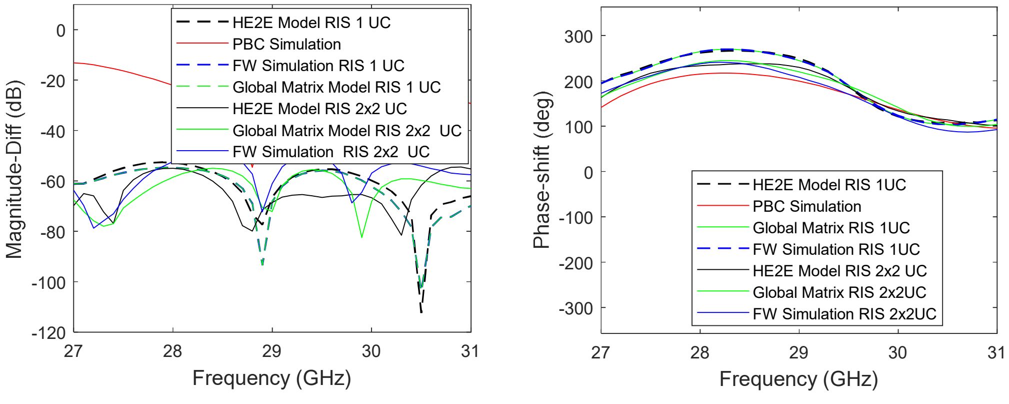

(a) (b)

Figure 3-6 Comparison between the impedance models and FW simulation of Finite RIS: Magnitude_difference (a), Phase_shift (b).

Additionally, in Figure 3-7 , we show the results of the two models Vs. full wave simulation in the case of single UC and finite 2×2 RIS. A final validation of the model is based on the analysis of this shift. The phase-shift of the model agrees with the full-wave simulation especially in the case of single UC configuration. On the finite 2×2 RIS and by increasing the number of UCs a good convergence to PBC simulation is found, and the reasons are related with an increased the number of UC in R-RIS structure.

In order to evaluate the RIS effect, we considered two cases with all UCs at state “000” or, alternatively, “180”. The phase difference between the two channel cases is shown in Figure 3-7, when using horn antennas as transmitter in broadside direction and the receiver in observation angles 0°, 30° and 40°. It can be shown that the phase difference is close to the expected ones. Despite the finite dimensions of the RIS, the phase shift is very close to the one obtained from PBC simulation. Additionally, one of the horn antennas was moved at a different angular position. While the phase difference changes according to the phase, this is still close to the 180° shift expected.

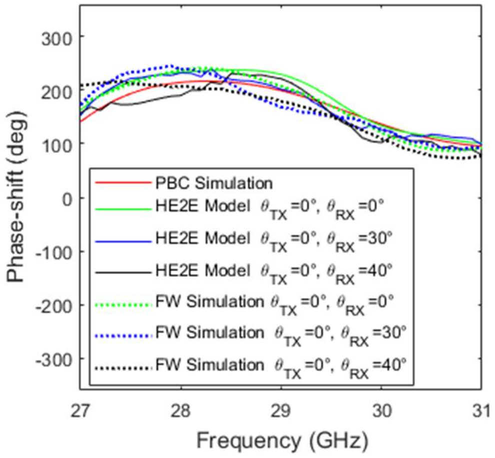

Figure 3-7 Phase-shift with finite RIS and two horn antennas for different observation angles.

3.1.2 Impedance model validation on sub-6GHz RIS

The aim of this section is to validate the impedance model on the a binary reflecting RIS based on the Greenerwave unit cell design operating at 5.2 GHz and already showcased in D3.2.The simulation layout for the RIS prototype briefly consists of two co-polarized linear dipole antennas acting as a transmitter and a receiver respectively. The two dipole antennas are placed in the far-field of a reflective RIS consisting of 2×2 UCs. The Tx and Rx dipole antennas, as well as the RIS, operate at a central frequency of 5.2 GHz; the numerical simulations were therefore performed over a wide frequency bandwidth ranging from 4 to 6 GHz. The UC design used to conveniently simulate this finite size reflective RIS has been developed by GNW and has the topology of two folded dipoles to cope both the polarizations, a suitable printed matching network both placed on a FR4 substrate backed by a ground plane. The proposed UC is therefore presented in Figure 3-8 along with the equivalent circuits of the pin diodes in the ON and OFF state respectively. The prototype has been simulated through Ansys EM HFSS 2022©. The method that we used to verify the E2E model starts by extracting the impedance matrices as described in [GR21]. The interactions between Tx/Rx antenna and RIS UCs are calculated by a frequency domain solver in the form of open circuit impedance matrices. It is interesting to point out that to build the E2E matrix, we have defined discrete ports within the UCs. Those ports are left in open circuit or terminated by an equivalent circuit of the pin diode in turn. Given that each UC has two pin diodes, one for each wave polarization, only the folded dipoles co-polarized with the Tx and Rx dipoles will be used for RIS reconfiguration. However, the general impedance matrix of the E2E system in this configuration consists of 10 ports in total: 8 that will be used for RIS configuration via pin diodes, with the 8 diodes replaced by discrete ports, plus the two feed ports of the dipole antennas. The resulting impedance matrix will therefore have dimensions 10×10.

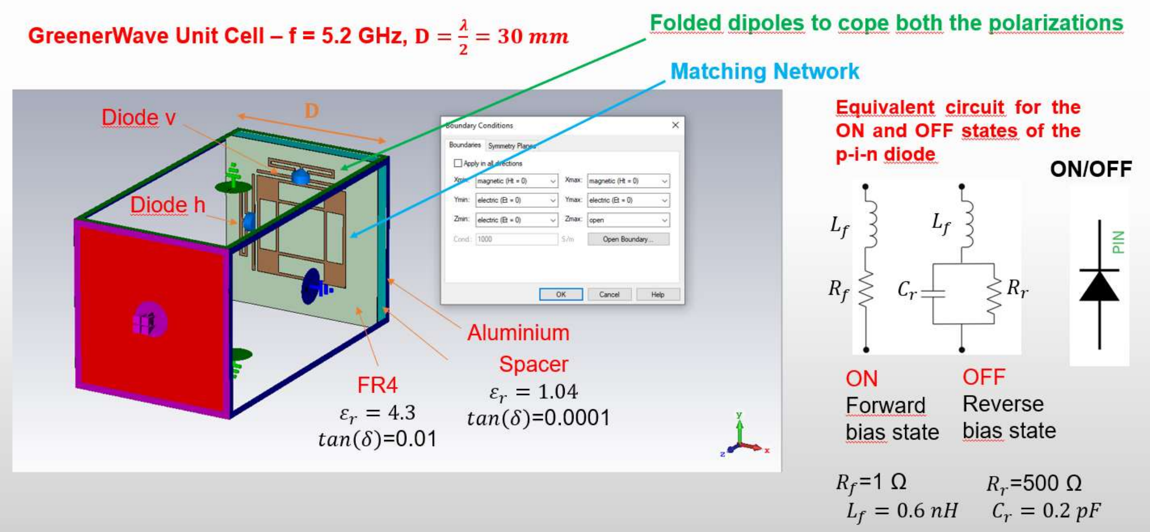

☐ Apply in all directions
Xmin: magnetic (Ht = 0) Xmax: magnetic (Ht = 0)
Ymin: electric (Et = 0) Ymax: electric (Et = 0)
Zmin: electric (Et = 0) Zmax: open
Cond.: 1000 S/m

R_f=1 Ω R_r=500 Ω
$L_f = 0.6\ nH$ $C_r = 0.2\ pF$

Figure 3-8 On the left a schematic View of the proposed reflective RIS 1 bit UC. On the right the Equivalent lumped-elements models of the pin diode in the ON and OFF state.

The simulation setup adopted to validate the model is represented in Figure 3-9 (a). Firstly, two full-wave simulations in the two possible states are performed: namely "000" and "180" as shown in Figure 3-9 (c)-(d). In the second step, the lumped ports are placed instead of the diodes to realize a multi-port simulation for retrieving the Z_{SS} active impedance matrix, Figure 4-4 (b). Moreover, a PBC simulation is performed.

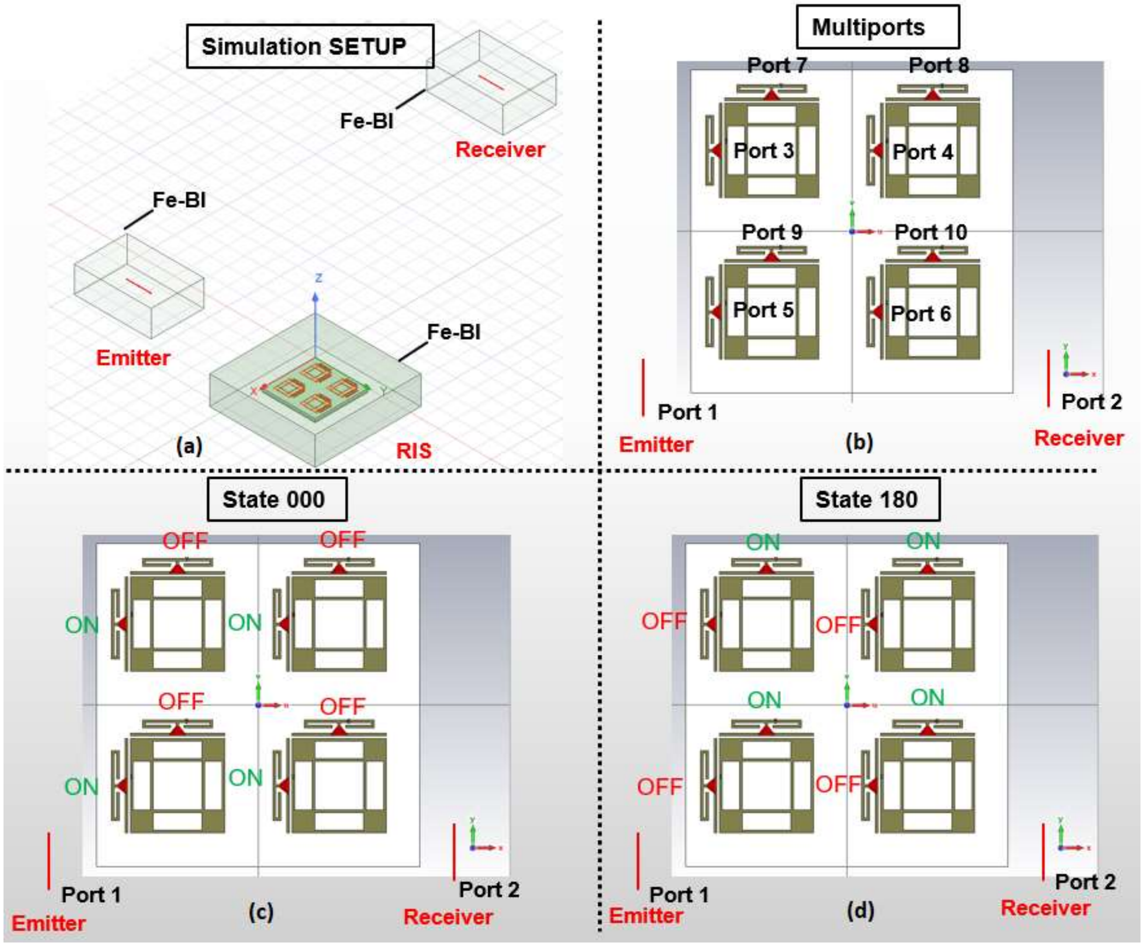

Figure 3-9(a) Simulation layout of the reflective RIS prototype provided by Greenerwave, (b) Multi-ports reflective RIS configuration, (c) Reflective RIS Configuration in state 0°, (d) Reflective RIS Configuration in state 180°.

To summarize, the approach employed to validate the E2E transfer function model, starts by determining all impedance matrices comprised in the HE2E model and in particular Z_{RIS} that is the impedance of the reflective RIS structure obtained by switching diode states, Z_{SS} or the active impedance obtained with discrete ports which replaced the pin diodes in a particular ON/OFF state. To calculate the H-matrix, the mutual impedances between the Receiving and Transmitting antennas Z_{RT}, between the Tx antenna and RIS Z_{ST} , and between the receiving antenna and RIS or Z_{RS} will also be considered. To generate all impedances described in the use of the general HE2E model, all scenarios are simulated in Ansys EM HFSS can be described as follows in Figure 3-9:

- Scenario 1: In this configuration, all active elements in the reflective RIS UC are changed by lumped ports and the dipole antennas are also excited with lumped ports: the general impedance matrix with all ports (10 ports) is extracted with MATLAB to calculate the E2E transfer function model H_{E2E} of the system. The resulting active impedance Z_{SS} matrix has 10x10 dimensions (8 ports in the R_RIS Structure and 2 in the dipole antennas)
- Scenario 2: The second configuration is presented by active elements placed in 2x2 reflective RIS UCs which are biased in State 000 and only the dipole antennas R/T are

excited with lumped ports. Consequently, $\boldsymbol{S_{21}}$ or the scattering receiver-transmitter parameter is extracted to be compared with H_{E2E} calculated from the simulation Multi-ports elements. Where $H_{E2E} = Y_0(Z_{21} - [Z_{23}\ Z_{24}]\left(\begin{bmatrix} Z_{33} & Z_{34} \\ Z_{43} & Z_{44} \end{bmatrix} + \begin{bmatrix} Z_{L3} & 0 \\ 0 & Z_{L4} \end{bmatrix}\right)^{-1}\begin{bmatrix} Z_{13} \\ Z_{14} \end{bmatrix} = \frac{\boldsymbol{v_2}}{\boldsymbol{v_1}}$

- Scenario 3: The third configuration is presented by the active elements placed in 2×2 reflective RIS UCs which are biased in State 180 and only the dipole antennas R/T are excited with lumped ports. Therefore, the impedance the $\boldsymbol{S_{21}}$ is extracted to be compared with the E2E transfer function model H_{E2E}.

We report in the following the comparison between the predicted E2E transfer function obtained with the proposed model, applied to the reflective RIS design and the $\boldsymbol{S_{21}}$ extracted from Ansys HFSS obtained with simulations of the loaded RIS in the two states. The simulation results of impedance model have been extracted with a Matlab script, which outputs the total scattering or impedance matrix of the multi-port configurations to validate the E2E transfer function model HE2E. As we can see from Figure 3-10, the impedance plots referred to as proposed model are in good agreement with the $\boldsymbol{S_{21}}$ extracted from the Ansys HFSS simulation with diodes in the $0°$ and $180°$ state cases. Furthermore, we have also extracted active impedance from the UC placed in PBC and used this approach to validate the proposed HE2E transfer modal in the infinite case of reflective RIS arrays.

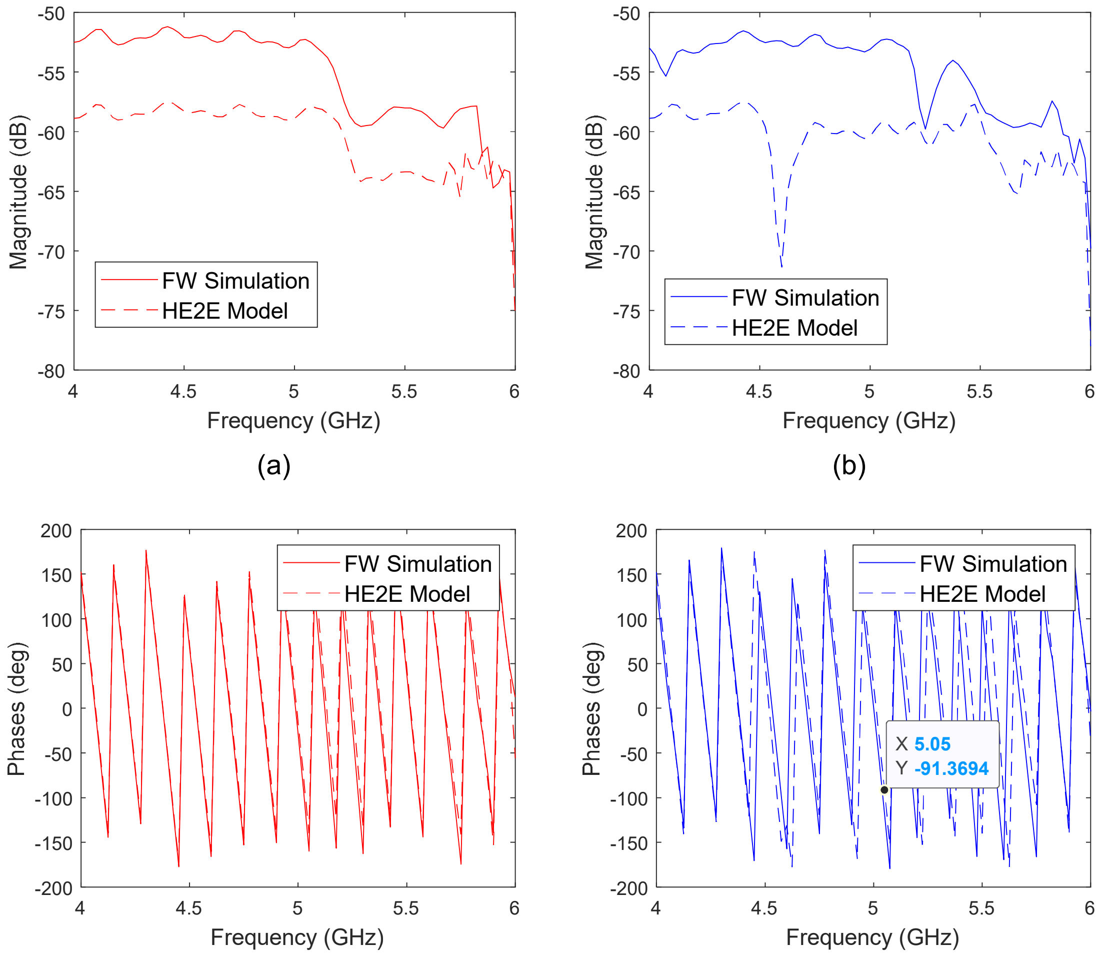

(a) (b)

(c) (d)

Figure 3-10 Comparison between full-wave simulations and the proposed model: Magnitude and phase responses at the operating frequency: (a,c) State 000 (red curves) , (b,d) State 180 (bleu curves).

As discussed above for reflective RIS at mm-wave frequencies, we will present similar results here by following the decomposition used in [R18]. We can adopt this global matrix impedance model to validate furthermore the end-to-end model.
As done previously, we compare the global matrix model Z_{Global} as function of the impedance properties extracted by the Tx-RIS-Rx overall channel. The impedances matrix of this channel system are modeled with equivalent matrix impedances as states in [GD21]. As a second step, the required impedance term can be extracted after the full-wave simulation. This $Z_{21Global}$ is then converted to $S_{21Global}$ to compare it with simulation one on both states. The magnitude and phase responses retrieved by this model and a full wave simulation are compared. As a result, likewise the case of classical expression of HE2E, the global matrix model plots are in good agreement with the S_{21} extracted from the Ansys HFSS simulation with diodes in both state cases (Figure 3-11).

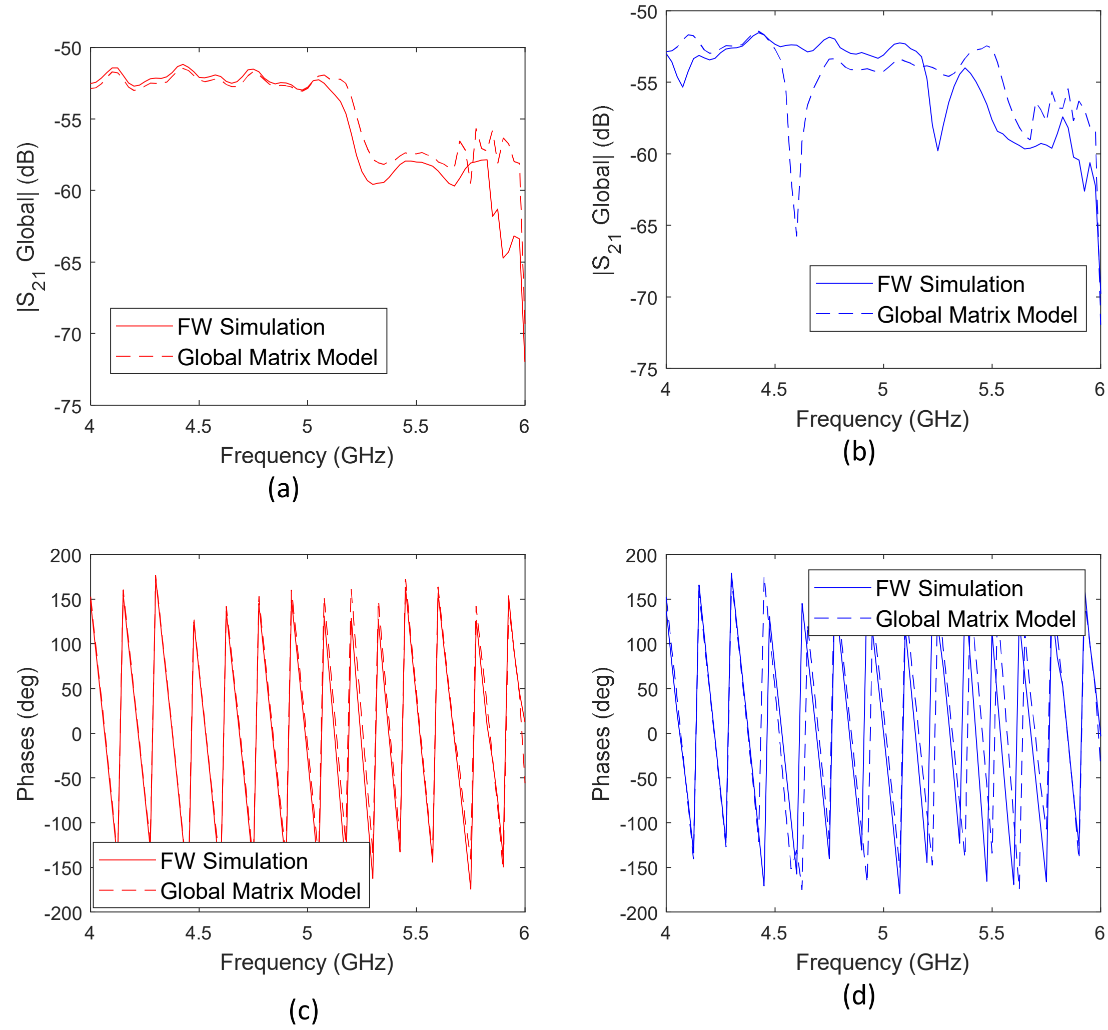

(a)

(b)

(c)

(d)

Figure 3-11 Comparison between full-wave simulations and the proposed model : Magnitude and phase responses at the operating frequency: (a,c) State 000 (red curves) , (b,d) State 180 (bleu curves).

Revisiting the steps previously described for the unit-cell at mm wave frequencies, to express the global impedance matrix in terms of voltages, we can compare the H_{Global} to the H_{E2E} model with the tuning parameters appropriately chosen to achieve this End-to-End channel system. The comparison simplest with H_{E2E} model or Global matrix model adopting the same transfer function form is shown in Figure 3-11. A same accuracy with respect to the magnitude in case 0° is present, and concerning the reflection phase the two curves are almost superposed. We can say that the terms of impedance that are neglected and simplified in the H_{E2E} does not affected the model. Thus, we observe that the neglected term among the H_{Global} model has imperceptible impact on the final H_{E2E}. The results substantiate the proposed End-to-End model, which compared to global matrix model and the full wave simulation.

We perform now an updated validation of the model presented in D3.3 int terms of phase-shifts. The previous results were not incompletely in agreement especially at the central frequency. The reasons were related to the normalization of the all terms of with $\boldsymbol{y_0}$ that was supposed equal to 1.

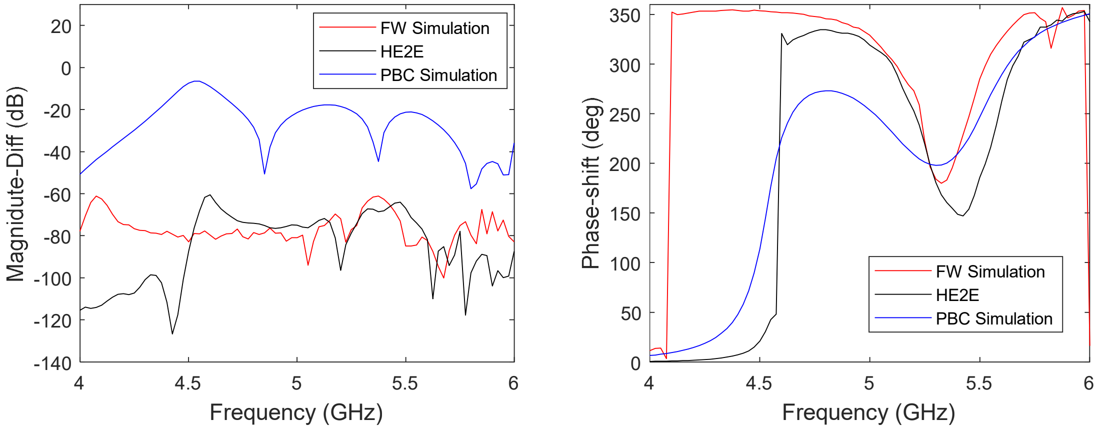

(a) (b)

Figure 3-12 Comparison between the impedance models and FW simulation of Finite RIS: Magnitude_difference (a), Phase_shift (b).

In Figure 3-12 we show the results of the two models Vs. full wave simulation in the case of single UC, considering even the PCB simulation. A final validation of the model is based on the analysis of this shift. The phase-shift of the model is in fair agreement with the full-wave simulation especially in the case of single UC configuration.

3.2 **Resonant model validation**

The presence of frequency selectivity and the resonant behaviour of the RIS unit cell, requires a dedicated analysis to understand the Band of Influence (BoI) of the RIS – as defined in D6.2. The RIS is operated at a selected (design) central frequency but can influence a range of nearby frequencies that is substantially wide (in the sense that can go beyond the individu-al/aggregated user channel prescribed by 5G standards).

In D3.3 initial work has adopted Lorentzian models of the reflection coefficient originally developed for metasurface-assisted imaging and focusing [KSI+22]. Recently, we have analysed an 'inverse' Lorentzian model that was proposed for reflect-array antennas [KYE13]. While the former model could be applied to characterise transmissive RISs, e.g., the recent OMNI-RIS structures, here we have focused on a perturbative approach that allowed for extending the latter model to reflective RISs. This has led to the expression, for the nth cell of the RIS

$$[\boldsymbol{\Gamma}(\boldsymbol{f})]_{\boldsymbol{n},\boldsymbol{n}} = \frac{\frac{1}{Q_n^{rad}+\Delta Q_n^{rad}} - \frac{1}{Q_0+\Delta Q_{0,n}} - \frac{2j(f-f_n^r-\Delta f_n)}{f_n^r+\Delta f_n}}{\frac{1}{Q_n^{rad}+\Delta Q_n^{rad}} + \frac{1}{Q_0+\Delta Q_{0,n}} + \frac{2j(f-f_n^r-\Delta f_n)}{f_n^r+\Delta f_n}}$$

3-7

More precisely, a fitting procedure adopted to determine ΔQ_n^{rad}, $\Delta Q_{0,n}$, and Δf_n led to good agreement between Eq. 3-7 and response of an M-ary (patch-based, varactor-loaded) RIS across a broad frequency range. Nevertheless, the need of fitting both the quality factor deviation and the resonant frequency shift hinders the direct optimization of the tuneable loads of the specific reconfigurable structure. Therefore, the need to devise an expression of the 'inverse' Lorentzian that includes the load impedance becomes clear. In order to do so, we start by deriving the reflection coefficient from temporal coupled mode theory (tCMT) as suggested in [KYE13]. We assume the situation depicted in Figure 3-8, where the (RIS) resonator has one dominant eigenmode with amplitude a that couples with two leads, i.e., one Floquet port (with waves s_1) and one circuital port (with waves s_2).

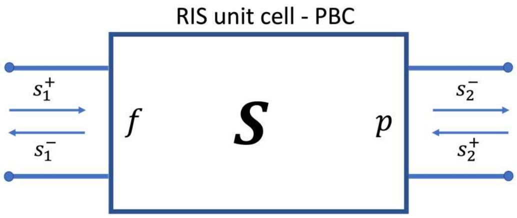

Figure 3-8 Waves scattered from a (single-mode) unloaded resonant RIS unit cell. The scattering matrix S is obtained from full-wave simulations under PBC.

The tCMT equations express the decay of the modal coefficient a into absorption losses and leads, viz.,

$$\frac{d\boldsymbol{a}}{d\boldsymbol{t}} = \boldsymbol{j}\boldsymbol{\omega}_0\boldsymbol{a} - \left(\frac{\mathbf{1}}{\boldsymbol{\tau}_0} + \frac{\mathbf{1}}{\boldsymbol{\tau}_1} + \frac{\mathbf{1}}{\boldsymbol{\tau}_2}\right)\boldsymbol{a} + \boldsymbol{k}_1\boldsymbol{s}_1^+ + \boldsymbol{k}_2\boldsymbol{s}_2^+$$

3-8

with τ_0 decay rate due to resonator losses, τ_1 decay rate due to the Floquet port, and τ_2 decay rate due to the circuital port, and the coupling of the resonant mode into port waves

$$\boldsymbol{s}_1^- = -\boldsymbol{s}_1^+ + \sqrt{\frac{2}{\tau_1}}\boldsymbol{a} \qquad \boldsymbol{s}_2^- = -\boldsymbol{s}_2^+ + \sqrt{\frac{2}{\tau_2}}\boldsymbol{a}$$

3-9

yield to the solution of the problem at hand. In the harmonic regime, the time-derivative in (3-8) becomes $\boldsymbol{j\omega a}$ and the modal coefficient is given in closed mathematical form as

$$a = \frac{k_1 s_1^+ + k_2 s_2^+}{j(\omega - \omega_0) + \left(\frac{1}{\tau_0} + \frac{1}{\tau_1} + \frac{1}{\tau_2}\right)}$$

3-10

with $k_1 = \sqrt{\frac{2}{\tau_1}}$ and $k_2 = \sqrt{\frac{2}{\tau_2}}$, which can be inserted into (3-9) to make the relation between scattered waves explicit. Furthermore, exploiting the relation between quality factor and decay rates $Q = \frac{\omega\tau}{2}$ yields closed form expressions for the scattering parameters of the two-port system

$$\boldsymbol{S_{11}} = \boldsymbol{\Gamma(f)} = \frac{\frac{1}{Q_1} - \frac{1}{Q_0} - \frac{1}{Q_2} - \frac{2j(f - f_0)}{f_0}}{\frac{1}{Q_1} + \frac{1}{Q_0} + \frac{1}{Q_2} + \frac{2j(f - f_0)}{f_0}} \quad \textbf{3-11}$$

$$\boldsymbol{S_{22}} = \frac{\frac{1}{Q_2} - \frac{1}{Q_0} - \frac{1}{Q_1} - \frac{2j(f - f_0)}{f_0}}{\frac{1}{Q_2} + \frac{1}{Q_0} + \frac{1}{Q_1} + \frac{2j(f - f_0)}{f_0}} \quad \textbf{3-12}$$

$$\boldsymbol{S_{12}} = \boldsymbol{S_{21}} = \frac{\frac{2}{\sqrt{Q_1 Q_2}}}{\frac{1}{Q_1} + \frac{1}{Q_0} + \frac{1}{Q_2} + \frac{2j(f - f_0)}{f_0}} \quad \textbf{3-13}$$

We proceed by considering the configuration in Figure 3-9, where the circuital port is terminated by the equivalent impedance of the tuneable electronic component.

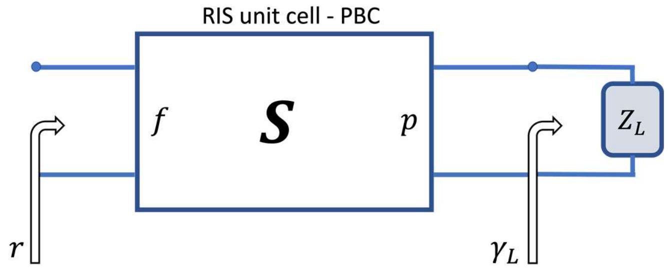

Figure 3-9 Global r and load γ_L reflection coefficients at the (single-mode) loaded resonant RIS-unit cell.

We then write the constitutive equations of the resonator in terms of scattering parameters

$$\begin{cases} s_1^- = \boldsymbol{S_{11}} s_1^+ + \boldsymbol{S_{12}} s_2^+ \\ s_2^- = \boldsymbol{S_{21}} s_1^+ + \boldsymbol{S_{22}} s_2^+ \end{cases} \quad \textbf{3-14}$$

known from Eqs 3-11- 3-13, and adopt the boundary condition

$$s_2^+ = \gamma_L \, s_2^- \quad 3\text{-}15$$

with circuital port reflection coefficient defined as

$$\gamma_L = \frac{Z_L - Z_{in}}{Z_L + Z_{in}} \quad 3\text{-}16$$

where Z_L is the equivalent impedance of the tuneable circuitry, and $\boldsymbol{Z_{in}}$ is the input impedance of the unit cell seen from the circuital port, as defined below in Eq. 4-21, and which can be devised from full-wave simulations. Now, Eq. 3-15 is applied to the second of Eq. 3-14 and used to eliminate s_2^+ in the second of Eq. 3-14, which yields the wave reflection coefficient of the (one-port) loaded resonator

$$r = \frac{\gamma_L^{-1} S_{11} - S_{11} S_{22} + S_{12} S_{21}}{\gamma_L^{-1} - S_{22}}$$

3-17

Upon substitution of Eqs. 3-11 - 3-13 in Eq. 3-17, and algebraic manipulations, we get to a generalized 'inverse' Lorentzian where additional terms due to the presence of circuitry have been identified, viz.,

$$\boldsymbol{r} = \frac{\left(\frac{1}{Q_1}-\frac{1}{Q_0}-\frac{1}{Q_2}-\frac{2j\left(f-f_0\right)}{f_0}\right)\left[\left(\gamma_L^{-1}-1\right)\frac{1}{Q_2}+\left(\gamma_L^{-1}+1\right)\left(\frac{1}{Q_0}+\frac{1}{Q_1}\right)+\left(\gamma_L^{-1}+1\right)\frac{2j\left(f-f_0\right)}{f_0}\right]+\frac{4}{Q_1 Q_2}}{\left(\frac{1}{Q_0}+\frac{1}{Q_1}+\frac{1}{Q_2}-\frac{2j\left(f-f_0\right)}{f_0}\right)\left[\left(\gamma_L^{-1}-1\right)\frac{1}{Q_2}+\left(\gamma_L^{-1}+1\right)\left(\frac{1}{Q_0}+\frac{1}{Q_1}\right)+\left(\gamma_L^{-1}+1\right)\frac{2j\left(f-f_0\right)}{f_0}\right]}$$

3-18

Where the quality factors and the central frequency are obtained by fitting the scattering parameters, obtained from the multi-port (wideband) full-wave simulations. The numerical verification of this new mathematical expression is performed for the RIS prototype §2.2.

In particular the simulation setup considered for the validation of the quality factors and Eq. 3-18, is presented in Figures 15a, b. PCB simulations with two ports (one Floquet and one discrete port) are performed in Figure 15a while in Figure 15b, PCB with one Floquet and impedance Z$_L$. More precisely, we have simulated the presence of a switchable component, e.g., diode, varactor, or mems, with the presence of an arbitrary complex-value impedance, here fixed at $Z_L = 50 + j75\ \Omega$, loading one of the lumped port.

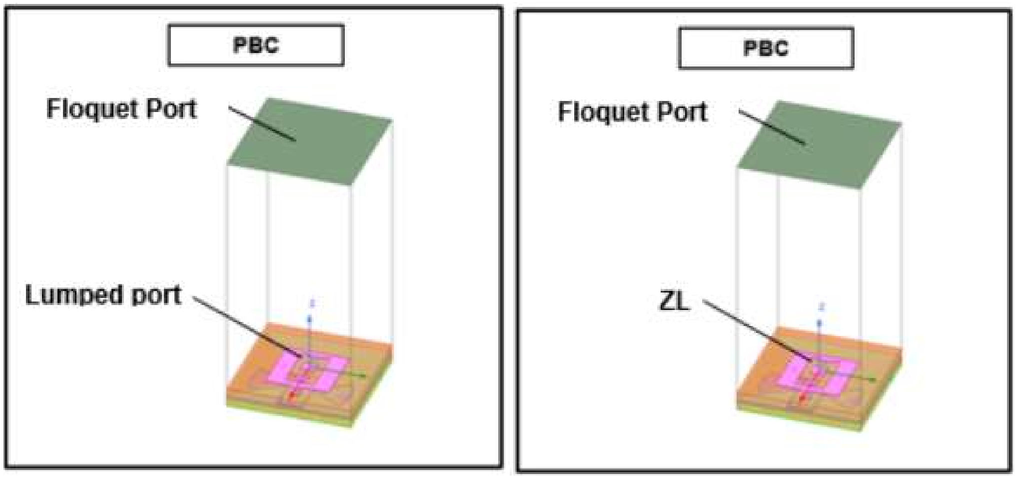

a) (b

Figure 3-13 Simulation layout of the reflective CEA-RIS prototype (b) Scenario 1: PBC simulation with two ports (one Floquet port and one lumped port). One of the diodes in the unit cell is deleted

(c) Scenario 2: PBC simulation with one Floquet port and impedance Z_L loaded replacing one of diodes, the second diode in the unit cell is deleted.

The quality factors Q_1, Q_2 are obtained from the 2x2 linear system formed by Eqs. 3-12 and 3-13 where the S parameters are obtained from the full wave simulation for the set-up of Figure 3-15a. The real and imaginary parts of Q_1, Q_2 are shown in Figure 3-16 and as expected the imaginary part is zero at 29 GHz. Eq. 3-18 is validated by comparing r, obtained from the simulation setup of Figure 3-15b, with the expression in the right-hand side, viz., $\frac{\gamma_L^{-1} S_{11} - S_{11} S_{22} + S_{12} S_{21}}{\gamma_L^{-1} - S_{22}}$. As seen in Figure 3-16b, Eq. 3-18 is validated with satisfactory accuracy.

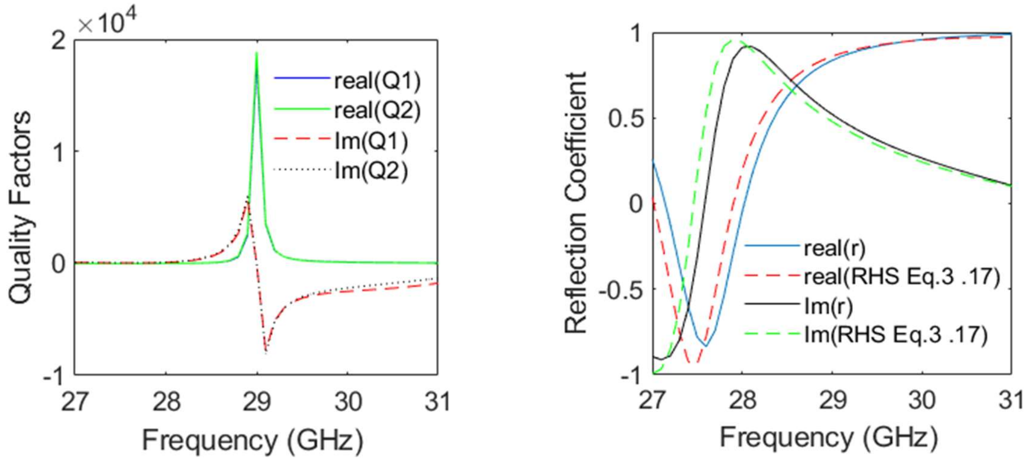

(a) **(b)**

Figure 3-14 (a) real and imaginary part of Q1 and Q2, obtained by solving the system of Eqs. 3-11 and 3-12. One of the diodes in the unit cell is deleted. (b) validation of Eq. 3-18 for $Z_L = 50 + j75\ \Omega$

A second simulation setup is adopted to validate the quality factors and Eq. 3-18 where is presented in Figure 3-18. In the left figure (a), one PBC simulations with two ports simulations is considered (the first one is the Floquet port and the second one is a discrete port placed in one of the diode and the second diode is used in the OFF state). In the right figure (b), a simulation setup is adopted where the lumped port is deleted and the diode in the state OFF is maintained

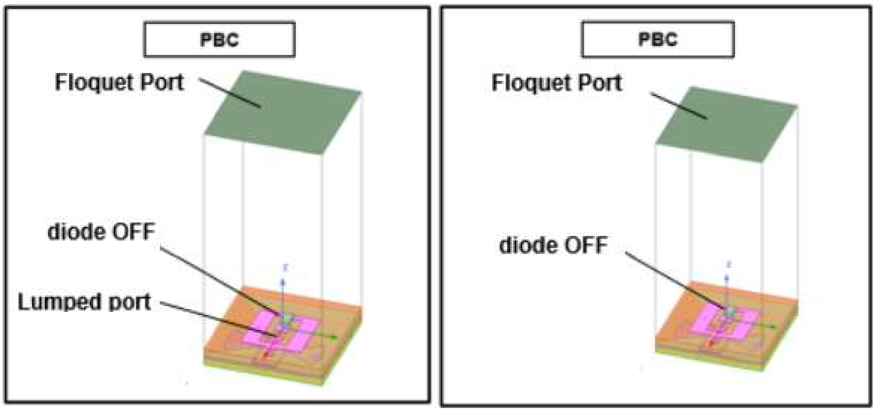

a) (b)

Figure 3-15 Simulation layout of the reflective CEA-RIS prototype (a) Scenario 1:PBC simulation with two ports one Floquet port and one lumped port and the second diode is placed in the off state (b) Scenario 2: PBC simulation with one Floquet port and the diode in the OFF state.

By following the same procedure as in the first case the quality factors are as expected, with zero imaginary part at 29GHz and Eq. 3-18 holds with accuracy higher than the first case. These findings are shown in Figure 3-18.

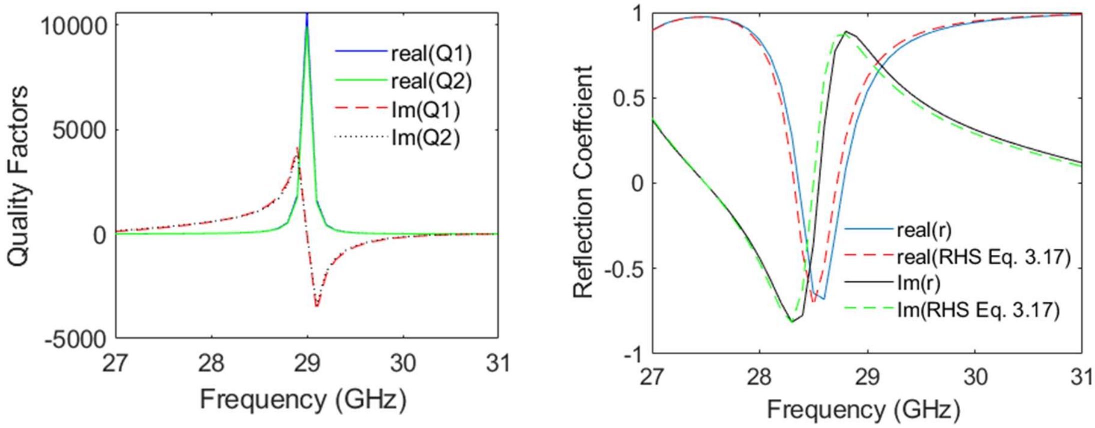

(a) **(b)**

Figure 3-16 (a) real and imaginary part of Q1 and Q2, obtained by solving the system of Eqs. 3-11 and 3-12. One of the diodes in the unit cell is in OFF state. (b) validation of Eq. 3-17 for $Y_L = \frac{1}{R} + j\omega C\ \Omega\ (\text{diode in off state})$

The treatment can be extended to multiple eigenmodes coupled (and decaying onto) multiple leads, and this constitute a future development to broaden the applicability range of the simple model assessed in this project.

3.3 Hybrid model based on transfer function validation

3.3.1 Reflectarray Configuration and Modeling

Previously a hybrid full wave methodology based on analytic expression and full-wave simulations was developed to synthetize, and optimize Transmitting-RIS (transmitarray). It was validated with the measurement results up to 330 GHz in. This tool has been extended to consider Reflecting-RIS and RA antenna arrays. In this section, the model will be presented briefly. The input data in the model are the following: the focal source radiation pattern, the unit-cells scattering matrix, and their radiation patterns. The data could be considered as ideal cases (ideal unit cell and ideal source) or could be extracted from full-wave simulations (such as HFSS simulation). The structure in § 2.2 is considered with a RIS of M×M elements. The RA is illuminated by a focal source at a focal distance F. The input power on the focal source is P_1 . The complex radiation pattern of the focal source is denoted as $H_{FS}(\theta,\phi)$. The radiation pattern in the m^{th} directions is $H_{FS}(\theta_{FS}^{m},\phi_{FS}^{m})$; the two components of the pattern in the m^{th} unit cell direction are $H_{FS}^{\theta^m}$ and $H_{FS}^{\phi^m}$. The complex radiation pattern of the unit cell is denoted as$H_{uc}\ (\theta,\phi)$. The radiation pattern in the direction of the focal source is $H_{uc}(\theta_{uc}^{m},\phi_{uc}^{m})$; the two components of the pattern of the m^{th} unit cell in the direction of the focal source are $H_{uc}^{\theta^m}$ and $H_{uc}^{\phi^m}$. Therefore, the incident wave received by the m^{th} unit cell is calculated by the following formula:

$$a_1^m = \frac{\lambda e^{-\frac{j2\pi R_m}{\lambda}}}{4\pi R_m}\left(H_{FS}^{\theta^m} H_{uc}^{\theta^m} + H_{FS}^{\phi^m} H_{uc}^{\phi^m}\right)\sqrt{P_1}\,,$$

3-19

where R_m: is the distance between the focal source and the m^{th} unit cell, and λ : is the wavelength.

The reflected wave by the m^{th} unit cell is then calculated using the following formula:

$$b_1^m = S_{11}^m . a_1^m,$$

3-20

where S_{11}^m: is the reflection coefficient of the m^{th} unit cell (for all $m = 1, \dots, M$).

Finally the radiation pattern of the reflectarray (H_{RA}^{θ} and H_{RA}^{ϕ}) is computed by the summation of the contribution of each cell, taking into account the reflected wave calculated in equation 3-19 and the radiation pattern of the unit cell for given direction $(\theta, \phi\ )$:

$$H_{RA}^{\theta/\phi}(\theta, \phi) = H_{uc}^{\theta/\phi}(\theta, \phi) \sum_{m=1}^{M} b_1^m e^{\frac{j2\pi}{\lambda}(sin\theta cos\phi X_m + sin\theta sin\phi Y_m)},$$

3-21

where X_m and Y_m: are the Cartesian coordinates of the unit cell (in the plane z = 0 , since the RA is placed in the place xoy.

The Matlab tool can ensure a full analytical study. Several sweeps could be performed such as: frequency sweep, focal distance sweep, etc… These sweeps help in the optimization of the RA antenna.

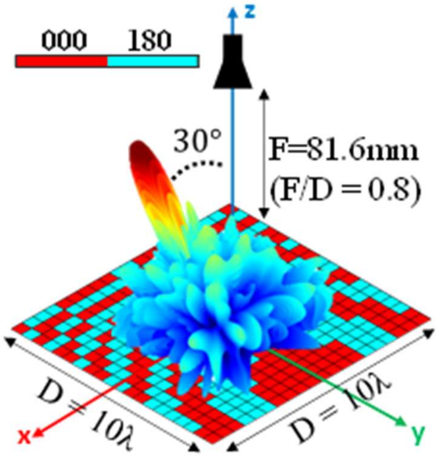

Figure 3-17 The adopted scenario in the Matlab Simulation of a RA of 20×20 unit cells and the 3D gain pattern in 30° direction.

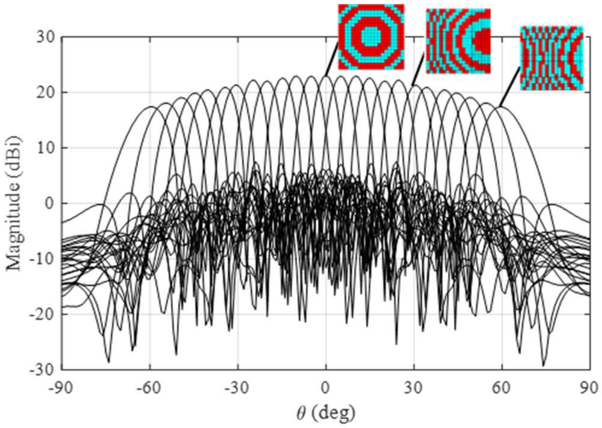

Figure 3-18 The gain patterns for different steering angles are calculated analytically in the Matlab tool for a RA of 20×20 unit cells.

InFigure 3-20, an example of 20×20 unit cells RA is shown. The analytical results calculated in the developed tool are shown in Figure 3-17 and Figure 3-18. The different phase distributions for the steering angles [-60°:5°:60°] are calculated as well as the 2D radiation patterns in the plane ϕ = 0° at 29GHz. The 3D radiation pattern for a reflection towards 30° is shown. There are other far-field results that could be extracted from the tool such as other cut planes, the gain vs the frequency, the efficiency etc…

3.3.2 Synthesis and Simulation of R-RIS

In order validate the model of the proposed MATLAB tool in one hand and to demonstrate the reliability of the designed reconfigurable unit cell in the other hand, a 8×8 unit cell (4λ×4λ, 40.8×40.8mm^2) RA is considered. The RA is illuminated using a standard 10-dBi horn placed at a focal distance F =32 mm (F/D = 0.8). For the sake of simplicity, the horn is placed at the middle of the RA. Since the horn is covering an angle of the reflection thus, the reflection in broadside is not considered in order to avoid the shadowing caused by the horn. The phase distributions for two steering angles are generated: i) Reflection towards 10°, ii) Reflection towards 30°. The full RA considering the two phase distributions is then simulated in HFSS (Figure 3-19) with the Finite Element Boundary Integral (FE-BI) solver.

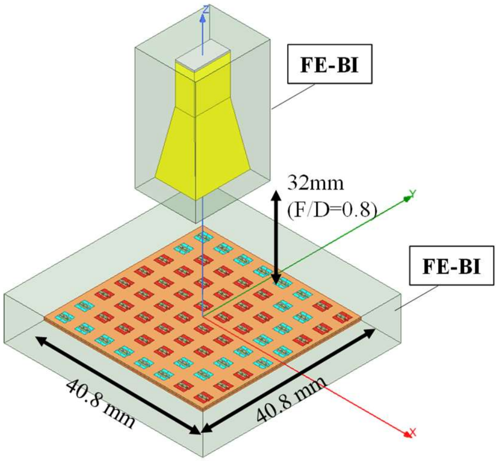

Figure 3-19 The HFSS simulation setup of a RA of 8x8 unit cells illuminated in the middle by a standard 10dBi horn

The simulation results are then compared to the MATLAB theoretical results. In Figure 3-20, the pattern for the two reflection cases (10° and 30°) are shown with the corresponding phase distribution. The plots show good agreement between the full-wave simulations and the theoretical results. For the case of the reflection towards 10°, the maximum gain calculated in MATLAB is of 15.71 dB, and of 14.92 dB the maximum gain exported from HFSS which leads to a small difference of 0.8dB. Whereas in the case of the reflection towards 30°, the gain value is almost the same with a small shift of 1.5° between the two patterns. The side lobes in both cases (10° and 30°) show differences between the analytical and simulation results. This could be explained by the small size of the considered RA. The simulation setup in HFSS (Figure 7) shows that the size of the horn compared to the size of the RA is too big and this may leads to some coupling effects. The aperture efficiency calculated at broadside reflection in MATLAB is of 20.91%. In general, the RIS sizes are much bigger than the one considered in this case. The small size was fixed in order to maintain the balance between the validation of the concept and the time consumption of the full-wave simulation. Finally, these patterns demonstrate the feasibility of reconfigurable RA using the developed unit cell.

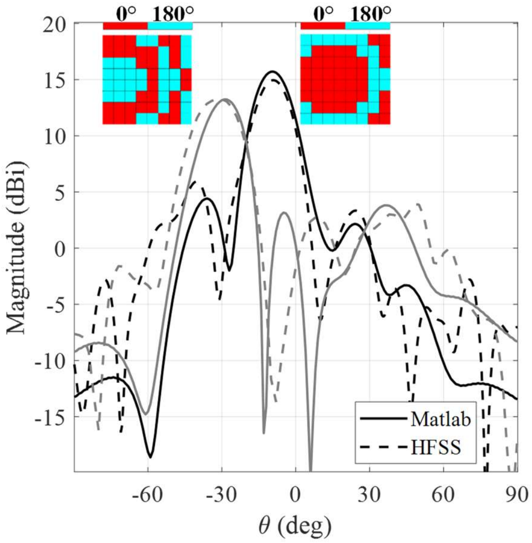

Figure 3-20 The 2D gain pattern of the RA of 8x8 unit cells at 29GHz in the plane ϕ=0° for two steering angles -30° and -10°.

3.4 FDTD modelling of RIS

In D3.3 we reported the model of the RIS modeled as a periodic arrangement of PEC squares patches over a ground plane [FCB21]. Varactor diodes that interconnect adjacent cells each other, are integrated within an in-house FDTD tool by their constitutive equations [TAF95]. The geometry of the simulated RIS is reported in Figure 3-21. We performed tests with a RIS composed by 100 patches and 180 varactor diodes. Its dimensions are 120x10x120 FDTD cubic cells, where the cell size is 1 mm. The dielectric substrate has been simulated with $\varepsilon_r = 4.4$ and $\sigma = 0.0025$ S/m whereas the ground plane is simulated as a PEC.

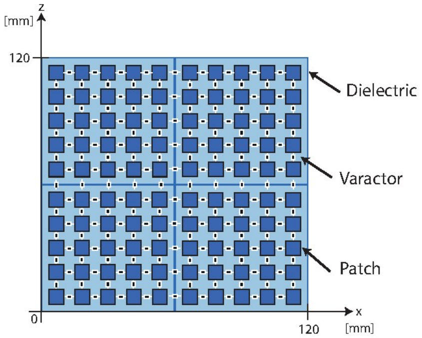

Figure 3-21 Geometry of the simulated RIS.

The EM source that hits the RIS is a plane wave, or randomly generated sets of plane waves. The generation of plane waves is done by an external serial program whose output is given as an input to the FDTD code. This avoids possible conflicts using parallel machine and can be applied due to the limited number of parameters. Concerning the capacitance values, we considered 1.0 pF and 0.1 pF which represent the two opposite cases, i.e., ‘ON’ and “OFF” state respectively. Figure 3-22 reports the field distributions for a 2D plane of the 3D simulated domain. The field distribution is evaluated in the near-field region over the RIS surface. In Figure

3-22 a) all capacities are set to 0.1 pF whereas in Figure 3-22 b) all are set to 1.0 pF. In the second configuration, the magnitude of the electric field distribution over the RIS is higher with respect to the case when all capacities are set to 0.1 pF. The possible configurations of a binary RIS with 180 varactors are 2^180, a number that is far too large to be tested via a brute force approach. Therefore, an optimization procedure can be applied in order to find the best RIS configuration that achieve energy focusing on a prescribed spatial location. Inherently, we implemented a routine based on GSL for scientific computation. The GSL library offers different kind of optimization algorithms that can be implemented in order to find the minimum or maximum of a given function. Among the ones available, the *multidimensional minimization* has been chosen. Our parameter space is spanned from the array of varactor diodes, each one characterized by a capacity. The goal of the algorithm is to iteratively find the ideal configuration of the varactor capacities to have the maximum towards the receiving antenna.

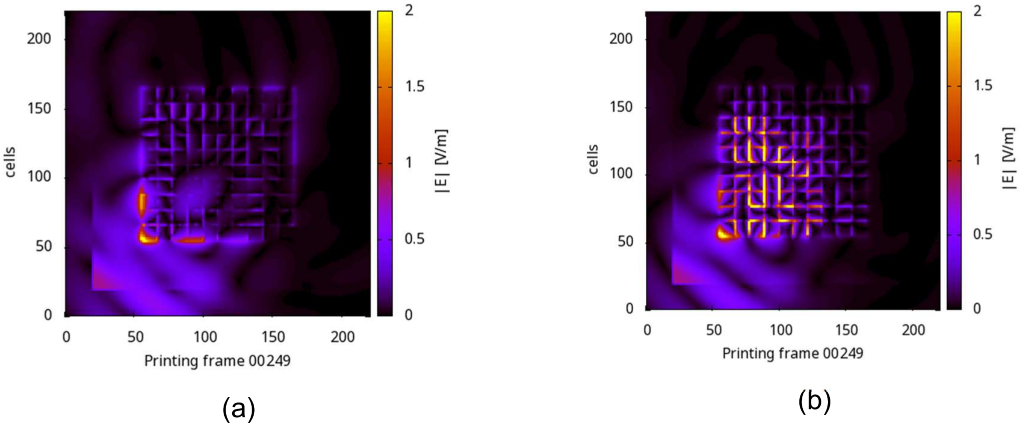

(a) (b)

Figure 3-22 2D field distribution over the RIS hit by a single plane wave.

In our simulations, the investigated frequency band ranges from 0.8 GHz to 8.4 GHz, whereas the optimization procedure is limited to a smaller band. In particular, the band for the optimization starts at 3.3 GHz and ends at 4.2 GHz. After several attempts we noticed that the finite band optimization is still computationally prohibitive. We thus introduced an additional constraint in the optimization routine that prescribes keeping the variance to a small level. We performed our analysis on two scenarios for the optimization:

- the minimization of the received field;
- the maximization of the received field.

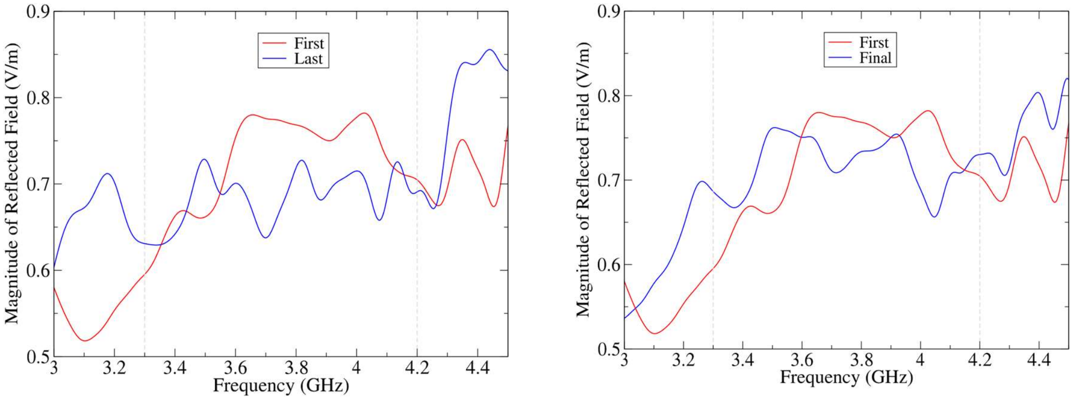

(a) (b)

Figure 3-23 Received field after: a) minimization and b) maximization. Single plane wave.

Figure 3-23 (a) and (b) reports the received field before and after the optimization respectively. The goal is either to minimize the received field (a), or to maximize it (b). In both cases, the band adopted in the optimization cycle starts from 3.3 GHz and goes up to 4.2 GHz. The minimization algorithm can reduce the signal throughout the investigated frequency band. In Figure 3-23 the source is only one plane wave with $\alpha = \theta = \psi = 45°$.

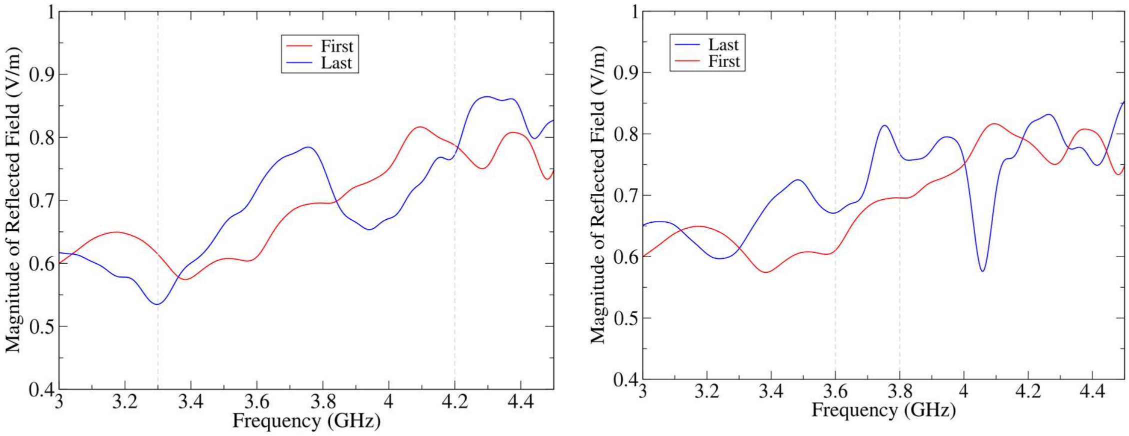

(a) (b)

Figure 3-24 Received field after: a) minimization and b) maximization. Set of plane waves.

Figure 3-24 shows the results before and after the optimization by considering a set of plane waves as source. After the optimization procedure, for the minimization there is a reduction of the received filed above 3.8 GHz but as showed in Figure 3-24 (a) in practice, there is a reduction of the variance. Regarding the maximization, after several runs and by reducing the frequency band, a maximum is found between 3.6 and 3.8 GHz, as reported in Figure 3-24. When we use a set of plane waves, the number of FDTD iterations increase of about 5 times those of a single plane wave, and the overall time of the simulation increases considerably. Those results are obtained by considering a cluster of diodes. This model for the RIS and the optimization algorithm are considered for WP6 activities. The use of random sets of plane waves is useful to simulate the statistics of RC fields [DAH98] by the Monte Carlo method. Briefly, the Monte Carlo technique is a method for simulating a random physical process using random numbers. The capability of this method of ensuring to create a stochastic field and thus emulating a physical process allows us to simulate the RC parameters such as Cartesian or rectangular components of the electric field, the received power, and the total electric field [LAD99, MBC02]. The numerical results of the Monte Carlo simulation borrow numerical uncertainty, which decrease as the number of performed simulations increase. Furthermore, the plane-wave integral model [DAH98] can be combined with the Monte Carlo statistical approach to simulate the EM behavior within a RC by a superposition of a finite set (or more sets if we run the parallel code on a supercomputer) of plane waves. In our simulations, the parameters that will be randomly generated are the propagation direction, the field polarization, and the phase of the plane waves, whereas a constant amplitude of 1 V/m is chosen for all plane waves. Within the working volume of a well stirred RC, there is not a preferred propagation direction and no preferred field polarization. This implies that the uniform distribution can be chosen for the generation of the propagation direction cosines, as well as for the polarization angles, over the solid angle and over 2π, respectively. Figure 3-25 shows the geometry of the random plane waves that hit an object at the center of the spherical frame of reference, in our case an RIS.

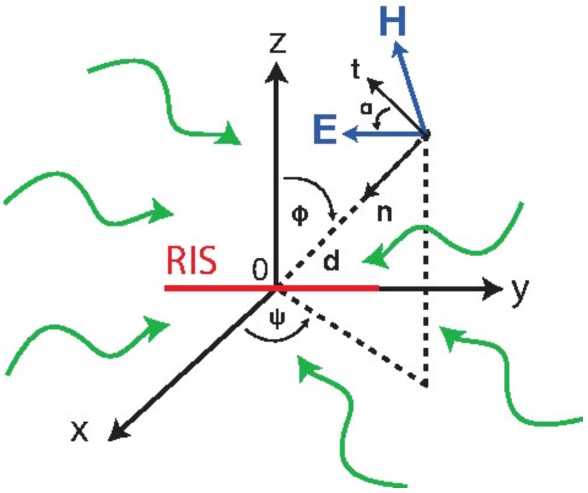

Figure 3-25 Geometry of plane waves that hit the RIS.

In our algorithm, in order to obtain a uniform distribution, we generate the θ and Φ angles by adopting the following procedure:

1) the angle θ is randomly generated with uniform probability in the range [0, π] and an auxiliary angle ψ is randomly generated with uniform probability in the range [0, 2π];
2) if 2π sin(θ) ≥ ψ, the angles θ and Φ = ψ/sin(θ) are stored in the computer memory and the plane wave will be used in the simulation;
3) otherwise, angles θ and Φ are rejected and the process starts again from the step 1.

Thereafter, the distance *d* will be generated, starting from outside the computational domain, and the polarization angle α is also generated with a uniform distribution within the range [0, 2π]. In the FDTD numerical analysis, adopting the plane waves method instead of simulating the entire geometry is preferable, and in some case is the only option, when the computational burden increase beyond the available computational resources, and/or we need more accuracy. In the FDTD, the best case occurred when devices and objects to be simulated can be modeled with the same cell size of the RC. In fact, a reduction of cell size increases drastically the simulation time. If we need to simulate complex objects or a finer grid is required, we can apply a superposition of plane waves to overcome this issue [MAP06]. The simulated RIS, composed by metallic patches, requires a high resolution that is not attainable by simulating a whole RC, e.g., the RC with dimensions 6x4x2.5 m^3 at 2 GHz can be simulated by a cell size of 1.5 cm which corresponds to λ/10, which is too large to model millimeter-sized objects such as the RIS structure.

4 RIS assisted Radio Environment Sounding and Modelling

4.1 Multiple RIS assisted channel sounding and characterization (CEA, GNW)

4.1.1 RIS designs and prototypes

1-bit Transmitting RIS

The employed linearly polarized TRIS operates in the Ka-band over a 3-dB relative gain bandwidth close to 25%. A 10 dBi pyramidal horn antenna illuminates a programmable electromagnetic surface composed of 20×20 radiating elements (also named unit cells). These unit cells (UC) are based on a 1-bit architecture to achieve low power consumption. To this purpose, two phase-states with a relative phase-shift of 180° are achieved by electronically changing the state of two PIN diodes integrated on the UC. The UC architecture is presented in Figure 4-1 (a) and consists of four metal layers (M1 – M4), two identical substrates of Rogers Duroid RT6002 and one bonding film of Arlon CuClad 6700. Figure 4-1 (b) shows the view of the TRIS with the focal source and the steering logic. The transmitting layer (M4) is composed of a rectangular patch loaded by a U-shaped slot, while the receiving layer (M1) contains a rectangular patch loaded by an O-shaped slot and the two PIN diodes (D1 and D2). In the EM simulator, these active devices are modelled as a lumped-element equivalent circuit extracted from the measurements and a gallium-arsenide block [DCD16]. This active patch is connected to the passive one printed on (M4) with a metallized via hole placed at the center of the UC. A ground plane occupies one of the two intermediate metal layers (M3). The other inner layer (M2) contains the biasing lines. In the proposed UC structure, one PIN diode is biased in the forward state with a 5 mA current. The 1.3 V threshold voltage of this diode is sufficient to maintain the other diode, mounted in anti-parallel configuration, in its reverse state. Thus, only one bias line is necessary for each UC, facilitating thereby the layout and routing of the bias network in very large array configurations. The bias line is 100 µm wide and is connected to the active patch by using two symmetric metallic via connections. More details on the 1-bit unit-cell operational principle, model, parametric analysis, and simulation setup are detailed in [DCD16]. The array can electronically steer the beam on a two dimensional window of $120° \times 120°$. The T-RIS patterns are shown in Figure 4-2. A peak gain of 23.1 dBi has been measured at 28 GHz when the beam is oriented in the broadside direction in very good agreement with the simulations. The average gain reduction due to the pin-diode insertion loss if compared to the performance of an equivalent fixed-beam transmitarray is lower than 1.7 dB.

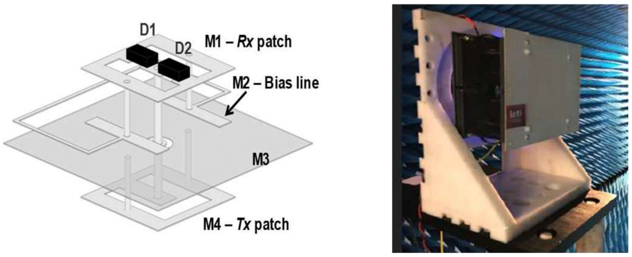

(a) (b)

Figure 4-1 (a) Schematic view of the 1-bit electronically reconfigurable unit cell based on PIN diodes, (b) view of the TRIS with the focal source and the steering logic.

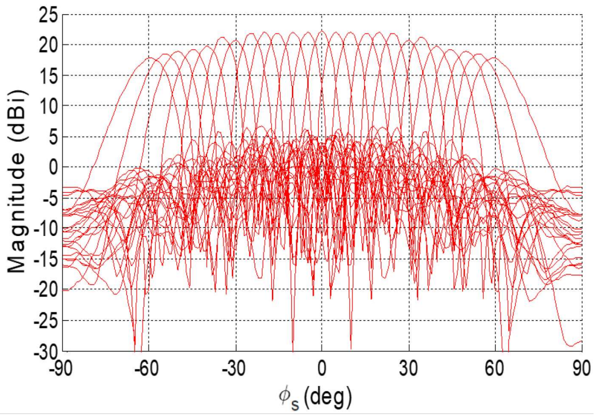

Figure 4-2 Linearly polarized TRIS beam scanning capability at 28 GHz (simulations).

1-bit Reflecting RIS

In this section, we describe Reflecting-RIS (RRIS) design working at mmW frequencies. The proposed RRIS is shown in Figure 4-3 (a). The unit cell has been designed to provide the patch resonance f_0 to be approximately around 27.5 GHz. The simplest way to achieve a 180° phase shift is to shunt the patch resonator onto the ground using an active element i.e. PIN diode. Nevertheless, this leads first to a strong dissipation growth due to increased current through the PIN diode. Here the design of the pixel, shown in Figure 4-3 (b) and (c), is complemented with a parasitic resonator P_H and P_V for both corresponding horizontal and vertical polarization of the E-vector of the incident wave. The resonance frequency of the parasitic resonator lies close to the resonance of the patch. That leads to the appearance of strong coupling between two resonators and corresponding anti-crossing behaviour when coupled resonances repulse and the mutual resonance shifting occurs. While changing the electrical length of the parasitic resonator we change its resonance frequency and can tune the mutual coupling between resonant modes of the parasitic resonator and the patch. This allows changing the resonance frequency of the patch and the phase of the reflected wave at a given frequency.

A 10×10 cm² RIS made up of 400 unit cells periodically placed every $\lambda/2 = 0.5$ cm on a rectangular lattice of 20×20 pixels. Each unit cell having to control independently both components of the reflected EM field. An overall of 400 diodes are used to control the vertical polarization and 400 diodes to control horizontal polarization. RIS consists of six layers PCB. The first layer is made from a low-loss substrate, namely the METEORWAVE 8000 from AGC of 0.5 mm thickness and $\varepsilon_r = 3$ dielectric permittivity, and supports the 400 unit cells. The five remaining layers are made from FR4 substrate. The last layer supports the electronic components to control the states of the diodes of the pixels on the first layer. This control is operated by a 10×10 matrix of shift registers, each managing the states of 8 PIN diodes associated to the horizontal and vertical polarization states of 4 pixels. In order to provide control of each pixel of the RIS, an FPGA control board has been designed and programmed. PIN diodes are thus connected to the control board through the network of shift registers. We have chosen to use a bistatic characterization approach. Figure 4-4 shows the amplitude and the phase of the measured $|S_{11}|$. As can be seen, the reflecting surface maintains an average dissipation of -2 dB in the 27-31 GHz band. In the desired mmW frequency range, the phase difference between ON and OFF states is between 150° and 180°. The physical model of the binary RRIS design, its fabrication and characterization are detailed The physical model of the binary RRIS design, its fabrication and characterization are detailed in [GPO21] [GPOL21] [POG21].

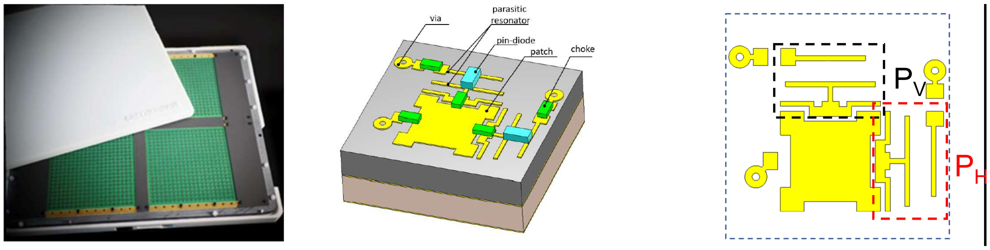

(a) (b) (c)

Figure 4-3 (a) RRIS composed by 4 panels of 20×20 pixels, (b) Perspective view, and (c): layout of the RRIS unit cell.

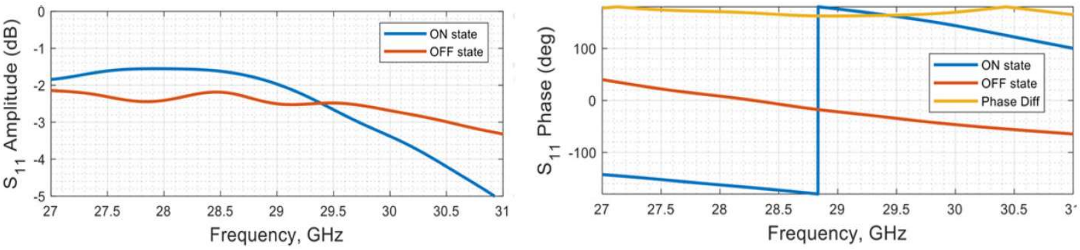

(a) (b)

Figure 4-4 RRIS Unit Cell characteristics: (a) reflection coefficient amplitude, (b) phase.

The simulated RRIS pattern for two sources configurations is presented in Figure 4-5 with steering angles between -60° and 60°. These two configurations match the scenarios measured during the measurement campaign with the Transmit-RIS acting as the source.

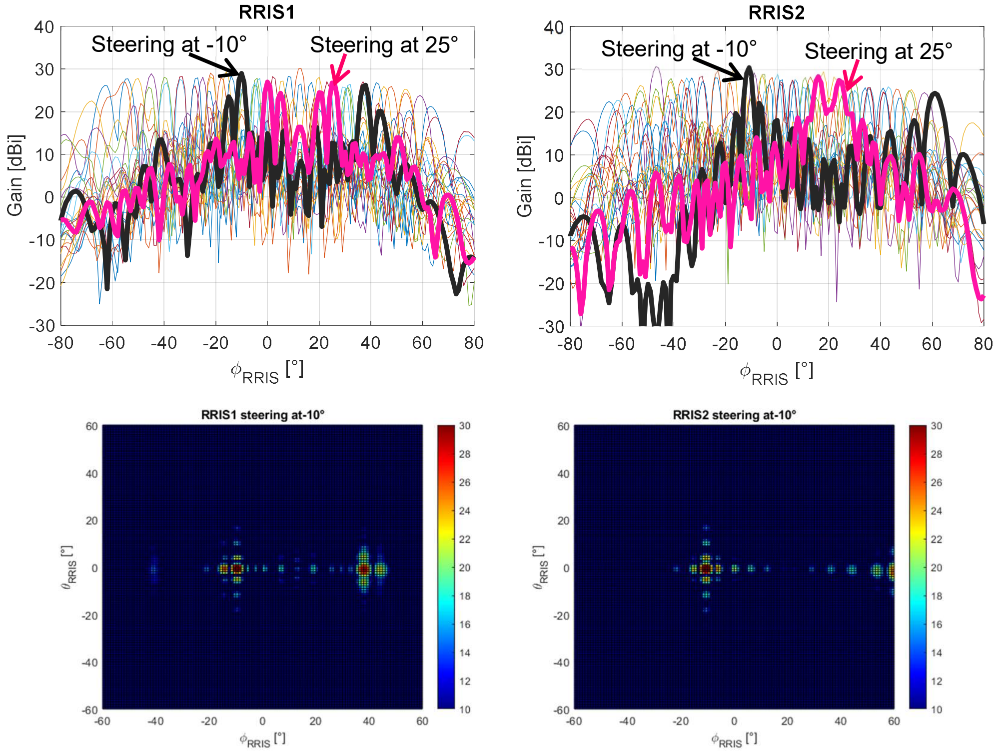

Figure 4-5 RRIS scanning beams at 28 GHz (top) and RRIS radiation patterns for a steering angle of 10° (bottom).

4.1.2 Measurement setup and environments

We have carried out in an indoor environment a channel measurement campaign employing two different types of RIS: a transmit-RIS (T-RIS) on the Base Station (BS) side and a reflect-RIS (RRIS) acting as extender. The User Equipment (UE) side involves a wideband monopole antenna with omnidirectional pattern in the azimuth plane. As illustrated in Figure 4-6, we have selected a single position for BS/TRIS, two different positions for RRIS (denoted as RRIS1 and RRIS2), and 5 different positions for UE (denoted as UE1, UE2, UE3, UE4 and UE5). All these antennas are almost at the same height, about 1.6 m above the ground. The propagation channel is measured based on a vector network analyser (VNA) operating in the 25-35 GHz frequency range. On a first step, we need to steer the TRIS beam towards the RRIS, and subsequently, we need to steer the RRIS beam towards the UE location. These steering steps require the estimation of the locations of the RRIS and UE, respectively, as well as the employment of an optimization algorithm on the RRIS. Alternatively and for more practical case representation, we have controlled both the TRIS and the RRIS to perform a scan of the steering angle in the azimuth plane (from -60° to +60° with a step of 5°). For each steering angle of TRIS, RRIS performs an azimuthal scan of the environment by updating accordingly and for a given location of Tx its phase distributions. Then, for each combination of TRIS/RRIS steering angles, the monopole antenna on the UE side is placed on an X-Y positioner and thus performs a 3x3 spatial grid of a half-wavelength step (4.3 mm). A computer is employed to control the measurement equipment (i.e., the VNA and the positioner) as well as perform automatically the azimuthal steering scan of both TRIS and RRIS after configuring the phase distributions of the latter. We have carried out these measurements for two cases: RRIS ON and RRIS OFF. The floorplan of the measurement environment with a visualization of the steering angles scan is shown in Figure 4-6, while the measurement environment and setup are shown in Figure 4-7.

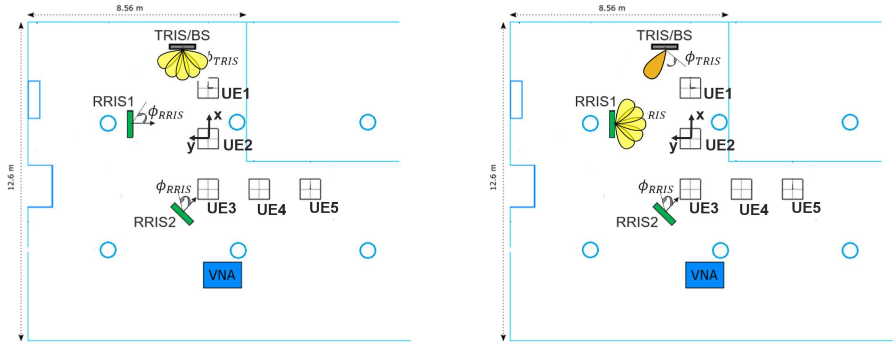

(a) (b)

Figure 4-6 Floorplan of the environment with the distribution of UE and RRIS. (a) TRIS scan, (b) RRIS1 scan.

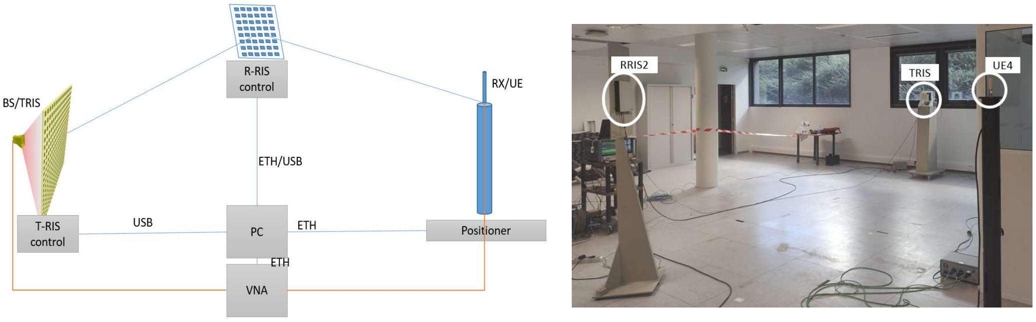

(a) (b)

Figure 4-7 (a) The measurement setup, (b) the measurement environment: case RRIS2 and UE4.

4.1.3 Results on channel characteristics

Using the virtual 3x3 array at the UE side, we are able to extract the multipath components (MPCs) in both angular and delay domains, by applying a wideband high resolution algorithm such as SAGE (space-alternating generalized expectation-maximization algorithm) [HTa03]. More clearly, each MPC is characterized by a distance and an angle of arrival (AoA). SAGE is effectively implemented within the 27-29 GHz band. It enables the extraction of 99% of the energy from the channel frequency response (CFR), while ensuring a constraint of 20 MPCs.

RRIS OFF

We start by showcasing the results obtained solely from TRIS's azimuth scan when RRIS is turned off. The direct TRIS-UE path is characterized by the travelled distance and its AoA with respect to the location of UE. Given the floorplan geometry and the AoA, we can compute the required steering angle of TRIS (ϕ_{TRIS}), which is particularly here equal to the AoA. On the other hand, we can use the SAGE results in order to get the measured values of both distance and the required steering angle. Table 4-1 displays the expected and measured values for the 5 UEs. Although the AoAs exhibit almost similar values, a difference of about 30 cm is shown for the distances owing to SAGE resolution.

Figure 4-8 shows the power of the direct TRIS-UE path and the overall channel gain as a function of the steering angle ϕ_{TRIS}. We note that the overall channel gain results from the sum of the powers of all the MPCs extracted by SAGE. The highest powers for each UE are observed at the expected steering angle and in its vicinity due to the limitations of the 5° scan step and beamwidth. Beyond this range, the power drops over 10 dB due to the TRIS sidelobes, except for UE5, which is obstructed by a wall. Regarding UE4, it is clear that the maximum power occurs at a steering angle between 25° and 30°, although the measured AoA is equal to 30°. The overall channel gain displays almost a similar pattern with the same maximum powers since the direct TRIS-UE path dominates the channel when TRIS is steering towards the UE. Otherwise, MPCs are added to the direct path, resulting in a higher overall channel gain.

Table 4-1 Direct TRIS-UE path characteristics: expected vs measured.

	Expected		Measured	
	Distance (m)	AoA (°)	Distance (m)	AoA (°)
UE1	1,89	32	2,25	29
UE2	3,74	15	4,05	14
UE3	5,69	10	6	9
UE4	6,35	28	6,6	30
UE5	7,51	42	7,8	41

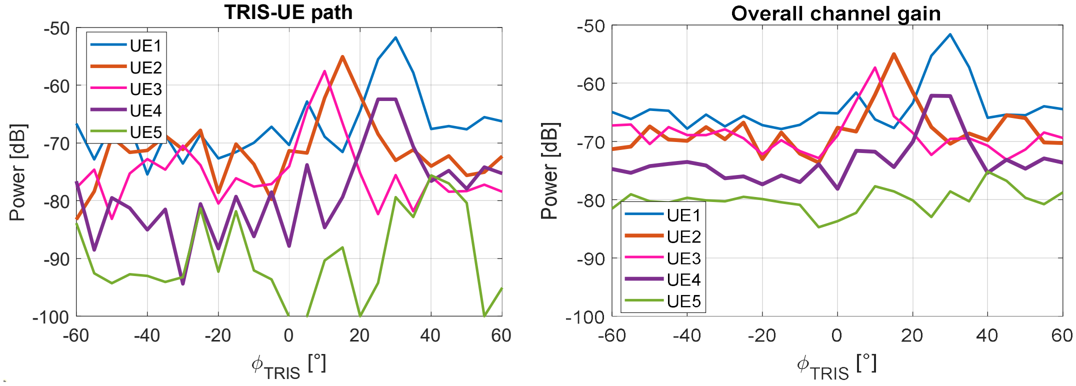

(a) (b)

Figure 4-8 TRIS's azimuth scan with RRIS OFF: (a) Power of direct TRIS-UE path, (b) Overall channel gain.

RRIS ON

With turning on the RRIS, we perform an azimuthal scan with both TRIS and RRIS. We aim to address the SAGE results when TRIS illuminates RRIS1 or RRIS2, which are subject to azimuthally scanning. To this end, we identify the appropriate steering angles for TRIS that align with the directions of RRIS1 and RRIS2, which correspond to -35° and 0°, respectively, as indicated by the floorplan shown in Figure 4-9. These angles are reliable since our prior analysis with RRIS turned off revealed a close match between the measured and estimated steering angles for TRIS. For each RRIS-UE pair, we isolate the corresponding RRIS path using the geometrical floorplan information (i.e., distance and AoA). We show then, for each UE, the variation of both the power of the isolated RRIS path and the overall channel gain as a function of the RRIS steering angle ϕ_{RRIS}.

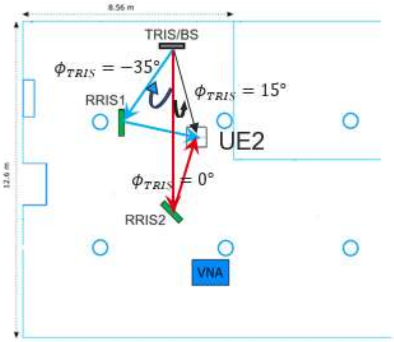

Figure 4-9 Floorplan and steering angles information for UE2.

UE2

Figure 4-10 shows, for UE2, the power of the isolated RRIS1 and RRIS2 paths, while TRIS is steering respectively towards RRIS1 ($\phi_{TRIS} = -35°$) and RRIS2 ($\phi_{TRIS} = 0°$). The results show that, while RRIS1 is scanning, UE2 experiences two maxima at -10° and +40°. The former corresponds to the expected main beam steering in the RRIS1-UE2 direction, while the latter corresponds to a sidelobe beam, which is due to the design of the 1 bit RIS. Regarding the scan with RRIS2, UE2 receives approximately the same gain over the angles ranging from 15° to 30°, while the required steering angle is expected at 25°. To validate these results, we plot the RRIS gain towards UE2 as a function of the steering angle ϕ_{RRIS}, as shown in Figure 4-11.

As shown in Figure 4-10(b) and for both RRISs, the overall channel gain is slightly increased when the RRIS is steering towards UE2. This is explained by the fact that the direct TRIS-UE path dominates the propagation channel. Indeed, when steering towards UE2, RRIS1 induces a relative gain of 1 dB, which is higher than that induced by RRIS2 since the former is much closer to UE2 than the latter.

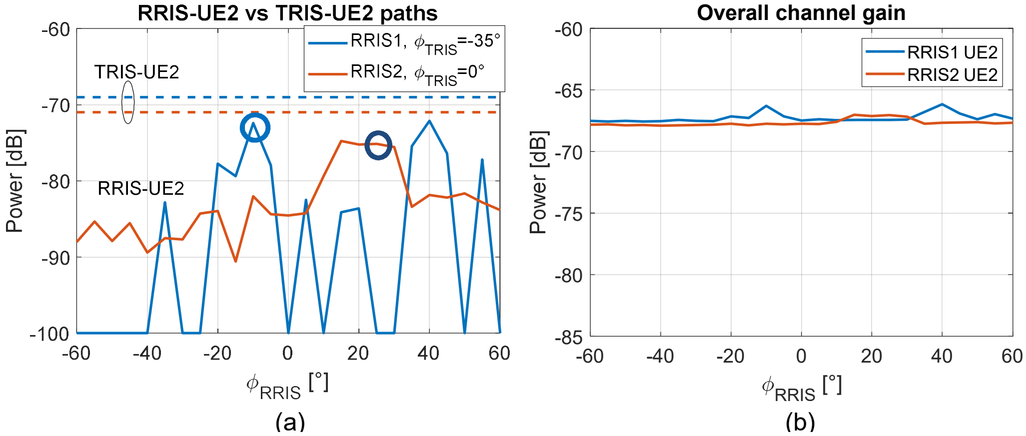

Figure 4-10 (a) Isolated RRIS path and (b) overall channel gain for UE2.

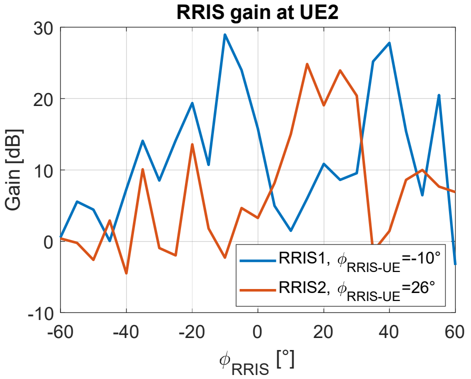

Figure 4-11 RRIS1 and RRIS2 gain towards UE2 as a function of the steering angle ϕ_{RRIS}.

Figure 4-12 shows the characteristics of the MPCs in angular-delay domain, after applying SAGE. Here delay is replaced by distance. The results are shown for RRIS OFF when TRIS is steering towards UE2 ($\phi_{TRIS} = 15°$), RRIS1 OFF ($\phi_{TRIS} = -35°$), and RRIS2 OFF ($\phi_{TRIS} = 0°$). Moreover, we shows the results for RRIS ON when TRIS is steering towards RRIS1 and RRIS2, which are in turn steering towards UE2 with respectively $\phi_{RRIS} = -10°$ and $\phi_{RRIS} = 25°$. The results clearly show that turning on the RRIS implies a new significant MPC related to the RRIS.

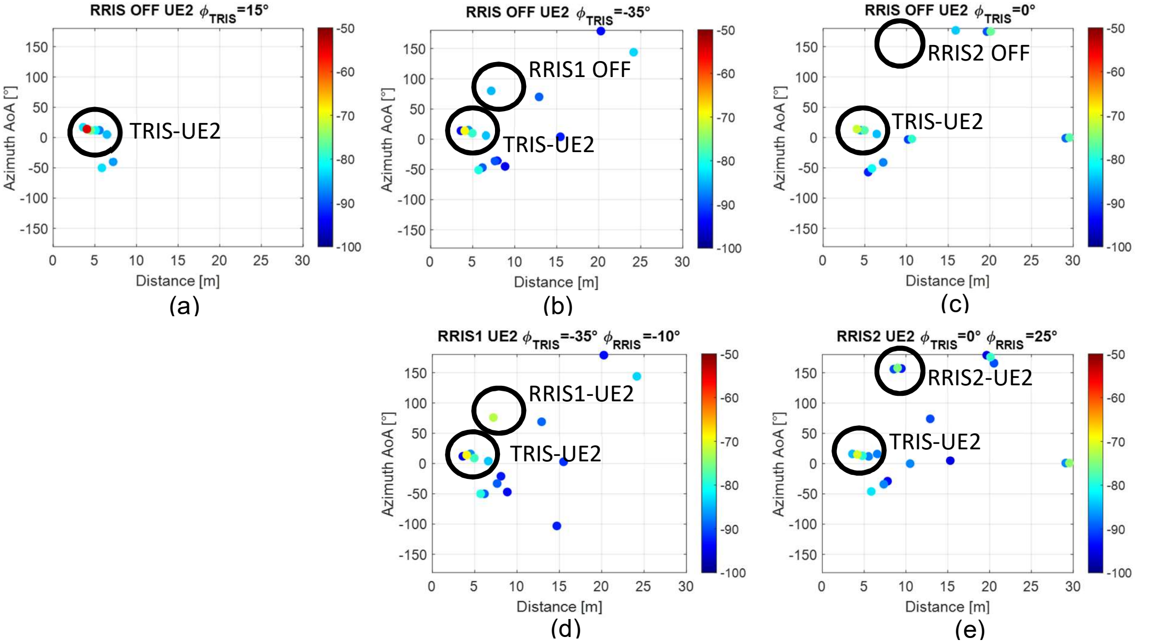

(a) (b) (c)

(d) (e)

Figure 4-12 Angular-distance distributions of MPCs at UE2, for RRIS OFF (top) and RRIS ON (bottom): (a) TRIS steering towards UE2 ($\phi_{TRIS} = 15°$), (b) TRIS steering towards RRIS1 ($\phi_{TRIS} = -35°$), (c) TRIS steering towards RRIS2 ($\phi_{TRIS} = 0°$), (d) $\phi_{TRIS} = -35°$ and RRIS1 steering towards UE2 ($\phi_{RRIS} = -10°$), (e) $\phi_{TRIS} = 0°$ and RRIS2 steering towards UE2 ($\phi_{RRIS} = 25°$).

UE4

Similar results are shown for the remaining UEs. In particular, we present in Figure 4-13 the isolated RRIS path power and the overall channel gain for UE4 since, contrary to UE2, the direct TRIS to UE4 path is not dominant when TRIS steers towards RRIS2. In this case, the impact of RRIS2 when steering towards UE4 ($\phi_{RRIS} = -35°$) on the overall channel gain is clearly shown in the results. A gain of more than 5 dB at $\phi_{RRIS} = -35°$ is shown on the overall channel gain. Another significant gain is shown at $\phi_{RRIS} = -55°$ due to the sidelobes of the RRIS, as shown in Figure 4-14. Regarding RRIS1, its impact on the overall channel gain is slightly shown since the direct TRIS-UE path dominates the channel and the RRIS1 is located far away from UE4. The angle-distance distributions of the MPCs resulting from SAGE algorithm are shown in Figure 4-15, where it is clearly shown the added MPC corresponding to turning ON the RRIS. The measured steering angles towards UE4 are with agreement with the geometrical expected values.

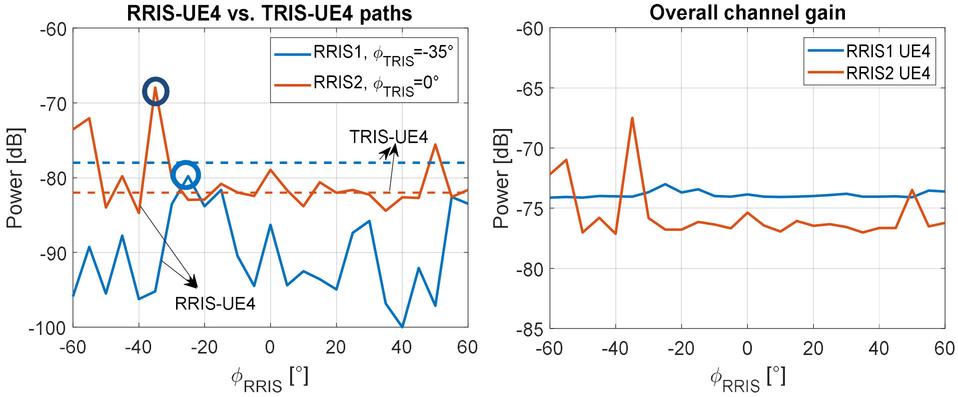

(a) (b)

Figure 4-13 (a) Isolated RRIS path and (b) overall channel gain for UE4.

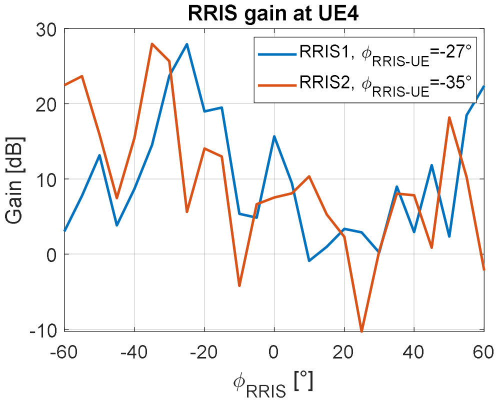

Figure 4-14 RRIS1 and RRIS2 gain towards UE4 as a function of the steering angle ϕ_{RRIS}.

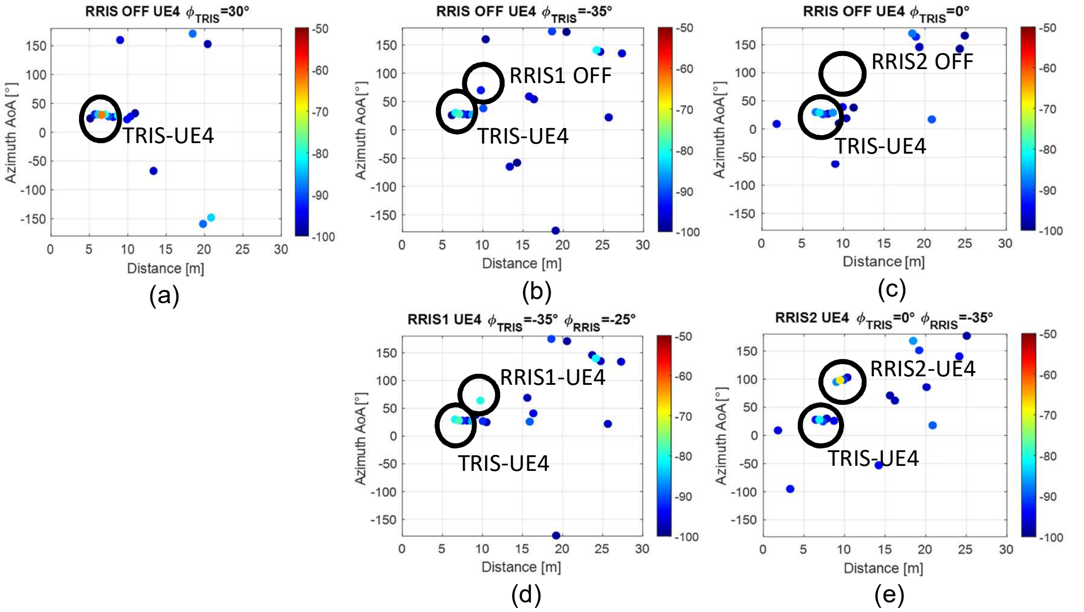

(a) (b) (c)

(d) (e)

Figure 4-15 Angular-distance distributions of MPCs at UE4, for RRIS OFF (top) and RRIS ON (bottom): (a) TRIS steering towards UE4 ($\phi_{TRIS} = 30°$), (b) TRIS steering towards RRIS1 ($\phi_{TRIS} = -35°$), (c) TRIS steering towards RRIS2 ($\phi_{TRIS} = 0°$), (d) $\phi_{TRIS} = -35°$ and RRIS1 steering towards UE4 ($\phi_{RRIS} = -25°$), (e) $\phi_{TRIS} = 0°$ and RRIS2 steering towards UE4 ($\phi_{RRIS} = -35°$).

4.1.4 Path loss estimation

We intend in this section to estimate the power received by each UE. We consider first the case RRIS OFF, where the power of the direct Tx-Rx path is estimated using the Free space Friis equation. Then, we consider the case RRIS ON, where the RRIS path is isolated due to SAGE algorithm. The received power due to the RRIS path is estimated using two different models, i.e., based on a radar-like equation and the field superposition over the unit cells.

RRIS OFF

According to the Free space Friis equation, the received power of the direct Tx-Rx path can be expressed as follows:

$$\frac{P_{Rx}}{P_{Tx}} = \frac{G_{Tx}(\phi^{Tx-Rx})G_{Rx}\lambda^2}{(4*\pi*d_{Tx-Rx})^2}, \qquad \textbf{4-1}$$

where d_{Tx-Rx} is the distance between TRIS and UE, $G_{Rx} = 1dBi$ is the UE antenna gain, and $G_{Tx}(\phi^{Tx-Rx})$ is the TRIS gain in the direction of a given UE (ϕ^{Tx-Rx}). Figure 4-16(a) illustrates the TRIS gain for each UE as a function of the steering angle, which ranges from -60° to +60° with a step of 10°. The TRIS-UE path free space received power for each UE is shown in Figure 4-16(b), with d_{Tx-Rx} are obtained from SAGE and ϕ^{Tx-Rx} correspond to the closest steering angle in the direction of each UE. Overall, the estimated received power for all UEs, except UE5, closely aligns with the measured values, with differences of only 3-7 dB in the direction of each UE. We note that the estimated received power is computed at a single frequency, while the SAGE computation is an average within a 2 GHz band. Notably, UE5 exhibits significant deviations due to its obstruction from TRIS.

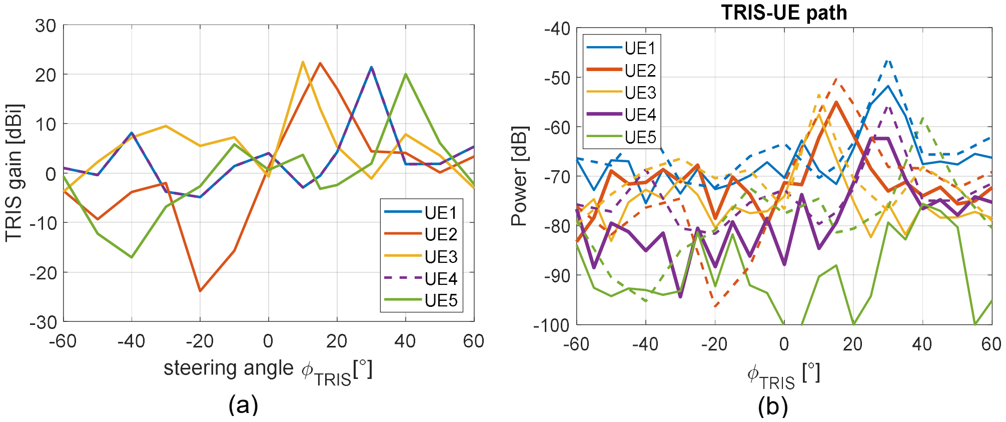

(a) (b)

Figure 4-16 (a) TRIS Gain towards each UE, (b) Free space estimated TRIS-UE path power (dashed lines) vs. isolated TRIS-UE path power (solid lines).

RRIS ON

After isolating the RRIS path with SAGE algorithm, we estimate the corresponding received power using two different models, i.e., the radar-like equation and the field superposition over the unit cells. We note that the formulas are given for a standard coordinate system where θ is the elevation angle and ϕ is the azimuth angle in the x-y plane corresponding to the RIS plane. However, we present our results by considering ϕ_{RRIS} as the angle in the x-z plane corresponding to the azimuth plane where the scanning of the environments occurs.

a) The radar-like equation

If we consider the RIS as an object illuminated by an incident plane wave, its radar cross section (RCS) could be expressed as:

$$\boldsymbol{RCS = S \times \eta \times G(\phi^{TX-RIS}, \theta^{TX-RIS}; \phi^{RIS-RX}, \theta^{RIS-RX})},$$

4-2

with S the RIS surface, η the efficiency, and G the RIS gain. We note that the RIS gain depends on the direction of the incident plane wave ($\phi^{TX\_RIS}, \theta^{TX-RI}$) and the direction of the desired reflected wave (ϕ^{RIS-R} , θ^{RIS-R}). Therefore, the RCS will vary with the phase distributions of the RIS.

The power received by an UE is computed as follows:

$$\boldsymbol{P_{Rx} = \frac{P_{Tx} G_{Tx} G_{Rx} \lambda^2}{(4\pi)^3 d_1^2 d_2^2} RCS},$$

4-3

with d_1 and d_2 the distances from the Tx and the UE towards the RIS, respectively.

b) The field superposition over the unit cells

The received electric-field strength due to a single UC (the *mn*th one with a reflection coefficient Γ_{mn}) is computed as:

$$E_{mn}^{Rx} = \sqrt{\frac{2Z_0 P_{Tx} \lambda^4 G_{Tx}(\phi_{mn}^{Tx}, \theta_{mn}^{Tx}) G_{Rx}(\phi_{mn}^{Rx}, \theta_{mn}^{Rx}) G_{RIS}(\phi_{mn}^{RIS-} \quad , \theta_{mn}^{RIS-Tx}) G_{RIS}(\phi_{mn}^{RIS-} \quad , \theta_{mn}^{RIS-} \quad)}{(4\pi)^4 d_{1,mn}^2 d_{2,mn}^2}} \times \Gamma_{\mathrm{mn}} e^{-j\frac{2\pi}{\lambda}(d_{1,mn}+d_{2,mn})}$$

4-4

By superposing the fields redirected by all the UCs and received at an UE, we can obtain the total E field strength as follows:

$$\boldsymbol{E_{Rx} = \sum_m \sum_n E_{mn}^{Rx}\, E_{Rx} = \sqrt{\frac{2Z_0 P_{Tx} \lambda^4}{(4\pi)^4}} \sum_m \sum_n \frac{\sqrt{G}\Gamma_{\mathrm{mn}}}{d_{1,mn} d_{2,mn}} e^{-j\frac{2\pi}{\lambda}(d_{1,mn}+d_{2,mn})}}$$

with $G = G_{Tx}(\phi_{mn}^{Tx}, \theta_{mn}^{Tx}) G_{Rx}(\phi_{mn}^{Rx}, \theta_{mn}^{Rx}) G_{RIS}(\phi_{mn}^{RIS} \quad , \theta_{mn}^{RIS-Tx}) G_{RIS}(\phi_{mn}^{RI} \quad , \theta_{mn}^{RI} \quad)$

4-5

We consider the beamforming in the far-field case, and we perform accordingly some assumptions. The distances from each *mn*th UC to Tx ($d_{1,mn}$) and RX ($d_{2,mn}$) can be approximated as:

$$d_{1,mn} = d_1 + \cos\left(\phi_{mn}^{RIS-Tx}\right)\sin\left(\theta_{mn}^{RIS-TX}\right)\left(m-\frac{1}{2}\right)d_x + \sin\left(\phi_{mn}^{RIS-Tx}\right)\sin\left(\theta_{mn}^{RIS-TX}\right)\left(n-\frac{1}{2}\right)d_y \quad \text{4-6}$$

$$d_{2,mn} = d_2 + \cos\left(\phi_{mn}^{RIS-Rx}\right)\sin\left(\theta_{mn}^{RIS-RX}\right)\left(m-\frac{1}{2}\right)d_x + \sin\left(\phi_{mn}^{RIS-Rx}\right)\sin\left(\theta_{mn}^{RIS-RX}\right)\left(n-\frac{1}{2}\right)d_y \quad \text{4-7}$$

Moreover, we assume that the directions from Tx (or Rx) towards all the UCs of the RIS are the same. Accordingly, we can calculate the received power at RX as:

$$P_{Rx} = \frac{E_{Rx}^2}{2Z_0} = \frac{P_{Tx}\lambda^4 G}{(4\pi)^4 d_1^2 d_2^2}\left|\sum_m \sum_n |\Gamma_{\text{mn}}| e^{j\phi_{mn}^{\Gamma}} e^{-j\frac{2\pi}{\lambda}(d_{1,mn}+d_{2,mn})}\right|^2 \quad \text{4-8}$$

The comparison of the two models with the isolated RRIS path is shown in Figure 4-17. The two models agree well with the RRIS path isolated with SAGE. Almost the same interferences are experienced by all the received powers across the scanning in the azimuth plane. The maximum powers are observed at the direction of the UE. We note that the RIS far-field distance at 28 GHz is equal to $\frac{2D^2}{\lambda} = 16$ m, which means that all the UEs are in the near-field of the RRIS. Even though, the results are in a good agreement. We will assess the received power by taking into account near-field conditions in future works.

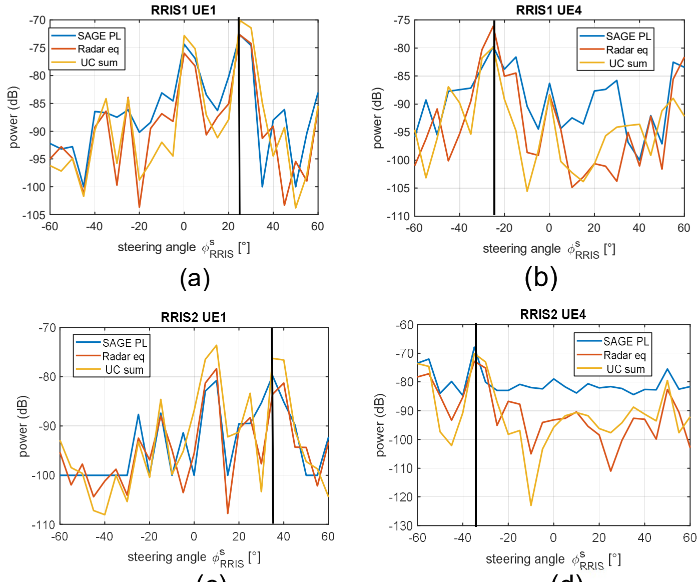

(a) (b)

(c) (d)

Figure 4-17 Comparison of the received power of the isolated RRIS path with the radar-like equation and the field superposition (UC sum). The vertical lines correspond to the UE position.

4.2 Measurement of sub-6GHz RIS impact on indoor channel characteristics

4.2.1 Setup Description

All measurements were carried out using the wide-band correlation channel sounding system described in [NFE18], configured to operate in a 100 MHz band centered at 3.5 GHz and sounding a 2 × 4 (Tx × Rx) branch multiple-input multiple-output (MIMO) channel. The two transmitter (Tx) channels Tx1 and Tx2 are sounded simultaneously and connected to the vertical and horizontal ports, respectively, of a dual-polarized antenna, see Figure 4-18.

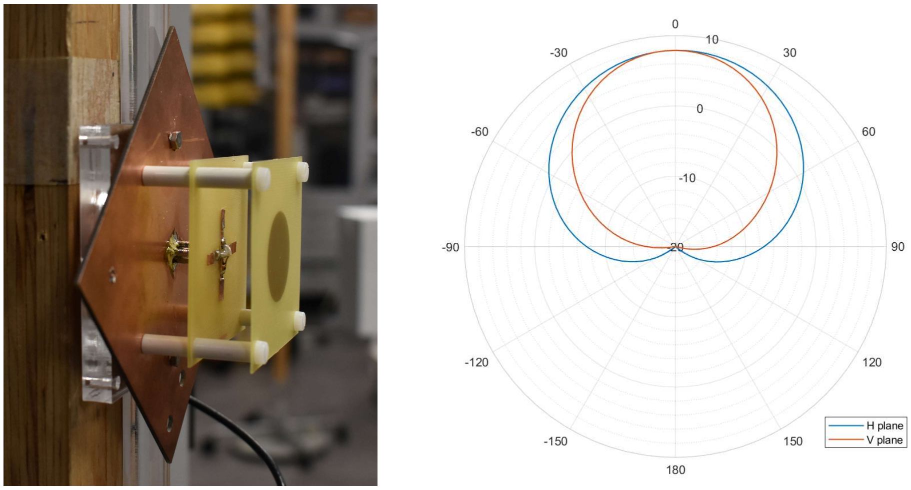

Figure 4-18 The dual-polarized patch antenna (left) and its gain pattern (right).

The 4 receiver (Rx) antennas were connected to a single frontend of the sounder via fast switch. Below a set of channel impulse response (CIR) measurements for all 2 × 4 branch combinations is denoted a channel snapshot, which was completed in 320 µs. The four Rx printed circuit board (PCB) antennas are identical with dipole-like characteristics and mounted to be vertically polarized and with a radiation pattern which is approximately omni-directional in azimuth.

The reconfigurable intelligent surface (RIS) used was the model I24-S35 from Beijing Actenna Technology Co, Ltd. which is specified to operate in the 3.4–3.6 GHz band with a 1–3 dB insertion loss. Its elements are arranged in a 10 × 10 planar grid and the phase of individual elements can be set in steps of 90° with an accuracy of ±15°, i.e., 2-bit control. It supports dual-linear polarization, with the same phase shift applied to both polarizations. It is noted that the polarization of the incident and reflected fields are orthogonal. The unit size is 430 × 430 × 46 mm^3 and was controlled from a computer via a serial link. An example of a beam pattern is given in Figure 4-19.

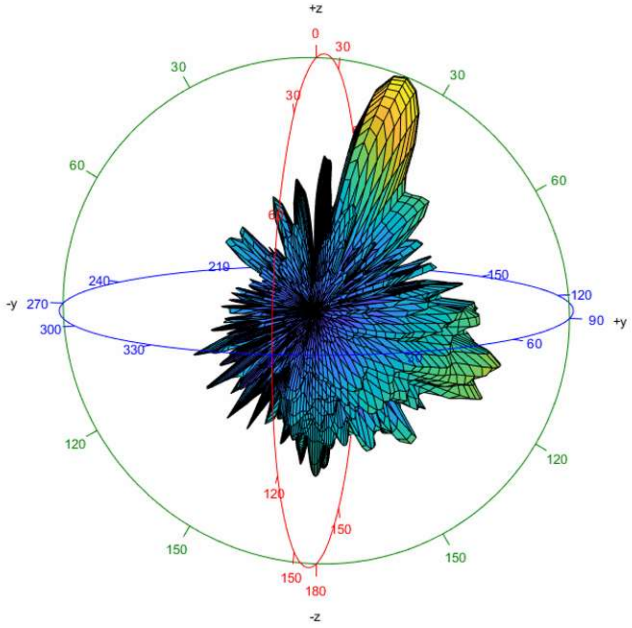

Figure 4-19 Power gain pattern for the RIS configured for AoD theta = 20°, phi = 90°, with AoA theta = 40°, phi = -90°.

All measurements took place in the laboratory area of Antennas, Propagation and Millimetre-Wave Systems (APMS) section at Aalborg University, as sketched in Figure 4-20. The Tx was located in a corridor to which the lab area is connected through openings, one of which is closed by a sliding door.

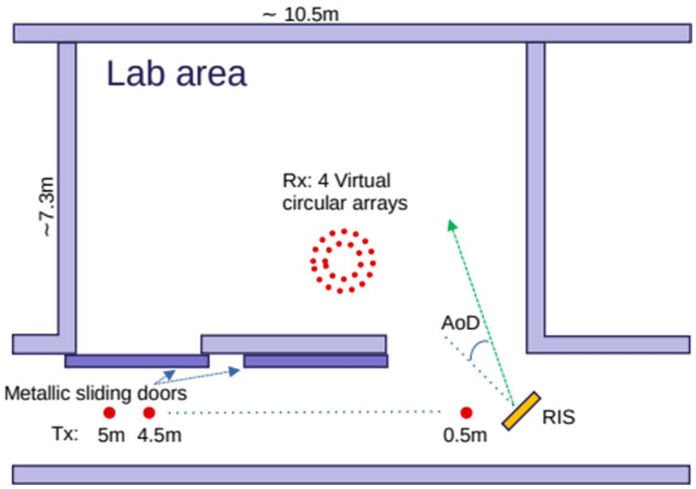

Figure 4-20 Sketch of the laboratory area where the measurements took place (not to scale).

The RIS was placed just outside the other opening, so that it could potentially scatter signal from the corridor into the lab area where the Rx antennas were. The lab is furnished with tables, shelves and closets filled with equipment and miscellaneous other items, see Figure 4-21.

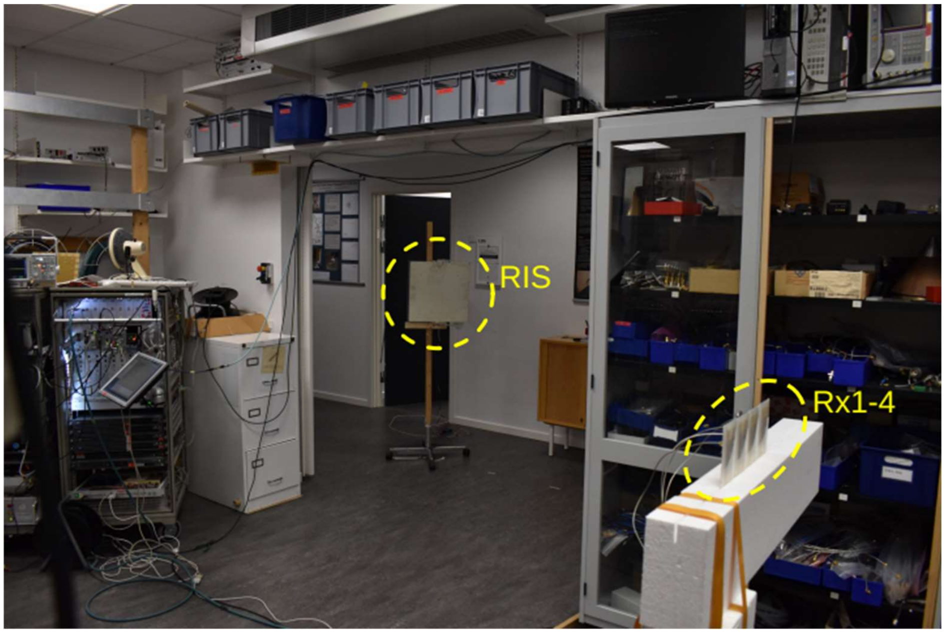

Figure 4-21 The laboratory area where the measurements took place.

A measurement consists of a series of 349 snapshots acquired while the Rx antennas were moved in concentric circles by a pedestal rotating a block of expanded polystyrene foam (EPS) on which the antennas were mounted, see Figure 4-21. In this way, each Rx antenna formed a virtual circular array (VCA) with radius of 10 cm, 18 cm, 26 cm, 37.5 cm, respectively, corresponding to about 1.1–4.4 wavelengths. The angle increment between snapshots was constant, i.e., about 1° and the time used for a measurement was about 39 s. Note that the measurements without the RIS was, for practical reasons, done with an angle increment of 3° in an otherwise essentially identical setup. In this setup the measurement time was about 232 s since more (6360) snapshots were obtained.

The Tx antenna, the Rx antennas and the RIS center were all mounted at a height of 1.25 m from the floor. Further, the RIS was mounted so that its normal was at an angle of 40° from the center line of the corridor, which made the normal point at the center of the VCAs.

Although the RIS can be used to form beams in a two-dimensional angle space, this work only uses main directions located in the horizontal plane at a height of 1.25 m, with the direction defined by the angle from the RIS normal, as shown in Figure 4-20. In all the measurements, the RIS angle of arrival (AoA) is −40°, which is the direction of the Tx antenna.

In the following d denotes the distance in meter between the RIS and the Tx, and d_f denotes the focal distance, i.e., the distance used when computing the phase values for the RIS configuration regarding the AoA. The similar focal distance used towards the Rx to control the angle of departure (AoD), was always set to 5 m. Two series of measurements were carried out, as described below.

Angle:

> For fixed $d = d_f = 0.5$, measurements were made for the AoDs −15°, −10°, 0°, 20°, 40°.

Dist:

> The AoD was set to 0°. Measurements were made for d □ $\{0.5, 1.0, \dots, 5.0\}$ with both $d_f = d$ and $d_f = 5$. In addition, for each distance a measurement was done without the

RIS. Further, for distances *d* = 1.5 and *d* = 5.0, the RIS was also configured with all elements set to zero phase, random values, and the RIS powered off (but present).

4.2.2 Data Analysis

For each combination of Tx branch and Rx branch, the measured CIR can be represented as $h'(s, n) = h(s, n) + w(s, n)$, where *s* and *n* denote the discrete snapshot and delay index, respectively, and where $h(s, n)$ is the CIR sample and $w(s, n)$ is the noise component. The delay samples are given by $\tau(n) = n\Delta\tau$ with $n \in \{0, 1, \ldots, N - 1\}$, $\Delta\tau = 2.5$ ns and $N = 960$. The snapshot index $s \in \{0, 1, \ldots, S - 1\}$ corresponds to the VCA element number with $S = 349$ or $S = 6360$ for the measurements with or without the RIS, respectively. Note that Tx and Rx branch indices are omitted in the following description for brevity, since the processing was done on all combinations independently.

When processing the data it is essential to consider the noise that inevitable will be present in the measured CIR data.

The rest of this section is adapted from [NP21] where a similar processing is described (for other measurements), with the purpose of ensuring the quality of the processed data.

Despite the use of automatic gain control (AGC) in the measurement system, a high signal to noise ratio (SNR) cannot be guaranteed in all the measurements, due to the highly dynamic channel. In this work the approach is to estimate the SNR for each CIR snapshot and only include snapshots that have an SNR above a threshold of 15 dB. Although very few snapshots in the current measurement campaign have too low SNR, the following procedure is followed to control the quality.

The instantaneous SNR for snapshot s is estimated by

$$\boldsymbol{\eta(s) = 10log\left[\frac{P_h(s)}{P_w(s)}\right]}$$

4-9

where the signal and noise power are estimated, respectively, as

$$\boldsymbol{P_h(s) = \sum |h(s,n)|^2 - M\sigma_w^2(s)}$$
$$\boldsymbol{P_w(s) = M\sigma_w^2(s)}$$

4-10

where the signal is assumed to be contained in the first $M = 135$ samples of the CIR, corresponding to 338 ns. This was verified by visual inspection of the data. The estimated instantaneous noise density is

$$\boldsymbol{\sigma_w^2(s) = \frac{1}{K}\sum \left|h(s,N-n)^2\right|}$$

4-11

i.e., it is estimated from the last $K = 460$ samples of each CIR. Visual inspection reveals that in this part of the CIR the squared magnitude of the samples may be modelled by fluctuations around a mean value, consistent with the assumption that, due to path loss, any signal components in this delay range are much lower than the system noise.

The SNR estimation described above is done for all combinations of Tx branch index, Rx branch index and snapshot. The subsequent processing only considers data with an SNR above the threshold of 15 dB.

Narrow band channels are considered in this work, and hence a discrete Fourier transform (DFT) is applied to the measured CIRs. The sub-channels are all normalized individually over the snapshots, as

$$\boldsymbol{H_n}(\boldsymbol{c},\boldsymbol{t},\boldsymbol{r},\boldsymbol{s})=\frac{\boldsymbol{H'}(\boldsymbol{c},\boldsymbol{t},\boldsymbol{r},\boldsymbol{s})}{\boldsymbol{H_{sys}}(\boldsymbol{c})} \tag{4-12}$$

in which $H'(c, t, r, s)$ is the channel transfer function before normalization, where c, t, r are, respectively, the sub-channel, transmitter, and receiver index. H_{sys} (c) denotes the known system transfer function. Only a subset of the sub-channels are included in the analysis, chosen to be within a 3 dB bandwidth of 70 MHz, corresponding to $C = 168$ sub-channels. The subsequent analysis is based on vectors of the channel coefficients obtained by concatenating the coefficients for all combinations of sub-channels, $R = 4$ Rx-indices, and snapshots. For a single measurement this leads to a maximum of $C \cdot R \cdot S = 168 \cdot 4 \cdot 349 = 234{,}528$ samples, when all the corresponding SNRs are above the threshold.

The vector of complex coefficients is used to compute an empirical cumulative distribution function (CDF) of the power gain, where the coefficients are normalized to the mean value for each measurement. To ease comparisons, both the mean value and the 1st percentile is used, i.e., the level, in dB, below which 1% of the power gain samples are observed. In the following ‘power’ is used as a shorthand for channel power gain.

It is noted that the sub-channels for a measurement may be correlated, depending on the channel properties, and hence the coefficients are not necessarily of the same value in the analysis. Note also, that the lowest power levels in the CDF are not limited by the SNR threshold, since the power in the sub-channels are subject to fading and the SNR is determined by the total power in the wide band channel.

4.2.3 Results and Discussion

Mean Gain

Figure 4-22 Mean normalized power versus the AoD, where the LOS is 0°.displays the mean power versus the AoD from the RIS. In all cases the gains are normalized to the mean gain value achieved for vertical Tx polarization at 1.5 m for the scenario without the RIS. Most of the measurements shown are from the Angle series of measurements, but for 0° AoD a measurement is also available from the Dist series, since the two series both include the distance 0.5 m. The results obtained are almost identical (within 0.2 dB) with a gain of approximately 12 dB and 13.7 dB achieved for vertical and horizontal polarization, respectively. For each angle the gain is 0.9-1.7 dB higher for horizontal than for vertical polarization, except at 30° where the vertical polarization is about 1.1 dB higher.

The gain is strongly dependent on the AoD, with a decrease of 7.6–8.4 dB at −10° compared to the gain at 0° and even more at larger angles. Since an AoD of 0° is in the direction of the VCA, this is the expected impact of the RIS.

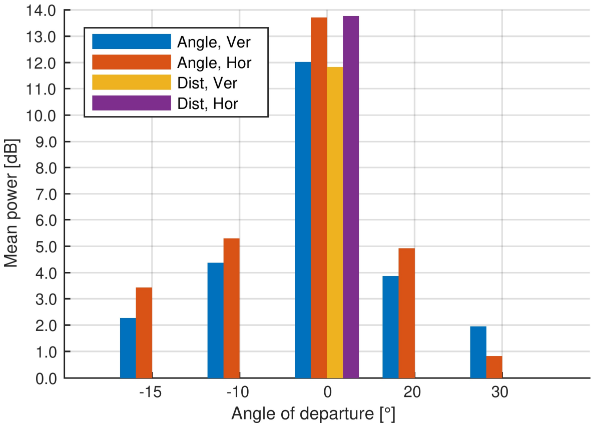

Figure 4-22 Mean normalized power versus the AoD, where the LOS is 0°.

The mean power versus distance is shown in Figure 4-23, obtained from processing the measurements in the Dist series. Again all power values are normalized to the mean value for the case without the RIS, at 1.5 m for vertical polarization. The different colors represent the configurations of the RIS.

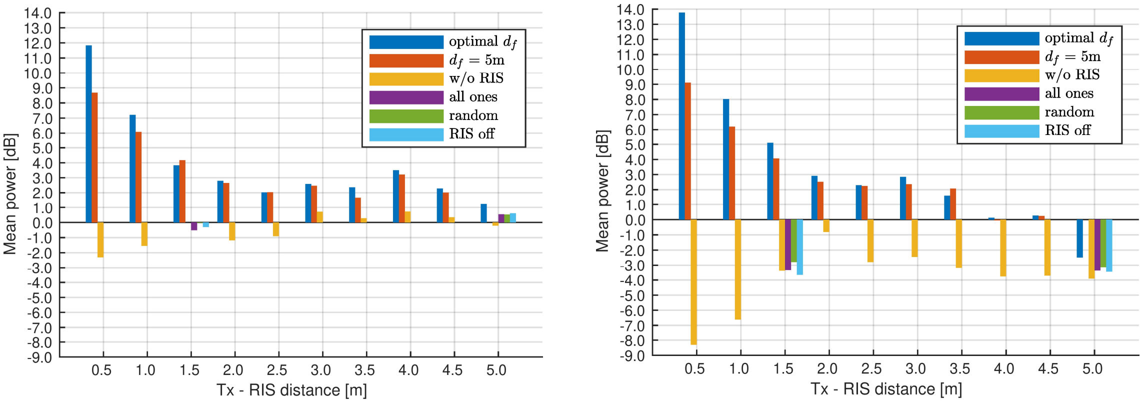

Figure 4-23 The normalized measured mean power versus distance between the Tx antenna and RIS for (left) vertical and (right) horizontal Tx polarization. The different bar/colors are for the different configurations of the RIS.

The power without the RIS is noticed to be vary some 3.0 dB (7.5 dB) along the corridor for the vertical (horizontal) Tx polarization. The relatively low variation with distance may be due to the setup, where the corridor may guide the signal before entering the lab area.

Without the RIS, the power for the horizontal Tx polarization is low, in the range about −8.3 to −0.8 dB, since the gain of the Rx antenna is included and the Rx antenna is mainly vertically polarized. Thus, in this case the Rx power is expectedly due to the cross-polarization coupling in the channel in addition to minor cross-polarization parts from the antennas.

The power achieved with the RIS is generally largest for close distances. This is expected since at short distances the RIS will reflect a large part of the power emitted by the Tx antenna, but at larger distances more of the power is reaching parts of the environment outside the RIS where it has no impact.

Defining the gain as the difference between the power achieved with and without the RIS for each distance, the gain is seen to depend highly on the distance. For 0.5-1.5 m the gain is 3.8–14.1 dB for the configuration with optimum focal distance, while the gain is 1.4–4.0 dB for 2–5 m distance, both for the vertical polarization. For horizontal polarization, the gain is about 8.5–22.1 dB for 0.5-1.5 m distance and 1.4–5.3 dB for 2–5 m, again for optimum focal distance. The generally higher gain for horizontal versus vertical Tx polarization is due to the Rx antenna being mainly vertically polarized and the wave reflected by the RIS is orthogonal to the incoming wave. Hence, in this setup the RIS effectively increases the cross-coupling in the channel.

The power achieved when assuming a focal distance of 5 m versus using the optimal distance, i.e., the actual distance, shows some differences, where the optimum focal distance gives −0.3 dB to 3.1 dB (1.0 dB to 4.7 dB) higher gain at 0.5–1.5 m, but only 0–0.7 dB (−0.5 dB to 0.5 dB) at longer distances for vertical (horizontal) polarization. The RIS element phase configuration is a function of the path length from the Tx to each element, but for sufficiently large Tx-RIS distance, the phase variation with distance is too small to cause practical differences, since the RIS can only be configured in 90° steps.

For the 1.5 m and 5 m distances measurements were also made with non-beamforming configurations of the RIS; viz. ‘random’, ‘all-ones’, and ‘RIS off’. For these cases the results are similar to these obtained without the RIS, within about 0.8 dB.

1st Power Percentile

Figure 4-24 shows the 1st percentile of the channel power gain versus the AoD for both polarizations obtained from the Angle measurement series. For comparison, the measurements from the Dist measurement series are shown for the 0° AoD. It is noticed that the results for the two series match within about 0.3 dB.

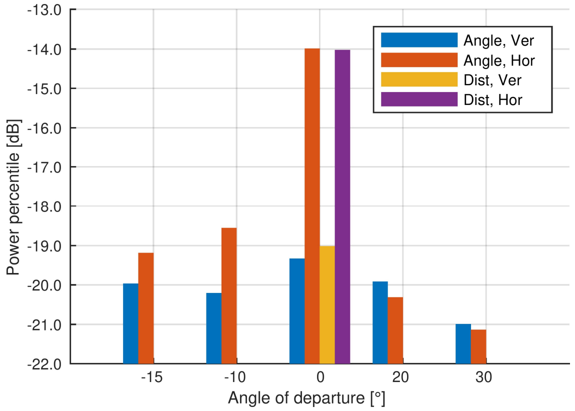

Figure 4-24 1st percentile of the measured instantaneous NB channel power gain versus the AoD, where the LOS direction between the RIS and the Rx is at 0°.

For 0° AoD in the horizontal polarization the percentile is about −14 dB compared to values mostly below −19 dB for other AoDs. This is consistent with the RIS creating a dominant direction in the horizontal polarization when the AoD is towards the VCA, whereas other AoDs make scattering from other directions more important.

Figure 4-25 displays how the 1st percentile depends on the distance for both Tx polarizations. For all distances and RIS configuration the percentiles for vertical polarization are relatively low in the range −21.5 dB to −19 dB with most values below −20 dB. Thus, the channels have statistics comparable to the −20 dB 1st percentile of a Rayleigh channel. Further, the variation due to the RIS configuration is within about 1.7 dB when the case of no RIS is included. It is noticed that even for d < 2 m where the mean power is higher than at longer distances (see Figure 4-23 (a)), the percentiles are −19 dB or below, indicating that the higher mean power is due to an increased power of more than just a few dominant paths. The picture is different in case of horizontal Tx polarization. For d ≤ 2 the percentiles are in the range −14 to −18.5 dB indicating that a dominating path exists from the RIS where the outgoing polarization matches that of the vertically polarized Rx ´antennas. For d > 2 the percentiles obtained with the RIS are in the range −21.0 to −19.0 dB and within about 2 dB of the similar measurements without the RIS.

Thus, although the mean power increases due to the RIS also for these distances, this is not only due to a increase power in a few paths.

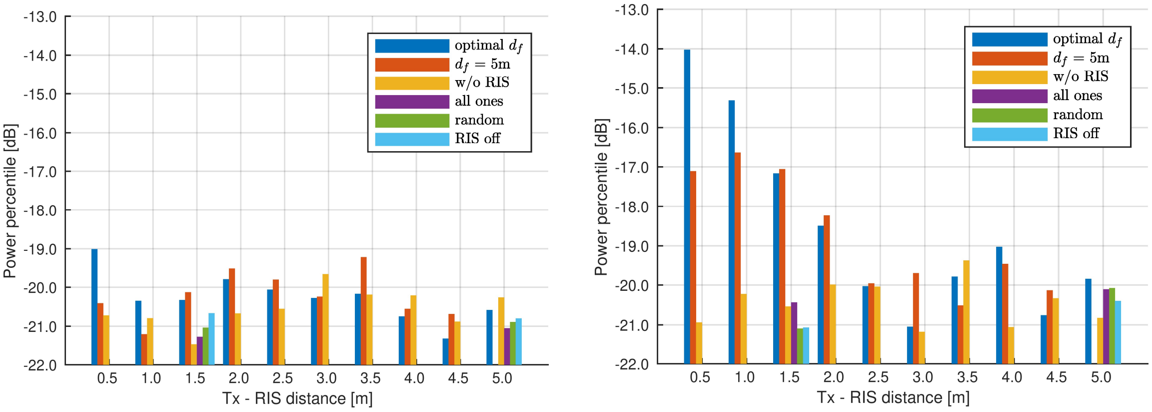

Figure 4-25 1st percentile of the measured instantaneous NB channel power gain versus distance d between the Tx antenna and RIS for (left) vertical and (right) horizontal Tx polarization. The different bar/colors are for the different configurations of the RIS.

4.3 RIS characterization and modeling in Reverberation chamber (CNIT, TIM, GNW, UNOT)

Figure 4-26 5G antenna.

The preliminary activity for the measurements campaign was the installation and configuration of the 5G base station (BS) within our lab, reported in D3.1. This activity was very important in understanding the functionality of a commercial 5G BS and for evaluating their KPIs in a real-life scenario. In fact, the 5G antenna, which operates at the mm-Wave frequency range, has the analog beamforming consisting of 32 beams. The used antenna is shown in Figure 4-26. We showed that the BS is able to scan the area and then selecting the beam that ensures the best link for the transmission. The BS is also able to change the beam in presence of an obstacle that blocks the link connection.

In our activities we employed the reverberation chamber (RC) in order to emulate both indoor and outdoor real-life scenarios. We exploit this RC peculiarity to test and explore the RIS functionalities in those reproduced environments. Preliminary activities that serve as input for other WPs, i.e. WP6 and WP7, are focused on the use of the vector network analyzer (VNA) to establish the better configuration of the RIS.
This task consists to considering the RIS at the origin of a reference system. We inserted the distance from the RIS to the transmitting antenna (Tx) as function of x, y, z coordinates and azimuth and elevation angle from the RIS to the receiver (Rx). In order to get the best RIS configuration, we employed of an optimization algorithm on the RIS by using an optimization algorithm provided by other partners.
In these tests, a computer is employed to control the measurement equipment i.e., the VNA, the RIS and the stirrer.

Figure 4-27(a) shows the RIS which is placed in front of the RC door whereas the Figure 4-27(b) shows the position of the Tx and Rx antenna. The Rx antenna is placed within an absorbing cage to reduce the multipath contribution and highlight the direct contribute due to the configured RIS.
The chamber is loaded by absorbing material to reduce the Q-factor of the RC and to block direct link between transmitting and received signal. Both Tx and Rx antennas will be replaced late by the 5G BS antenna and by the UE respectively. The use of the VNA is necessary to configure the RIS. Tests are repeated with both the door open, and the door closed behind the RIS.

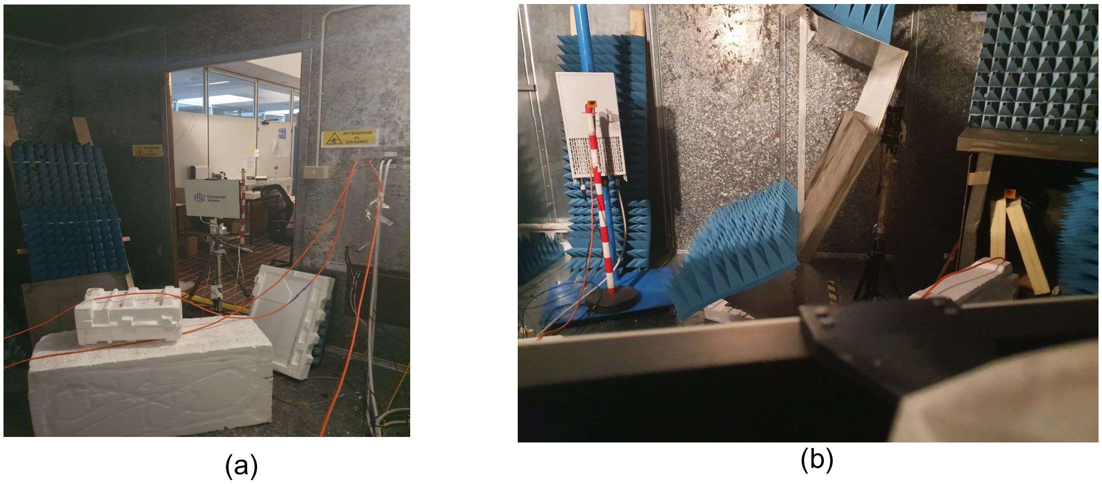
(a) (b)

Figure 4-27 (a) RIS within the RC placed in front of the RC door. (b) View of the RC equipped by two horn antennas, 5G BS antenna and absorbing material.

The receiving antenna is enclosed within a box, covered by absorbers excepted one side where the antenna points to the RIS. This homemade structure has been realized to reduce the multipath contribution on the receiver thus highlighting the contribution due to the RIS which is in line-of-sight (LOS) with the receiver.

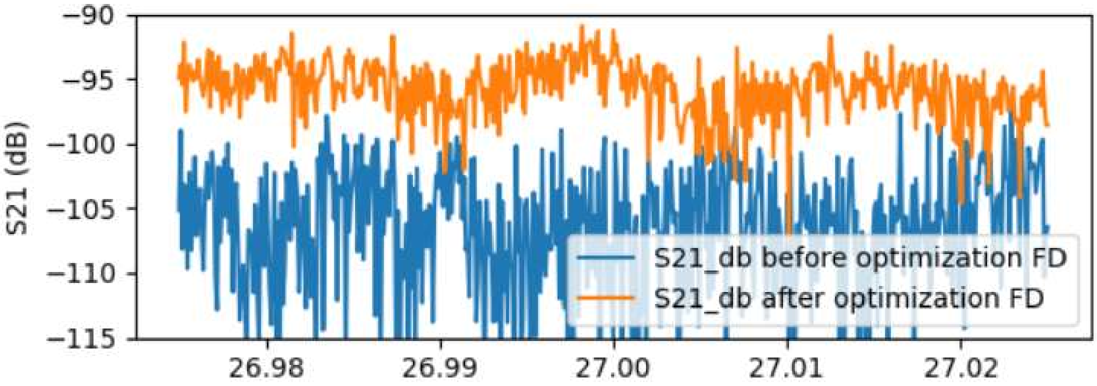

Figure 4-28 Comparison of S_{21} before and after the RIS optimized when the RC door is opened.

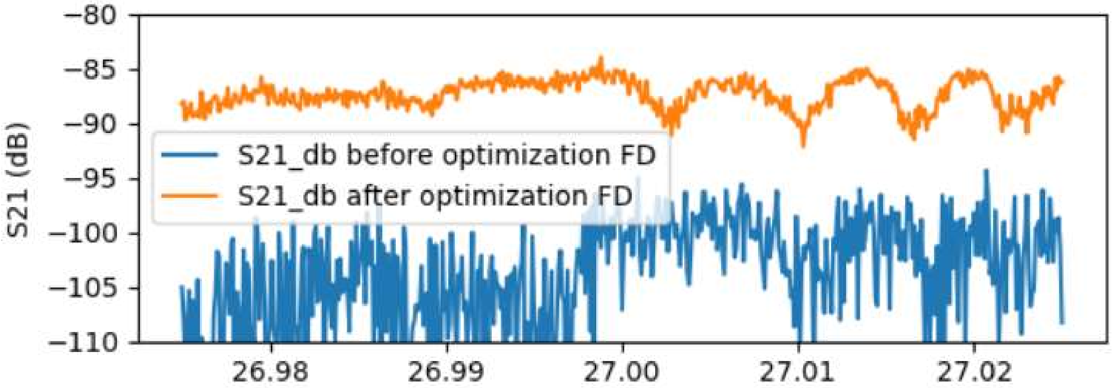

Figure 4-29 Comparison of S_{21} before and after the RIS optimized when the RC door is closed.

Figure 4-28 and Figure 4-29 reports the magnitude of the S_{21} when the RIS is randomly configured, labeled as "before_optimization" and after the optimization procedure, labeled as "after_optimization". When the door is closed the multipath contribute increases thus increasing the S_{21} and reducing the oscillations. In both scenarios, after the optimization the RIS is able to focus the signal on the R_x. Those activities, 5G BS configuration and the RC setup, are input for WP6 and WP7 measurements where we will also replace the horn antennas with the 5G antenna and the commercial UE.

Besides the case where we employed one receiving antenna, we are going also to investigate the performance of the RIS when a second, passive, antenna is added in the set up (Rx_2). Passive means that the optimization procedure is still focused on the antenna already present (R_{x1}). The more general set up of one of the investigated scenario is reported in Figure 4-30, which includes: the VNA, one transmitting horn antenna (Tx), one and two horn receiving antennas (R_{x1} and R_{x2}), absorbing materials and a notebook to collect data and configure the RIS.

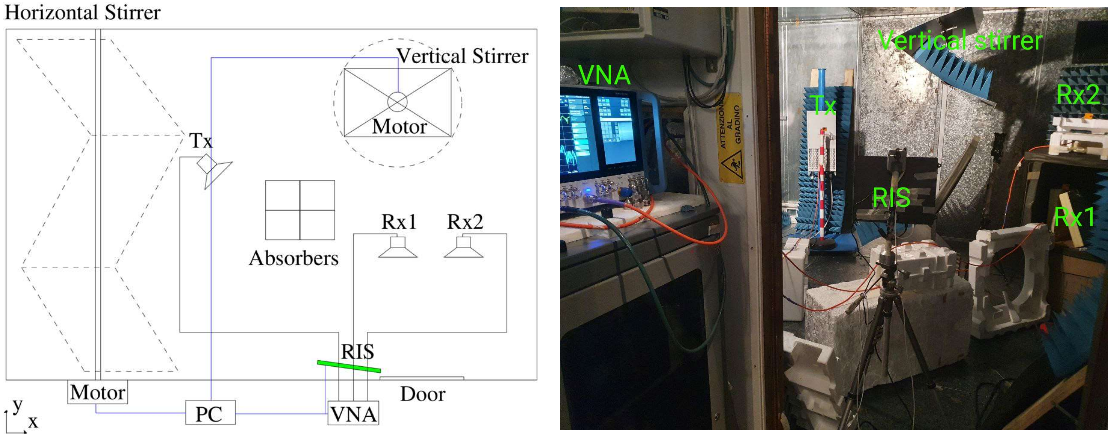

(a) (b)

Figure 4-30 Sketch of the setup with two receiving antennas.

The RC is still loaded by absorbing material. This setup is relevant for WP6 activities where more than one receiver e.g. user are investigated. For example the receiving target R_{x1} can represent the intended user whereas the R_{x2} can represents the non-intended user of a real scenario.

Figure 4-31 shows the final setup when horn antennas will be replaced by 5G antennas and UE to be used for WP7 activities. At this stage, the RIS will be configured by loading the configuration investigated previously with VNA and horn antennas.

The same setup, shown in Figure 4-31, will be adopted for the WP6 measurements by collecting data also from the second UE, to investigate the intended/non-intended user scenario.

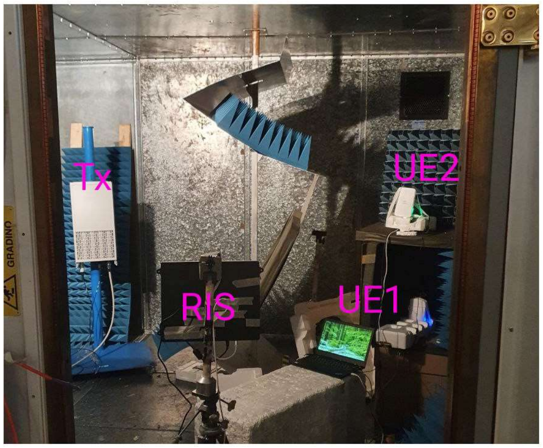

Figure 4-31 Final setup designed in WP3 for WP6 and WP7 activities.

4.4 DEA model for RIS-assisted environments

In the previous reporting periods, we have introduced a ray dynamical phase-space approach that propagates densities of rays efficiently through a numerical meshed space. Furthermore, we have introduced the generalised Snell law as a classical route to integrate anomalous reflectors at the boundary of an 2D confined environment. However, while this methodology is computationally efficient, as it enables rapid prediction (and programming) of wireless coverage within large floor maps of indoor channels, becomes inadequate to model arbitrary RIS structures in reflective environments self-consistently. The root of the problem resides in the non-symplectic behaviour of the generalized Snell law, which violates power conservation [AAT16] by ignoring spurious re-radiated waves [VVD+22]. Furthermore, having a global reflection law does not give access to the local state of individual RIS unit-cells.

In this reporting period we have solved the problem of power conservation by transforming a discrete EM model of the RIS scattered field into a phase-space representation through the WDF. Here, we just recall the definition of the WDF for a scalar field $\Psi(x)$,

$$\boldsymbol{W}(\boldsymbol{x},\boldsymbol{p}) = \int \boldsymbol{\Psi}\left(\boldsymbol{x}+\frac{\boldsymbol{u}}{2}\right)\boldsymbol{\Psi}^*\left(\boldsymbol{x}-\frac{\boldsymbol{u}}{2}\right)\boldsymbol{exp}(-\boldsymbol{ikpu})\,\boldsymbol{du}$$

4-13

where the variable x describes the position and p the local momentum. It is worth reminding two important properties of the WDF: It is positive and real-valued. Following the steps outlined in [MCT+22,TRM+22,TRM+23] for a RIS with N identical unit cells, the physical optics approximation leads to

$$\boldsymbol{W(x,p)} = \frac{1}{2}\left(\frac{kd}{2\pi r}\right)^2 \sum_{n=1}^{N}\sum_{l=1}^{4} r_n\, r^*_{l+m-n-2}\ e^{-jkd(2n-l-m+2)p}$$
$$(2-|l-2-\epsilon|)\,\mathrm{sinc}\left((2-|l-2-\epsilon|)\frac{kd}{2}(p-\sin\theta)\right) \tag{4-14}$$

with (uniform) unit-cell dimension d, $m = \lfloor 2x/d \rfloor$, $\epsilon = 2x/d - m$, and r_n local reflection coefficient of the n-th RIS unit cell. A Gaussian smoothing is applied in phase space to average out negative values of the WDF, which gives the HDF $H(\boldsymbol{x},\boldsymbol{p})$. Referring to [MCT+22,TRM+22,TRM+23], the reflection coefficients of a binary RIS $r_n = \{-1,1\}$ are optimized via simulated annealing to obtain the reflection of a single TE/TM plane wave towards non-specular directions. Figure 4-32 and Figure 4-33 report two examples of anomalous reflection in phase-space with the related phase masks of a one-dimensional RIS.

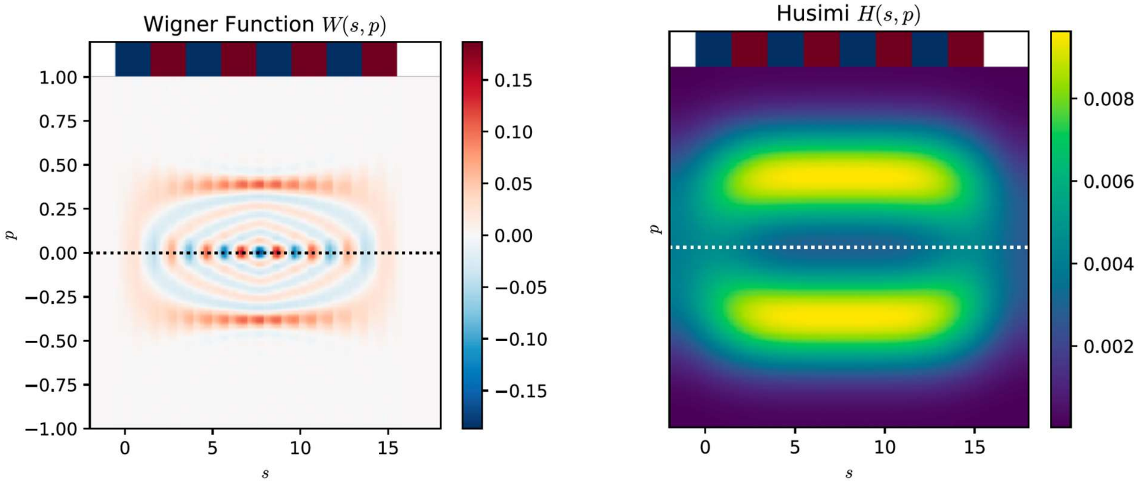

Figure 4-32 Phase-space anomalous reflection of a periodic RIS upon normal incidence.

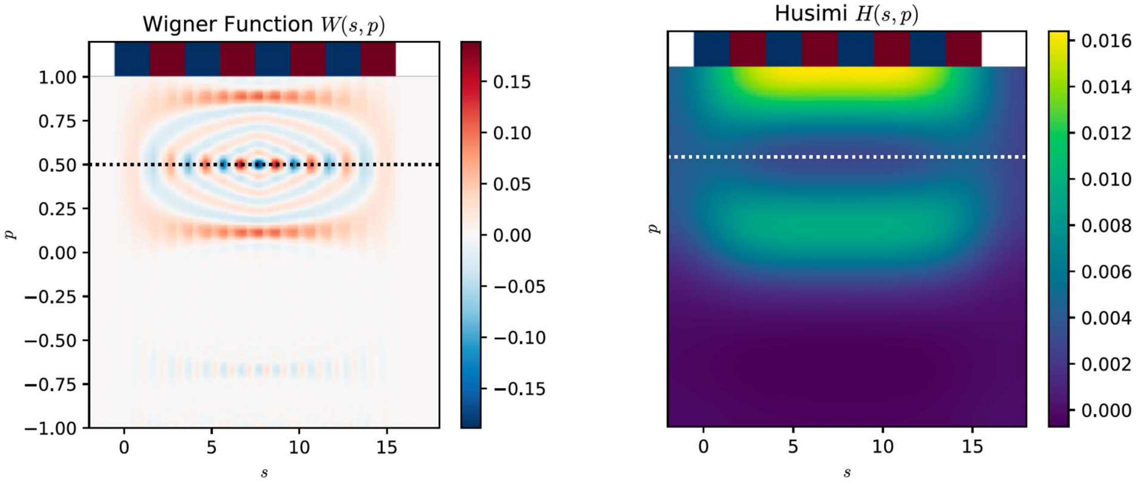

Figure 4-33 Phase-space anomalous reflection of a periodic RIS upon incidence at $p = {}^{1}/_{2}$.

Figure 4-2 Phase-space anomalous reflection of a periodic RIS upon incidence at $p = {}^{1}/_{2}$.

The next step is to integrate the model (4-2) in the DEA algorithm, which requires devising an procedure for the application of the transfer operator $\mathcal{T}$ in presence of non-uniform boundaries. The equilibrium HDF is found via the iterative map

$$\boldsymbol{H}(\boldsymbol{x},\boldsymbol{p}) = \sum_{\boldsymbol{s}=\boldsymbol{0}}^{\boldsymbol{S}} \boldsymbol{\mathcal{T}}^{\boldsymbol{s}}\, \boldsymbol{H}_{\boldsymbol{0}}(\boldsymbol{x},\boldsymbol{p})$$

4-15

which starts from a source distribution $H_0(x,p)$, and reaches an equilibrium distribution for $s \to \infty$, When the iteration hits the boundary, a local reflection/transmission map intervenes to establish the correct amount of energy that cross the boundary or get reinjected back into the confined environment. In this context, part of the wave density is captured by the RIS, where the engineered boundary condition is more complicated than a specular reflection. As the iterative transport proceeds, it is easy to imagine how an initial boundary distribution of waves develops a rich dynamics after a few iterations, on account of what is best known as multipath fading. Therefore, the RIS will be subject to multiple impinging plane waves coming simultaneously from various directions. We have developed a methodology that calculates the RIS scattered field under such a complex excitation field. The mathematical development, and the related integration with the DEA solver, is facilitated by the assumption that the plane waves generated by the environment scattering arrive at the RIS *incoherently*. More precisely, after making an iteration of the boundary density, we inspect the $\boldsymbol{x}$ domain related to the RIS collocation within the boundary and find the local maxima in p with associated weights. If we detect L local maxima, we assume there are L dominant plane waves with weights w_l for which we determine the associated scattered HSD $H_l(x,p)$ from (4-2), whence the updated boundary density to start the next iteration is given by

$$H(x,p) = \sum_{l=1}^{L} w_l\, H_l(x,p)$$

4-16

which provides an accurate approximation in presence of complex environments with rich scattering implying a large L covering the p range uniformly. More precisely, when a specific density of rays arrives at the boundary at each DEA iteration, the boundary map operates a specular reflection (in absence of the RIS) as depicted in Figure 4-3.

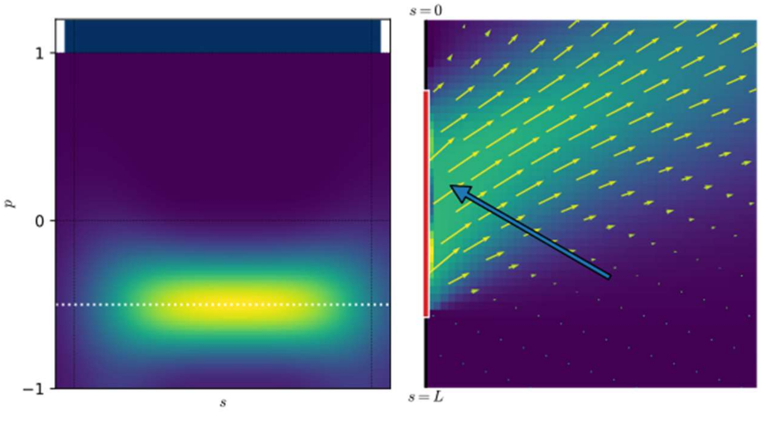

Figure 4-34 Specular reflection of a broad density of rays (approximating a plane wave) in phase space (left) and real space (right).

Figure 4-35 shows the anomalous reflection operated by a (finite size) binary RIS operated with periodic arrangements of the two states. The figure shows the difference between the achieved anomalous density and the specular reflection, which results only in an angular shift (linear momentum) and preserves the spatial localisation.

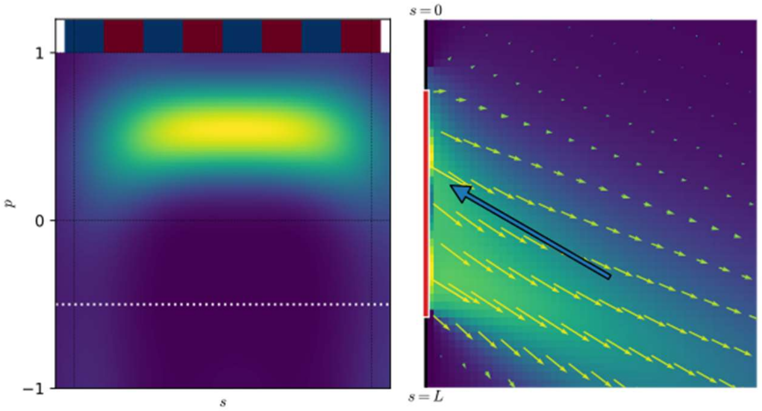

Figure 4-35 Anomalous reflection (against the specular reflection identified by the dashed white line) of a broad density of rays (approximating a plane wave) in phase space (left) and real space (right).

Figure 4-36 andFigure 4-37show the realization of beamforming in phase space, where localisation is achieved for both spatial and angular domains. The arrangement of pixel states is not regular anymore and the ray density can be shifted simultaneously in both position and momentum.

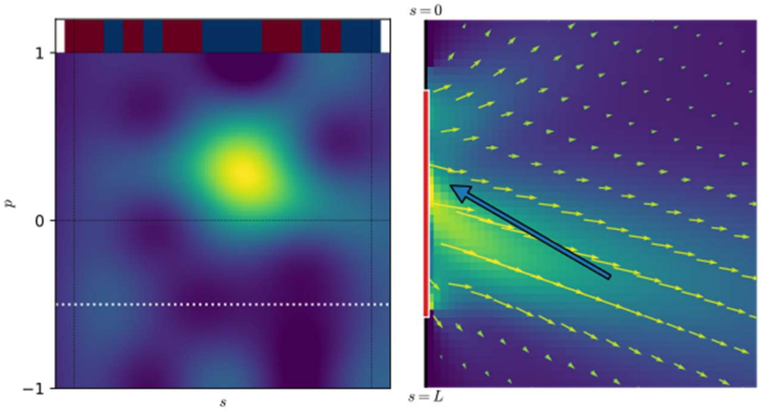

Figure 4-36 Beamforming of a density of rays (approximating a plane wave) in phase space (left) and real space (right) operated by an irregular arrangement of pixel states.

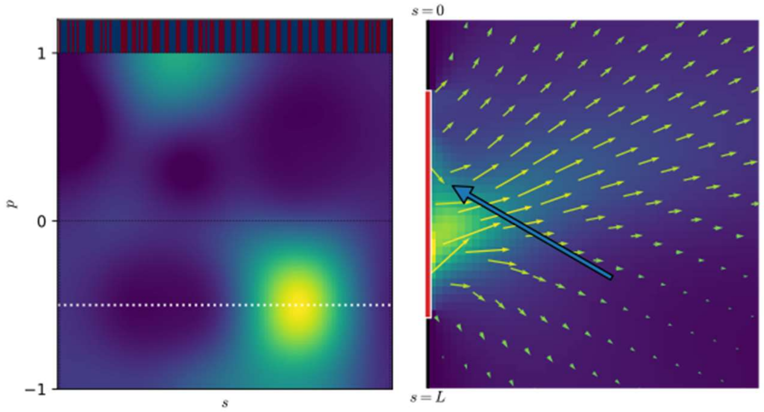

Figure 4-37 Beamforming of a density of rays (approximating a plane wave) in phase space (left) and real space (right) operated by an irregular arrangement of pixel states.

The 2D geometry that we used to perform a primary test our method is the L-shape corridor environment introduced in the previous reporting period, of interest in coverage extension studies. Figure 4-38 shows numerical results of energy focusing in a deployment scenario where the source is located at the bottom segment and there is no RIS deployed. As we can see from the phase space on the right-hand part of the figure, densities of rays arrive at limited parts of the boundary in presence of specular reflection. In other words, the densities are localized in both space and direction of travel.

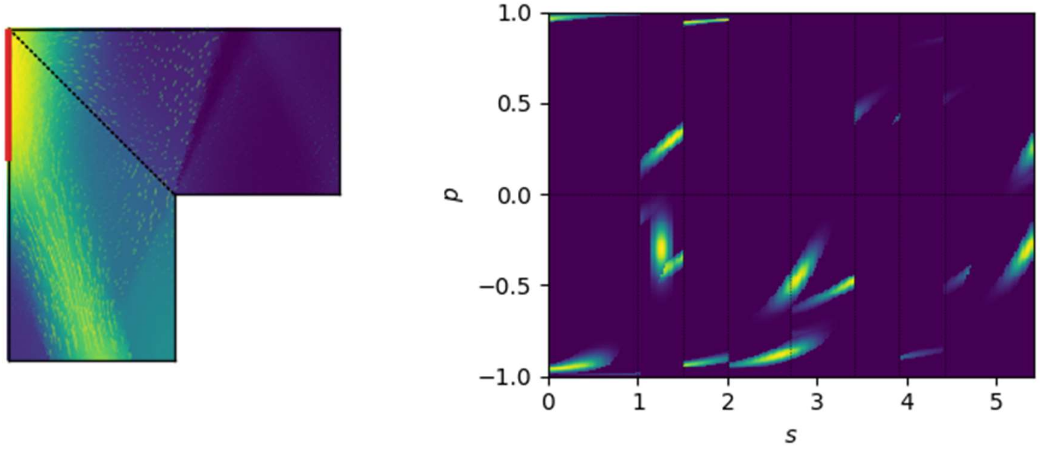

Figure 4-38 Optimization of the wave distribution in indoor environments without RIS. The configuration reported on the left indicates a (red solid) segment that act as a specular reflector). The phase-space reported on the right shows ray densities concentrated in both space and di

Figure 4-39 show numerical results for a RIS located in the top left segment. The phase space distribution shown in the right part of the figure indicates that the ray densities are smeared out after a few iterations of the DEA algorithm that accounts for the effect of the entire corner boundary self-consistently.

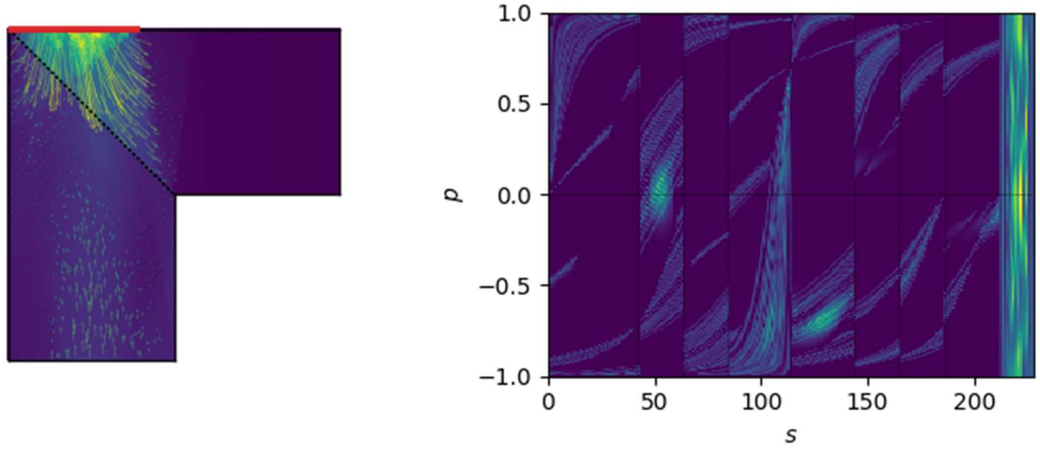

Figure 4-39 Optimization of the wave distribution in RIS-assisted indoor environments. The con-fig-uration reported on the left indicates a (red solid) segment that act as an anomalous reflector in the top left segment. The phase-space reported on the right shows ray den-sities diffused in both space and direction of travel.

Figure 4-40 show numerical results for a RIS located in the upper left segment. The effect of wave diffusion through a larger portion of the phase space is observed in the right part of the figure, as expected from Figure 4-39. However, we can appreciate that changing the location of the RIS has a substantial effect on the wave distribution within the environment as the parts of the spatial-angular parts covered in Figure 4-40 are different from those covered in the scenario of Figure 4-39.

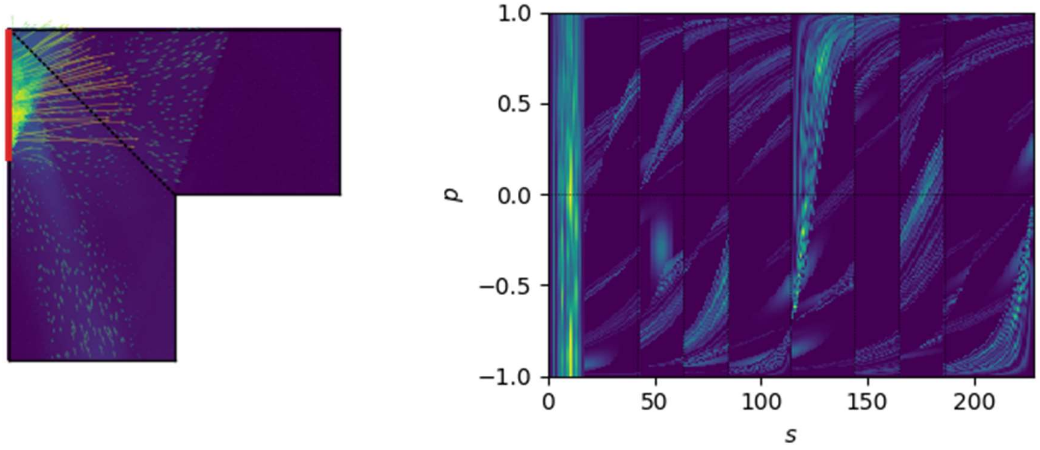

Figure 4-40 Optimization of the wave distribution in RIS-assisted indoor environments. The con-figuration reported on the left indicates a (red solid) segment that act as an anomalous reflector in the upper left segment. The phase-space reported on the right shows ray densities diffused in both space and direction of travel.

Further work is ongoing to extend the preliminary results achieved in this reporting period, with particular focus on the: i) formulation of accurate RIS scattering models upon incidence of arbitrary plane wave superposition, which helps treating incoherent wave densities incident upon the RIS at each DEA iteration. This can be tackled by a random plane wave spectrum approach developed in the theory of reverberation chamber [Arn06]; ii) inclusion of finite size RIS diffraction based on high frequency asymptotic EM field models, e.g., [VAK+23], in the phase-space language as outlined in [CSG+20]; iii) Efficient merging of closed-loop RIS optimization with computation of the equilibrium phase-space distribution for the confined environment, which is computationally intensive and constitutes the reason why only a few DEA iterations have been shown in this deliverable. This can be tackled by expressing the Wigner function in (4-2) on the basis function of a discrete, mesh-based, version of DEA achieved in a different field of application [CTL+13].

4.5 Reconfigurable Intelligent Surfaces in Propagation Environments with Scattering Objects

In this section, we summarize the contribution in [MPS23]. In particular, we extend the end-to-end mutual coupling aware and electromagnetic-compliant channel model, which was initially proposed in [GD21] for the case of pure LoS between Tx-RIS and RIS-Rx to the case of complex propagation environments with scattering clusters.

We consider the system model depicted in Figure 4-41, wherein a multi-antenna BS serves multiple single-antenna terminals with the aid of a $N = N_x \times N_y$ RIS whose antenna elements are spaced by d. Moreover, by exploiting the discrete dipole approximation [YH07], we model the scattering clusters as collections of thin-wire half-wavelength dipoles, that are assumed to be co-planar with the RIS.

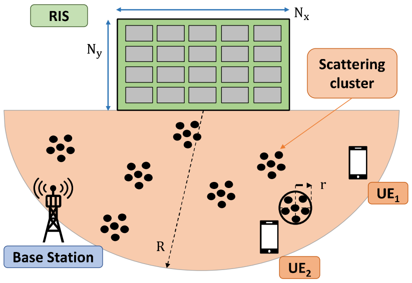

Figure 4-41: RIS-aided propagation environment with scattering clusters.

In this setting, we model the end-to-end MIMO channel as

$$\begin{gathered}\mathbf{H}_{E2E} = \left(\mathbf{I}_{\mathrm{L}} + \mathbf{Z}_{\mathrm{RR}}\mathbf{Z}_{\mathrm{L}}^{-1}\right)^{-1}\left[\mathbf{Z}_{\mathrm{RT}} - \mathbf{Z}_{\mathrm{RE}}(\mathbf{Z}_{\mathrm{EE}} + \mathbf{Z}_{\mathrm{SC}})^{-1}\mathbf{Z}_{\mathrm{ET}}\right](\mathbf{Z}_{\mathrm{TT}} + \mathbf{Z}_{\mathrm{G}})^{-1} \in \mathbb{C}^{L \times M} \\ \mathbf{Z}_{\mathrm{EE}} = \begin{bmatrix} \mathbf{Z}_{\mathrm{OO}} & \mathbf{Z}_{\mathrm{OS}} \\ \mathbf{Z}_{\mathrm{SO}} & \mathbf{Z}_{\mathrm{SS}} \end{bmatrix}, \mathbf{Z}_{\mathrm{RE}} = \begin{bmatrix} \mathbf{Z}_{\mathrm{RO}} & \mathbf{Z}_{\mathrm{RS}} \end{bmatrix}, \mathbf{Z}_{\mathrm{ET}} = \begin{bmatrix} \mathbf{Z}_{\mathrm{OT}}{}^{\mathbf{T}} & \mathbf{Z}_{\mathrm{ST}}{}^{\mathbf{T}} \end{bmatrix}^{\mathbf{T}} \\ \mathbf{Z}_{\mathrm{SC}} = \begin{bmatrix} \mathbf{Z}_{\mathrm{US}} & \mathbf{0} \\ \mathbf{0} & \mathbf{Z}_{\mathrm{RIS}} \end{bmatrix}\end{gathered} \tag{4-1}$$

where the code letters $\mathrm{R}, \mathrm{T}, \mathrm{S}, \mathrm{O}$ stand for the Rx, Tx, RIS and scattering objects, respectively. Moreover, $\mathbf{Z}_{\mathrm{US}}$ is a diagonal matrix modelling the loads of each scattering dipole. In this way, by suitably adjusting such load we can model any kind of realistic scattering object. Lastly, the tunable RIS impedance matrix is modelled as

$$\mathbf{Z}_{\mathbf{RIS}} = \mathbf{diag}[\mathbf{R_0} + \boldsymbol{j x_n}]_{\boldsymbol{n}=\mathbf{1}}^{\mathbf{N}} \tag{4-2}$$

with R_0 a constant value modelling the RIS internal circuit losses, and x_n the tunable reactance of each RIS unit cell.

We highlight that this model is more complex than standard additive multipath models [ADD21], since it accounts for the interaction between the RIS and the scattering objects, as well as between the objects themselves. Indeed, existing additive multipath models can be recovered as a special case of the above model by setting $\mathbf{Z}_{\mathrm{OS}} = \mathbf{Z}_{\mathrm{SO}} = \mathbf{0}$, i.e., ignoring the aforementioned interactions between the RIS and the scattering objects.

In this context, we formalize the problem of jointly optimizing the BS and RIS active and passive beamforming vectors, respectively, via the RISMA framework in [MGS21]. Specifically, by exploiting the iterative application of the Neumann series [QD21] and a series of mathematical reformulations, we are able to cast the problem in the same bi-convex nature of [MSG21]. The formulated optimization algorithm is dubbed as *SARIS.*

4.5.1 Application of RIS model based on mutually coupled loaded wire dipoles

In the following we provide some applications of the model described in Section 4.5. In particular, we briefly overview the achievable performance of two optimization algorithms based on the latter, which are described in [MPS23] and [EQJ23], respectively. Indeed, both contributions investigate a scenario involving a MIMO system with a RIS, taking into account the presence of scattering objects as proposed in Section 4.5 (see [MPS23]). More details on the specific optimization methods utilized by the two contributions are described in the relevant WP4 deliverables.

In the latter, we provide some numerical results of a $\mathrm{L} = 2$ UE setting by comparing SARIS with two reference schemes, namely the block-coordinate descent weighted MMSE (BCD wMMSE) algorithm in [ADD21] and a *mismatched* model, which corresponds to ignoring the interactions between the RIS and the scattering objects (i.e., by setting $\mathbf{Z}_{\mathrm{OS}} = \mathbf{Z}_{\mathrm{SO}} = \mathbf{0}$). In Figure 4-42 we show the convergence of the considered algorithms for different values of N and d on the left-hand side, while we show the convergence versus the value of R_0 for $\mathrm{N} = 64$ and $\mathrm{d} = \lambda/8$. Here, we demonstrate how SARIS is both faster and more stable than reference schemes. In Figure 4-43, we show the achievable sum-rate of the considered schemes versus the number of UEs L (left-hand side) and the number of scattering clusters $\mathrm{N_c}$ (right-hand side), for different values of N and d. Details on the numerical results can be found in [MPS23].

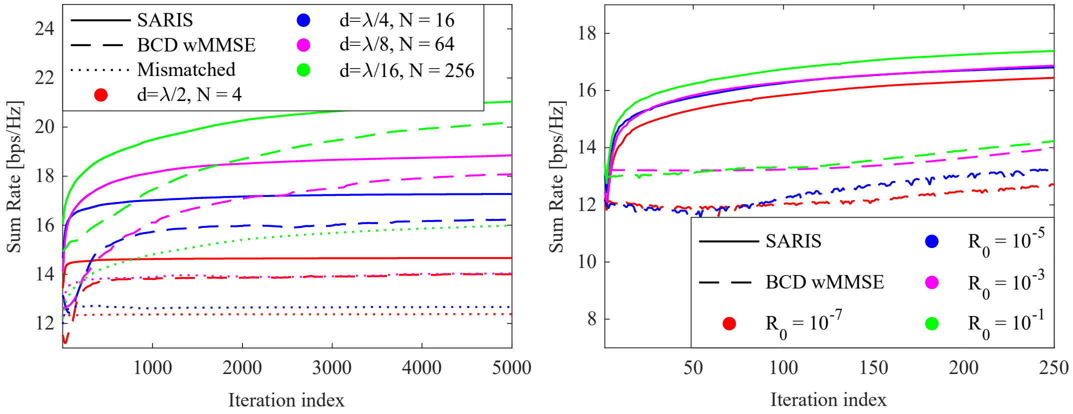

Figure 4-42 SARIS algorithm convergence for different values of N and d (left-hand side) and R_0 (right-hand side).

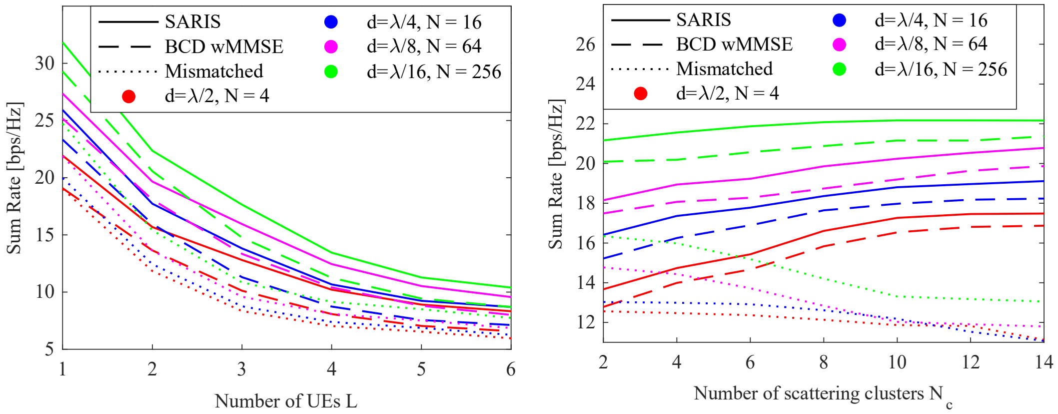

Figure 4-43: Sum rate obtained with SARIS and the reference schemes versus the number of UEs L (left-hand side) and the number of scattering clusters $\mathrm{N_c}$ (right-hand side), for different values of N and d.

While the algorithms presented in previous works [QD21], [ADD21] and [MPS23] utilize the Neumann series approximation to address the optimization problem involving the tunable impedances of the RIS, the significant contribution of [EQJ23] lies in the development of an algorithm that does not rely on any approximations when applied to RIS-aided MIMO systems. The approach involves iterative optimization of the tunable load impedances one by one where at each iteration, we employ the Gram-Schmidt orthogonalization method to obtain a closed-form solution.

In the following we provide some numerical results where we consider a 4-antenna transmitter and a single-antenna receiver. Observing Figure 4-44, we see that Algorithm 1 in our contribution [EQJ23] outperforms the algorithms [8] in [ADD21] and [9] in [MPS23]. Algorithm 1 exhibits two notable advantages: (i) faster convergence and (ii) achieving a higher rate value. These benefits can be attributed to two key features: its avoidance of the Neumann series approximation and the utilization of closed-form expressions for the solution at each iteration.

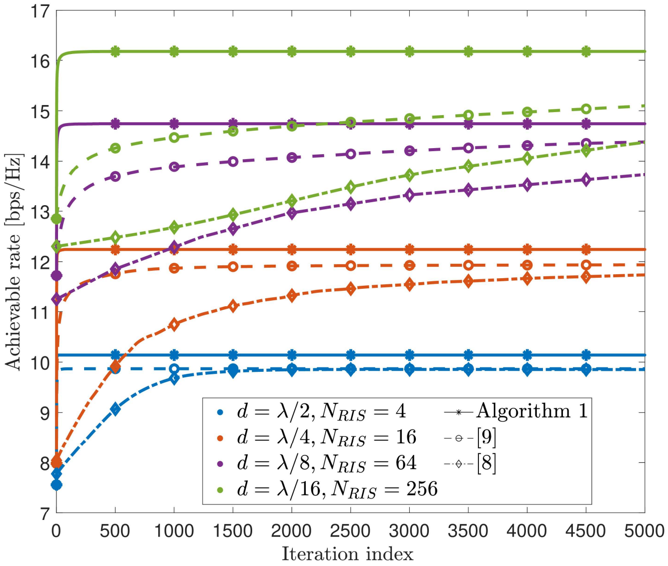

Figure 4-44 Comparison of the convergence of the algorithms [iterations].

Table 4-2 shows the convergence time (in seconds) for the algorithms. We can see that Algorithm 1 consistently achieves the highest rate value, while the algorithms in [ADD21] and in [MPS23], on average with respect to d, reach approximately 90% and 98% of Algorithm 1's rate upon convergence. The table also includes the execution times for the algorithms in [ADD21] and [MPS3] to converge, as well as the execution time for Algorithm 1 to reach 90% and 98% of the rate that it achieves at convergence. We see that Algorithm 1 demonstrates significant advantages, particularly for smaller values of the inter-distance d.

Table 4-2 Comparison of the execution time [seconds].

d	**Algo. 1** (90%)	**[8]**
$\lambda/2$	0.001	0.800
$\lambda/4$	0.004	0.770
$\lambda/8$	0.167	8.135
$\lambda/16$	16.530	213.128

d	**Algo. 1** (98%)	**[9]**
$\lambda/2$	0.001	0.0154
$\lambda/4$	0.008	0.896
$\lambda/8$	0.834	27.686
$\lambda/16$	170.807	946.404

More details on the derivations and the numerical results can be found in [EQJ23].

4.6 Propagation environment with scattering objects and random variability (NEC, UNOT, CNRS,)

In Section 3.1, we introduced an electromagnetic-compliant and mutual coupling-aware channel model for RIS-aided networks, which includes the presence of scattering objects modelled as loaded wire dipoles. However, given the 3D coordinates of all dipoles in the environment, such model is deterministic and deals mainly with large-scale fading channel conditions.

In this section, we further extend this approach to account for random variability in the propagation environment, e.g., user mobility or fast-fading conditions. In this regard, we capitalize on the random coupling model (RCM) in [GYX14], which provides a statistical model for the wave behaviour of large irregular cavities connected by one or more ports. Indeed, we model the random variability of the environment between any two dipoles in our system as a closed cavity wherein the ray trajectories are chaotic.

To this end, we model the self and mutual impedances between any two dipoles q, p in the aforementioned cavity as

$$\boldsymbol{Z}_{pp}^{cav} = \boldsymbol{j}\, \Im(\boldsymbol{Z}_{pp}) + \left[\Re(\boldsymbol{Z}_{pp})\right]^{\frac{1}{2}}\ \Xi_{pp}\ \left[\Re(\boldsymbol{Z}_{pp})\right]^{\frac{1}{2}}$$
$$\boldsymbol{Z}_{qp}^{cav} = \boldsymbol{Z}_{qp} + \left[\Re(\boldsymbol{Z}_{qq})\right]^{\frac{1}{2}}\ \Xi_{qp}\ \left[\Re(\boldsymbol{Z}_{qq})\right]^{\frac{1}{2}}$$

4-17

where Z_{pp}, Z_{qp} are the deterministic self and mutual impedances between any two dipoles q, p, which can be obtained as described in Section 3.1, and $\Im, \Re$ stand for the imaginary and real part, respectively. Moreover, the random matrices Ξ_{qp}, which incorporate homogeneous cavity losses, are defined as

$$\Xi_{pq} = -\frac{\boldsymbol{j}}{\boldsymbol{\pi}} \sum_{\boldsymbol{n}}^{\boldsymbol{N_s}} \frac{\boldsymbol{\phi}_{\boldsymbol{p},\boldsymbol{n}} \boldsymbol{\phi}_{\boldsymbol{q},\boldsymbol{n}}^{\boldsymbol{T}}}{\mathrm{K}_0^2 - \mathrm{K}_{\boldsymbol{n}}^2 + \boldsymbol{j\alpha}} \quad \forall \boldsymbol{p}, \boldsymbol{q}$$

4-18

where N_s is the size of the cavity (i.e., number of modes), $\mathrm{K}_n^2 = \kappa_n^2/\Delta\kappa^2, n \geq 0$, with $\Delta\kappa^2$ the mean mode spacing and κ_n^2 the eigenvalues of a matrix selected from the Gaussian orthogonal ensemble, $\boldsymbol{\phi}_{p,n}$ is a vector of uncorrelated, zero mean, unit width Gaussian random variables, which represent (unitless) random coupling coefficients between port current profiles and cavity eigenmodes, and $\alpha \geq 0$ is a loss parameter, which incorporates the effect of wall losses, internal homogeneous losses and the cavity dimensions. We remark that as α increases, the environment becomes increasingly lossy and tends to behave as a free-space setting. Indeed, for large α we get $\Xi_{pq} \xrightarrow[\alpha\to\infty]{} 0$ and $\Xi_{pp} \xrightarrow[\alpha\to\infty]{} \mathrm{I}$, where I is the identity matrix. Therefore, for large values of α, we recover exactly the same self and mutual impedances Z_{qp} as described in Section 3.1.

In order to verify such *channel hardening* effect, we generate 10^3 independent random realizations of all impedances and apply the SARIS [MPS23] optimization algorithm to both the transmitter and the RIS, by assuming perfect instantaneous CSI. In Figure 4-45, on the left-hand side we show the average rate obtained with SARIS versus the number of RIS antennas N and for different values of α. Moreover, we show the associated standard deviation of each mean value. On the right-hand side we show the variance of the rate divided by the square of its mean, thus effectively demonstrating the channel hardening effect for large values of N and α.

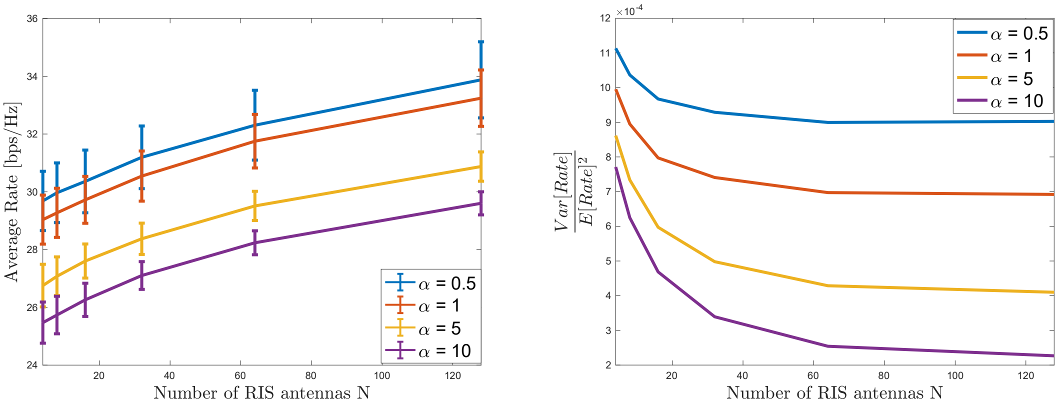

Figure 4-45: Average Rate (left-hand side) and channel hardening metric (right-hand side) obtained with SARIS versus the number of RIS antennas N and for different values of the cavity

4.7 Relation between impedance-based and system-level channel models

The E2E impedance matrix model in Sec 3.1 can be related to system level models that are widely adopted in the scientific literature for performance analysis. This constitutes the core of the harmonization procedure, bringing together all the models adopted in this project (legitimately different because of the heterogeneous needs among technical work packages). In particular, the task entails finding a mathematical relation between RIS port impedances and wave reflection coefficient [AZW+20], as well as expressing the mutual impedance between RIS and Tx/Rx antennas as a complex channel gain [NJS+21]. Furthermore, in order to make the harmonization procedure generic and useful in practice, the solution should stand on scattering/impedance parameters obtained from full wave simulation of the unloaded (open circuited, with no tuneable circuitry) planar structure.

The method we devise is based on macro-modelling of the RIS unit cell terminated by PBC. Our discussion is based on the unloaded resonator configuration in Fig. 3-8, which provides a direct way to characterize the wave reflection coefficient through simulated impedance parameters. As pointed out in Sec. 3.3, given a TE/TM plane wave impinging on the structure at some angle, the structure develops Floquet modes on account of periodicity modelled by PBC. As explained in Sec. 3.3, we have two types of ports: i) a Floquet port that corresponds to a selected mode; ii) a circuital port, to which tuneable circuitry, e.g., embedding pin diodes or varactors, is connected. Whilst this approach was originally proposed in [BAM10] for reflectarrays, and recently put forward as a macro-model for the RIS [ZZW+22], here we use the theory to find a relation between the impedance model validated in Sec. 3.2 and system models used in the literature, where the RIS codebook is usually specified in terms of phase shift of the wave reflection coefficient.

We start from the two-port system depicted in Figure 4-46, which is now treated with the classical circuit theories.

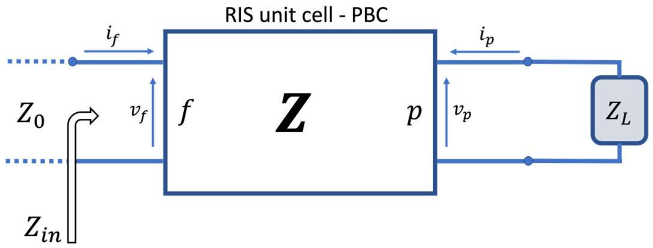

Figure 4-46 Port-based representation of the (single-mode) loaded RIS unit cell. The input Z_in and incident wave Z_0 impedances are reported.

Inherently, the wave reflection coefficient (at the Floquet port) r can be derived from the associated constitutive equations

$$\begin{cases} v_f & = Z_{ff} i_f & + Z_{fp} i_p \\ v_p & = Z_{pf} i_f & + Z_{pp} i_p \end{cases}$$

4-19

Which define the 'port' voltages v and currents i depicted in the scheme of Figure 4-46 Importantly, voltages and currents at the Floquet ports are defined by the transformation of the scattering matrix into the impedance matrix whose entries are involved in the constitutive equations of (4-19). Now, consider that the circuital port is loaded by the equivalent circuit of the tuneable electronic components, we can write the boundary condition

$$\boldsymbol{v_p} = -\boldsymbol{Z_L}\, \boldsymbol{i_p}$$

4-20

which after simple algebraic manipulations yields the expression

$$r = \frac{Z_{in} - Z_0}{Z_{in} + Z_0} = \frac{Z_{ff} - \frac{Z_{fp} Z_{pf}}{Z_{pp} + Z_L} - Z_0}{Z_{ff} - \frac{Z_{fp} Z_{pf}}{Z_{pp} + Z_L} + Z_0}$$

4-21

where $Z_0 = \sqrt{\mu_0 / \varepsilon_0} \approx 377\ \Omega$, whose behaviour with the load impedance $Z_{\boldsymbol{L}}$ shows the same trend of the circuit-based reflection coefficient expression in [AZW+20], obtained by modelling the RIS with a surface impedance. The expression in (4-21) can be related to the RIS admittance matrix

$$\boldsymbol{\Phi} = (\boldsymbol{Z}_{SS} + \boldsymbol{Z}_{RIS})^{-1}$$

4-22

that appears in the impedance model (3-1), for the case of large RIS structures where

$$\boldsymbol{\Phi} = \boldsymbol{I}\Phi = \boldsymbol{I}\,(Z_{SS} + Z_{RIS})^{-1}$$

4-23

leading to

$$r = \frac{Z_0 - Z_{ff} + Z_{fp} Z_{pf} \Phi}{Z_0 + Z_{ff} - Z_{fp} Z_{pf} \Phi}$$

4-24

It is worth pointing out that the use of r in practice is limited to relatively large planar periodic structures. In the context of RIS, we argue that this is useful for modelling individual macro-cells with dimensions of a few wavelengths, an approximation that is widely used in the scientific literature. Equation (4-24) allows for converting the reflection codebooks into the complex-valued RIS state (admittance) matrix adopted in the impedance model, viz.,

$$\Phi = \frac{(r+1)\, Z_{ff} + (r-1)\, Z_0}{(r-1)\, Z_{pf} Z_{fp}}$$

4-25

The last step towards unveiling the relation between impedance-based and system-level channel models consists of mapping the complex-valued channel gains onto impedance matrices. This can be readily done for any trans-impedance matrix of radiating elements operating at far-field distance, by using the array steering vectors as an intermediate representation. Using basic circuit analysis and after some algebraic passages, it is possible to obtain a far-field expression for the transimpedance in terms of array steering vectors, as shown in [INo10, ASB+22]

$$\boldsymbol{Z_{TR}} = \boldsymbol{\gamma} \frac{\boldsymbol{e^{-j\varphi}}}{\boldsymbol{2\pi\, r^d}} \sqrt{\boldsymbol{G_T\, G_R}}\ \mathbf{diag}(\Re\{\boldsymbol{Z_{RR}}\})^{\frac{1}{2}}\ \boldsymbol{a_R}(\boldsymbol{\theta_R})\ \ \boldsymbol{a_T^T}(\boldsymbol{\theta_T})\ \mathbf{diag}(\Re\{\boldsymbol{Z_{TT}}\})^{\frac{1}{2}},$$

4-26

which depends on frequency, and where the complex-valued pre-factor depends on the radiation patterns of the (two) antennas involved in the transmission. Gathering all the information together, under the approximations discussed above, leads to a systematic procedure that maps the impedance model onto the system model that is widely adopted in the wireless communication community. More precisely, given a specific RIS unit cell structure, their CAD model, and identified both Floquet and circuital ports, we proceed by:

1. Performing full-wave simulations of the RIS unit cell with PBC, under a selected Floquet mode dictated by the angle of incidence, and for the cell with circuital port in open circuit conditions.
2. Extracting the impedances Z_{ff}, Z_{pf}, Z_{fp}, and Z_{pp}.
3. Devising the equivalent impedance of the tuning circuitry $Z_{\boldsymbol{L}}$.
4. Performing full-wave simulations of the RIS unit cell with PBC, under the same Floquet mode selected in 1., and for the cell with circuital port loaded by the control circuitry (to be repeated at different RIS unit cell state).
5. Extracting the reflection coefficient r_u at the Floquet port for the RIS unit cell at state u.
6. Forming the $N \times N$ RIS state matrix $\boldsymbol{\Phi}$ in (5-5) for a specific finite-size RIS with N macro-pixels (in general, with UC at different reflective state).
7. Performing full wave simulations of the RIS, Tx, and RX antenna arrays to extract the active impedance matrices Z_{TT}, $Z_{\boldsymbol{RR}}$, and Z_{SS}.
8. Devising the array steering vectors, relative phase difference, as well as the RIS unit cell, Tx, and Rx antenna element gains $\boldsymbol{G_T}$, G_R, and G_S.
9. Forming the transimpedances $Z_{\boldsymbol{TR}}$, Z_{RS}, and Z_{ST} by using the outcome of steps 7. – 8. in the form (5-8).
10. Inserting the outcome of steps 6. and 9. in (4-26) and tweaking the constants $\boldsymbol{\gamma}$ in the transimpedances.

The harmonization procedure is important as it allows to provide a physics-based MIMO communication model where the optimization is carried out with respect to the circuital parameters in $\mathbf{\Phi}$ through Z_L. Importantly, besides the validation in Section 3.1, it has been recently shown that the same mathematical structure of (3-1) is obtained through the interaction formalism of the MoM [KTC+23].

Interestingly, both the active impedance $Z_{in} = Z_{pp}$ and the tuneable circuitry Z_L impedances are used in the 'distorted' inverse-Lorentzian (3-18) of Sec. 3.3, which effectively predicts the reflection coefficient (5-6). Therefore, given a specific configuration where an oblique plane wave impinges upon an unloaded RIS, only a one-off simulation is required to characterize the structural properties (in the form of scattering parameters) of the two-port Floquet-circuit system, required by channel mode and subsequently needed for RIS optimization. The presence of mutual coupling and finite size effects, as well as multi-resonance RIS unit cells, can be tackled by extending CMT and the circuit theory adopted in these sections to a scenario with multiple Floquet and circuital ports.

For validation of the impedance model we used the RIS prototype described in section 2.4, where the unit cell is a dual-polarized patch antenna with MEMS-based phase shifters on each polarization feed. The unit cell is capable of varying phase in 360 degree range with discrete steps given by the capacitance resolution of the MEMS chips. Each phase shifter consists of two variable-capacitance MEMS chips, one right next to the coaxial feed (“close”), and the other at the end of a short segment of coplanar waveguide (“distant”), in parallel configuration . By varying the capacitance of one MEMS chip from 0.23 to 2.7 pF, the phase shifter realizes approximately one half of the full 360 degree phase range. The second half of the phase range is realized by varying the capacitance of the other MEMS chip.

In the impedance modelling, we replace the MEMS chip with the load impedance $Z_L = 1/j\omega C$ where C is the MEMS capacitance varied from 0.23 to 2.7 pF in 32 steps. The reflection coefficient is then expressed using (4-21) and the Z-matrix.

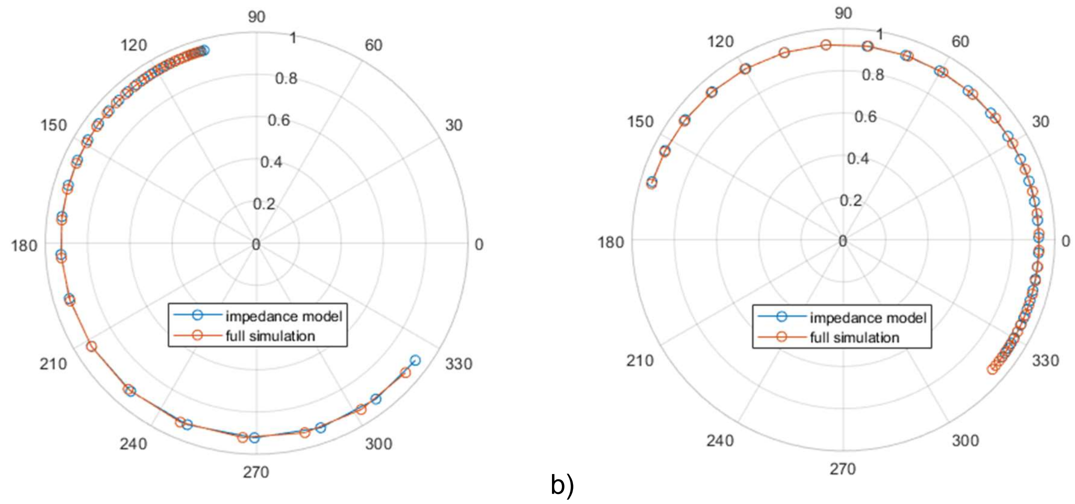

a) b)

Figure 4-47 Reflection coefficient of the vertical Floquet mode for the AAU prototype at 3.7 GHz when one of the MEMS capacitors is varied: a) “close”, b) “distant”

Figure 4-46 shows the reflection coefficient (S11) at the vertical Floquet port of the AAU RIS unit cell obtained from full simulation by CST MWS (red) and by the impedance model (blue) at frequency 3.7 GHz. The left and right plots show the variations of the “close” MEMS and the “distant” MEMS. In both cases, the match is very good, and the remaining errors are arguably due to slight differences between the full and the Z-matrix simulations.

Interestingly, both the active impedance $Z_{in} = Z_{pp}$ and the tuneable circuitry Z_L impedances are used in the 'distorted' inverse-Lorentzian of Sec. 3.2, which effectively predicts the reflection coefficient. Therefore, given a specific configuration where an oblique plane wave impinges upon an unloaded RIS, only a one-off simulation is required to characterize the structural properties (in the form of scattering parameters) of the two-port Floquet-circuit system, required by channel mode and subsequently needed for RIS optimization. The presence of mutual coupling and finite size effects, as well as multi-resonance RIS unit cells, can be tackled by extending CMT and the circuit theory adopted in this section to a scenario with multiple Floquet and circuital ports.

Finally, we show that the impedance-based harmonization with system-level communication models can be pushed further ahead to establish a link with path-loss models. Inherently, the power received at the receiver load reads

$$P_{\boldsymbol{R}} = -\frac{1}{2Z_L}|V_R|^2 = -\frac{1}{2Z_L}|H_{E2E}|^2|V_G|^2$$

4-27

which becomes, using the E2E channel model, and in absence of LOS between Tx and Rx antennas

$$H_{E2E} = -Y_0\, Z_{RS}\, \Phi\, Z_{ST}$$

4-28

and adopting 4-26 appropriately

$$P_R = -\frac{|Y_0|^2|V_G|^2}{2Z_L}\,\frac{G_T\, G_S^2\, G_R}{4\pi^2 r_{RS}^d\, r_{RS}^l}\gamma_{RS}\,\gamma_{ST}$$
$$\left|\mathrm{diag}(\Re\{Z_{RR}\})^{\frac{1}{2}}\ a_R(\theta_R)\ \ a_S^T(\theta_S)\ \mathrm{diag}(\Re\{Z_{SS}\})^{\frac{1}{2}}\ \Phi\ \mathrm{diag}(\Re\{Z_{SS}\})^{\frac{1}{2}}\ a_S(\theta_S)\ \ a_T^T(\theta_T)\ \mathrm{diag}(\Re\{Z_{TT}\})^{\frac{1}{2}}\right|^2$$

4-29

for which we require knowledge – by independent full-wave simulations – of both the active impedance $\boldsymbol{Z}_{SS}$ and the unit element gain G_S of the RIS, as well as of both the transmit and the receive array. For single-antenna transmitters and receivers as in VNA-based laboratory measurements, the path loss simplifies to

$$P_R = -\frac{|Y_0|^2|V_G|^2}{2Z_L}\,\frac{G_T\, G_R}{4\pi^2 r_{RS}^d\, r_{RS}^l}\gamma_{RS}\,\gamma_{ST}\,\sqrt{\Re\{Z_{TT}\}}\,\sqrt{\Re\{Z_{RR}\}}$$
$$G_S^2\left|a_S^T(\theta_S)\ \mathrm{diag}(\Re\{Z_{SS}\})^{\frac{1}{2}}\ \Phi\ \mathrm{diag}(\Re\{Z_{SS}\})^{\frac{1}{2}}\ a_S(\theta_S)\right|^2$$

4-30

Furthermore, the power injected in the transmit antenna P_T can be made explicit and can be used upon simulation of the end-to-end scenarios presented in the previous sections, just through knowledge of the RIS codebook in terms of reflection coefficient r.

5 Conclusions

The design and prototypes developed in the project encompass a large number of different technologies and frequency bands, spanning from sub-6GHz to THz (D-Band).
Different unit cell concepts based on Pin diode technologies, varactor, MEMS and RF switches, as well monolithic technologies. According to the technology different degrees of reconfigurability can be achieved. These prototypes and designs have been successfully employed for WP2 analysis on Band of Interest and Area of Interest.

RIS design have also been used to validate different modelling approaches that have been successfully employed to increase the connectivity and localization accuracy. In particular an important step has been moved for the improvement of a widely employed impedance model. Going beyond the minimum scattering antenna simplification of the unit cells, it has been validated on more complex multi-port designs, thanks to a careful simulation campaign. This model has been also extended to the multipath scenario by representing scatterers as clusters of loaded dipoles. Additionally resonant and hybrid (ray-tracing/full-wave) model have been validated. Finally new FDTD tools have been implemented to simulate RIS.
A relationship between impedance and “signal-processing” models has been also discussed in order to easily move to different formalism.

Before the RIS deployment for the Proof of Concept, the prototypes have been employed in different channel measurement campaign in indoor and reverberation chamber. It has been shown how the channel is indeed modified by the RIS, but its contribution should be carefully analysed also employing some high resolution techniques. Among the different campaigns, one have been employing for the first time multiple transmitting and reflecting RIS, and constitute a relevant basis for the assessment of the project investigation, as localization enhancement.

In summary, the porotypes and measurement here presented allow to assess their functionality, while the impact on the system performance will be showcased in the final demonstrators (WP7).

6 References

[ADD21]	A. Abrardo, D. Dardari, M. Di Renzo and X. Qian, "MIMO Interference Channels Assisted by Reconfigurable Intelligent Surfaces: Mutual Coupling Aware Sum-Rate Optimization Based on a Mutual Impedance Channel Model," in *IEEE Wireless Communications Letters*, vol. 10, no. 12, pp. 2624-2628, Dec. 2021, doi: 10.1109/LWC.2021.3109017.
[CBM23]	E. Colella, L. Bastianelli, V. Mariani Primiani, F. Moglie, “FDTD full wave simulations of reconfigurable intelligent surfaces”, submitted and accepted to International Symposium Electromagnetic Compatibility, EMC Europe 2023, Kracow, Poland, September 2023.
[Arn06]	L. R. Arnaut, “Spatial correlation functions of inhomogeneous random electromagnetic fields,” in Physical Review E, 73(3), p.036604, 2006.
[ASB+22]	M. Akrout, V. Shyianov, F. Bellili, A Mezghani, R.W. Heath, “Super-Wideband Massive MIMO,” arXiv preprint arXiv:2208.01556, 2022.
[AZW+20]	S. Abeywickrama, R. Zhang, Q. Wu and C. Yuen, "Intelligent Reflecting Surface: Practical Phase Shift Model and Beamforming Optimization," in IEEE Transactions on Communications, vol. 68, no. 9, pp. 5849-5863, Sept. 2020, doi: 10.1109/TCOMM.2020.3001125.
[BAM10]	L. Boccia, G. Amendola and G. D. Massa, "Performance Improvement for a Varactor-Loaded Reflectarray Element," in IEEE Transactions on Antennas and Propagation, vol. 58, no. 2, pp. 585-589, Feb. 2010, doi: 10.1109/TAP.2009.2037697.
[CSG+20]	S. C. Creagh, M. Sieber, G. Gradoni, G. Tanner, “Diffraction of Wigner functions,” Journal of Physics A: Mathematical and Theoretical, 54(1), p.015701, 2020.
[CTL+13]	D. J. Chappell, G. Tanner, D. Löchel, N. Søndergaard, “Discrete flow mapping: transport of phase space densities on triangulated surfaces,” Proceedings of the Royal Society A: Mathematical, Physical and Engineering Sciences, 469(2155), p.20130153, 2013.
[DCD16]	L. Di Palma, A. Clemente, L. Dussopt, R. Sauleau, P. Potier, and P. Pouliguen, “1-Bit Reconfigurable Unit Cell for Ka-Band Transmitarrays,” IEEE Antennas and Wireless Propagation Letters, vol. 15, pp. 560-563, 2016.
[DAH98]	D. A. Hill, “Plane wave integral representation for fields in reverberation chambers,” IEEE Trans. Electromagn. Compat., vol. 40, no. 3, pp. 209-217, Aug. 1998.
[EQJ23]	H. El Hassani, X. Qian, S. Jeong, N. S. Perović, M. Di Renzo, P. Mursia, V. Sciancalepore, X. Costa-Pérez. “Optimization of RIS-Aided MIMO -- A Mutually Coupled Loaded Wire Dipole Model”, 2023, [Online]: https://arxiv.org/abs/2306.09480
[FCB21]	F. Costa and M. Borgese, "Electromagnetic Model of Reflective Intelligent Surfaces," in IEEE Open Journal of the Communications Society, vol. 2, pp. 1577--1589, 2021, doi: 10.1109/OJCOMS.2021.3092217.
[GD21]	G. Gradoni, and M. Di Renzo, End-to-End Mutual Coupling Aware Communication Model for Reconfigurable Intelligent Surfaces: An Electromagnetic-Compliant Approach Based on Mutual Impedances. *IEEE Wireless Communications Letters, 2021*

[GPO21]	J.B. Gros, V. Popov, M. Odit, V. Lenets, and G. Lerosey, “A Reconfigurable Intelligent Surface at mmWave Based on a Binary Phase Tunable Metasurface,” IEEE Open Journal of the Communications Society, vol. 2, pp. 1055-1064, 2021.
[GPOL21]	J.B. Gros, V. Popov, M. Odit, and G.Lerosey, “A wave physics approach to electronically steerable antennas,” Small Satellite Conference, 2021
[GYX14]	G. Gradoni, J. H. Yeh, B. Xiao, T. M. Antonsen, S. M. Anlage, and E. Ott, “Predicting the statistics of wave transport through chaotic cavities by the random coupling model: A review and recent progress.” *Wave Motion*, *51*(4), 606–621, 2014.
[HTa03]	K. Haneda and J.I. Takada, “An application of SAGE algorithm for UWB propagation channel estimation,” IEEE Conference on Ultra Wideband Systems and Technologies, 2003, Reston, VA, USA, 2003, pp. 483-487.
[INo10]	M. T. Ivrlač and J. A. Nossek, "Toward a Circuit Theory of Communication," in IEEE Transactions on Circuits and Systems I: Regular Papers, vol. 57, no. 7, pp. 1663-1683, July 2010, doi: 10.1109/TCSI.2010.2043994.
[KSI+22]	K. D. Katsanos, N. Shlezinger, M. F. Imani and G. C. Alexandropoulos, "Wideband Multi-User MIMO Communications with Frequency Selective RISs: Element Response Modeling and Sum-Rate Maximization," 2022 IEEE International Conference on Communications Workshops (ICC Workshops), Seoul, Korea, Republic of, 2022, pp. 151-156, doi: 10.1109/ICCWorkshops53468.2022.9814515.
[KTC+23]	K. Konno, S. Terranova, Q. Chen, G. Gradoni, “Generalised Impedance Model of Wireless Links Assisted by Reconfigurable Intelligent Surfaces,” arXiv preprint arXiv:2306.03761, 2023.
[KYE13]	heoretical analysis on reflection properties of reflectarray unit cells using quality factors,” IEEE Trans. Antennas Prop., vol. 61, no. 1, pp. 201–210, Jan. 2013.
[LAD99]	Ladbury, J. M., “Monte Carlo simulation of reverberation chambers”, Technical report, National Institute of Standards and Technology, Boulder Internal Note, CO, USA, October 1999.
[MAP06]	F. Moglie and A. P. Pastore, "FDTD analysis of plane wave superposition to simulate susceptibility tests in reverberation chambers," in IEEE Transactions on Electromagnetic Compatibility, vol. 48, no. 1, pp. 195--202, Feb. 2006, doi: 10.1109/TEMC.2006.870793.
[MBC02]	L. Musso, V. Berat, F. Canavero, and B. Demoulin, “A plane wave Monte Carlo simulation method for reverberation chambers”, International Symposium Electromagnetic Compatibility, EMC Europe, vol. 1, pp. 45—50, Sorrento, Italy, September 2002.
[MPS23]	P. Mursia, S. Phang, V. Sciancalepore, G. Gradoni and M. Di Renzo. “SARIS: Scattering Aware Reconfigurable Intelligent Surfacemodel and Optimization for Complex Propagation Channels”, 2023, [Online]: https://arxiv.org/abs/2302.01739
[MSG21]	P. Mursia, V. Sciancalepore, A. Garcia-Saavedra, L. Cottatellucci, X. C. Pérez and D. Gesbert, "RISMA: Reconfigurable Intelligent Surfaces Enabling Beamforming for IoT Massive Access," in IEEE Journal on Selected Areas in Communications, vol. 39, no. 4, pp. 1072-1085, April 2021, doi: 10.1109/JSAC.2020.3018829.

[NFE18]	J. Ø. Nielsen, W. Fan, P. C. F. Eggers, and G. F. Pedersen, “A channel sounder for massive MIMO and MmWave channels,” IEEE Commun. Mag., vol. 56, no. 12, pp. 67–73, December 2018.
[NJS+21]	M. Najafi, V. Jamali, R. Schober and H. V. Poor, "Physics-Based Modeling and Scalable Optimization of Large Intelligent Reflecting Surfaces," in IEEE Transactions on Communications, vol. 69, no. 4, pp. 2673-2691, April 2021, doi: 10.1109/TCOMM.2020.3047098.
[NP21]	J. Ø. Nielsen and G. F. Pedersen, “Amplitude distributions of measured 21.5 GHz indoor channels for a handheld array,” in 2021 15th European Conf. Antennas and Propagation (EuCAP), 2021, pp. 1–5.
[QD21]	X. Qian and M. D. Renzo, "Mutual Coupling and Unit Cell Aware Optimization for Reconfigurable Intelligent Surfaces," in *IEEE Wireless Communications Letters*, vol. 10, no. 6, pp. 1183-1187, June 2021, doi: 10.1109/LWC.2021.3061449.
R18	T. Reveyrand, “Multiport conversions between S, Z, Y, h, ABCD, and T parameters”, 2018 International Workshop on Integrated Nonlinear Microwave and Millimetre-wave Circuits (INMMIC)
[RMG22]	M. Rossanese, P. Mursia, A. Garcia-Saavedra, V. Sciancalepore, A. Asadi, and X. Costa-Perez, “Designing, building, and characterizing RF switch-based reconfigurable intelligent surfaces”. In Proceedings of the 16th ACM Workshop on Wireless Network Testbeds, Experimental evaluation & CHaracterization (WiNTECH '22), 2022.
[TAF95]	A. Taflove, "Computational Electrodynamics: The Finite-Difference Time-Domain Method", Norwood, MA: Artech House, 1995.
[TR18]	T. Reveyrand, "Multiport conversions between S, Z, Y, h, ABCD, and T parameters," 2018 International Workshop on Integrated Nonlinear Microwave and Millimetre-wave Circuits (INMMIC), Brive La Gaillarde, France, 2018
[YH07]	M. A. Yurkin and A. G. Hoekstra, “The discrete dipole approximation: An overview and recent developments,” J. Quantitative Spectroscopyan d Radiative Transfer, vol. 106, no. 1, pp. 558–589, 2007.
[VAK+23]	E. M. Vitucci, M. Albani, S. Kodra, M. Barbiroli, V. Degli-Esposti, “An Efficient Ray-Based Modeling Approach for Scattering from Reconfigurable Intelligent Surfaces,” 2023, 10.36227/techrxiv.23041643.v1
[ZZW+22]	Z. Zhang et al., "Macromodeling of Reconfigurable Intelligent Surface Based on Microwave Network Theory," in IEEE Transactions on Antennas and Propagation, vol. 70, no. 10, pp. 8707-8717, Oct. 2022, doi: 10.1109/TAP.2022.3187645.